The Physics of Muon Cooling for a Neutrino Factory

Simon Holmes
Balliol College, Oxford

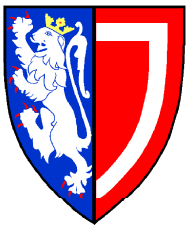

Thesis submitted in fulfillment of the requirements for the degree of Doctor of Philosophy at the University of Oxford

Hilary Term, 2006

The Physics of Muon Cooling for a Neutrino Factory

Simon Holmes
Balliol College, Oxford

Thesis submitted in fulfillment of the requirements for the degree of Doctor of Philosophy at the University of Oxford

Hilary Term, 2006

Abstract

Muon cooling is a way to reduce the spread of a beam of muons so that they can be put into a storage ring and used to produce neutrinos. Cooling depends on the relative amount of energy loss and scattering in a suitable absorber; materials with a low atomic number are preffered. However there is a lack of data for muons in such absorbers, and traditional scattering predictions for electrons have been shown to lose accuracy as atomic number decreases. The MICE experiment has been proposed to demonstrate muon cooling and tune simulations, while new data on muon scattering in a variety of materials has just been taken by the MUSCAT experiment.

A first principles derivation of the passage of muons in liquid hydrogen avoids traditional simplifications. The result is a double differential cross section in energy loss and scattering (ELMS), which is folded into a probability distribution for millimetre path lengths. This probability distribution shows a first order correlation between energy loss and scattering that is ignored in other simulations. The ELMS database is incorporated into an existing simulation package to show that the predicted performance of six dimensional muon cooling is increased. The scattering predictions made by the ELMS approach are distinct from those of existing models, and supported by empirical data from MUSCAT.

To my parents, who have given me all things in all ways.

Acknowledgements

In a Ripley's believe it or not exhibit there's a metallic vat with a round ball of pink sausage strings in it, coiled up in the way films show you what brains are like. A woman looks it up and down for a moment and reads the accompanying plaque. She turns to her boyfriend excited and says, "wow look, they've got Einstein's brain!" The poor guy, his face drops, and suddenly eyeing his girlfriend in as much disbelief as any of the other exhibits, he replies, "what the hell would Einstein's brain be doing in some dodgy fairground?" The point of this is that whilst the numerous artefacts on show – the three eyed fox, a piece of the Berlin wall, the world's smallest woman (in a jar) - were all unconvincing, plastic, and with apologies to Ripley's aficionados, ridiculous, they all offered something tangible to examine and judge.

Physics always used to be the same. When Du Chatelet dropped lead balls into clay from a height to show that kinetic energy is proportional to velocity squared, the conclusion was immediate with just one look: you could see that the ball that fell from twice the height went four times, and not twice as deep into the clay. Similarly much of classic science has beautiful experiments with accessible, visible results. But this accessibility must be true for the very reason that the subject is called classical, which has come to mean referring to our everyday experience. In physics these times are long gone. The quantum, uncertain, description of the world is de rigueur. And while this does and must reduce to classical physics at some level, any new discoveries build so high up on a column of intellectual giants that the normal world can't be seen from the top.

So here am I having written a thesis about techniques for creating sub-atomic ghosts, with results that are expressed as lines on graphs and confidence intervals. But that is the nature of physics these days. And it is a credit to all of the tutors and lecturers I have encountered at Oxford that they have made the subject as fascinating as it was back in the days when crowds of people would queue to literally feel a spark of electricty in their body, back when scientists were the celebrity of the day. Well, you can't have it all.

This thesis could not have been completed without the hard work, help, and support of

my supervisor, Wade Allison, who has driven the whole project forward from the beginning and given me much to aspire to. There are also other academic colleagues who have helped with the completion of this and who I would like to thank: John Cobb for suggestions and insight that shaped the fourth chapter, for help with understanding emittance, and advice on presentation that went far beyond the call of duty; Bill Murray and Rob Edgecock for assistance during the MUSCAT analysis; Ulisse Bravar for help with the MICE analysis; Bob Palmer and Rick Fernow for ICOOL and the RFOFO; Ed McKigney for GEANT; and Stephen Brooks for the alternate materials analysis. At Balliol college, my advisor Jonathan Hodby has always made time for me when I have needed advice about career progress and funding applications, and as such I am indebted to him. I would also like to thank all of the college members and staff who have made my eight years there so memorable.

To paraphrase Bret Easton Ellis, writing a thesis is not method acting, and I too find it easy to step out of at cocktail hour. So thanks too to my friends during the time of research; especially, Anil, Babs, Celine, Freddy, Keens, John, Louise, Luke, SJ, and Tom. You have helped keep me sane. And then there is the wonderful Jeandre. Also anyone else I may have forgotten, you deserve thanks for reading this far.

This work was funded to a large extent by a PPARC research grant, for which I am grateful.

Contents

List of Figures

List of Tables

Introduction

This thesis details the benefits of muon cooling towards future scientific experiments and shows that the technique may be more effective than traditional simulations predict. It is motivated by recent developements in particle physics, where often it is many years after a theory is accepted to be right that a more detailed experiment finds it wanting. For instance the once fundamental proton is seen to be made of quarks when probed at high enough energy. Likewise, recent observations and theoretical work give strong hints that the 1980's standard model of particle physics is incomplete. Neutrino oscillations and leptonic CP violation are one possible area, another is the search for the Higgs boson and the postulation of super-symmetric particles.

Muons are key to exploring both of these phenomena. These short lived members of the lepton family decay into neutrinos and electrons. If muons could be contained in a storage ring before they decayed, they could produce either a beam of neutrinos that could be studied (a neutrino factory) or be collided with their anti-particle to make a muon collider. However the storage of muons before decay is non-trivial. To get a high flux requires a way to focus a beam into a small enough volume to fit inside the storage ring, this is called beam cooling, and conventional cooling methods are not suitable for muons because of their short lifetime.

Muon cooling could be achieved by passing muons through an absorber so that they lose energy along the direction of travel and scatter (slightly), before re-accelerating the beam in the required direction. If this is repeated many times the transverse size of the beam will decrease. Other techniques can be used to shrink the beam size in longitudinal space. The physics of energy loss and scattering means that absorbers with low atomic number are required to minimise the scattering with respect to the energy loss, with liquid hydrogen the favoured candidate. However there is a lack of experimental evidence of the behavior of muons in such absorbers, and what does exist suggests that traditional multiple scattering

models are not correct for materials with low atomic number. The MICE experiment has been proposed to build a working section of a full cooling channel to confirm that the engineering challenges can be overcome, and help tune simulations. This is important because the iterative nature of muon cooling mean that any slight error will soon multiply up over many stages.

The presence of accurate data on the atomic structure of hydrogen and modern computing power means that it is possible to do much better. This thesis presents a first principles derivation of the double differential cross section (in energy loss and scattering) of muons in liquid hydrogen (ELMS). This cross section contains a class of collisions that are correlated in energy loss and scattering, which is not considered by traditional approaches because they treat energy loss and scattering separately. The ELMS cross section is folded into a three-dimensional probability distribution enabling Monte Carlo simulation of a beam of muons passing through liquid hydrogen.

A database of ELMS probability distributions is incorporated into ICOOL, a traditional simulation program, and the performance of the new cross section and the traditional calculations is compared in a variety of different cooling scenarios. It is shown that the new approach leads to a predicted improvement in cooling because the traditional simulations overestimate the scattering in materials of low atomic number. This discrepancy is supported by new empirical data from MUSCAT measuring the scattering of muons in a variety of absorbers. The ELMS prediction compares well with this data.

Chapter 1

The challenge of studying physics beyond the standard model

The standard model of particle physics is incomplete. Neutrinos were once thought of as massless but are now believed to have a small mass and oscillate, explaining why a deficit in both solar neutrino flux and atmospheric neutrino ratios have been observed in recent time. Evidence exists mainly from natural sources, with nuclear reactors the primary man-made source to date. However because muons decay to neutrinos, they are a useful tool to enhance research in neutrino physics. A storage ring of muons, which is called a neutrino factory, could further pin down the oscillation scheme of neutrinos and mass hierarchy, and look for evidence of charge parity violation in the leptonic sector. The neutrino factory would also be the first step towards making a muon collider, which is not limited in energy by synchrotron radiation like conventional electron machines and could probe the couplings of the Higgs boson and study any super-symmetric particles.

1.1 The standard model

The standard model states that the universe is made up of two groups of fundamental fermions, the leptons and the quarks, and a group of bosons, which act to carry force between the fermions, see table 1.1. All matter can be described in this formalism: an atom of hydrogen thus consists of a nucleus made from up and down quarks bound by the strong force of the gluons, and a solitary orbiting electron bound to the nucleus by the electromagnetic force, which is mediated by photons.

The standard model was the triumph of 1980's particle physics. It correctly explained the observable phenomena of the time, including the quark content and interaction strengths of known baryons and mesons, and went on to successfully predict the outcomes of many future experiments including the discovery of the the W and Z bosons and the top quark. The most important part of the standard model is the unification of the electromagnetic

Leptons	Charge	Mass (MeV/c^2)
e	-1	0.511
ν_e	0	< 3 eV
μ	-1	105.7
ν_μ	0	< 0.19
τ	-1	1777
ν_τ	0	< 18.2

Quarks	Charge	Mass
d	$-\frac{1}{3}$	5–8.5 MeV/c^2
u	$\frac{2}{3}$	1.5–4.5 MeV/c^2
s	$-\frac{1}{3}$	80–155 MeV/c^2
c	$\frac{2}{3}$	1.0–1.4 GeV/c^2
b	$-\frac{1}{3}$	4.0–4.5 GeV/c^2
t	$\frac{2}{3}$	174.3 ± 5.1 GeV/c^2

Bosons	Charge	Mass (GeV/c^2)
γ	0	$< 2 \times 10^{-25}$
W^+	1	80.423 ± 0.039
W^-	-1	80.423 ± 0.039
Z^0	0	91.1876 ± 0.0021
gluons	0	0
Higgs	0	> 114.3

Table 1.1: The particles and mediators of the standard model, including the Higgs boson; the lower mass bound for the Higgs is given for LEP2 data [1].

and weak interactions, which is discussed later. This unification offers hope that all known interactions in physics can be unified, even though the standard model still contains no reference to the gravitational force.

The standard model postulates the Higgs boson as the mechanism that gives mass to fundamental particles. This is the only unconfirmed part of the model, and hence the discovery of the Higgs is a vital test. The Large Hadron Collider (LHC) at CERN will soon perform a detailed search for the Higgs at energies above those of previous accelerators, and covering the expected range of the Higgs mass from calculations based on theory and previous experiment.

The Higgs has a relatively small mass with respect to the Planck mass, which is an example of the hierarchy problem in particle physics. This states that since all solvable theories are perturbative there must be a hierarchy of corrections in power series. This hierarchy is not seen in the masses of observable particles, where mass corrections differ by orders of magnitude. So whilst any theory is not necessarily represented by perturbation theory, the hierarchy problem does still suggest the presence of physics outside of the standard model such as super-symmetry. Another example is the mass of neutrinos. These weakly interacting particles once thought of as massless, oscillate between flavours implying that they have a small, definite mass. But why the mass is so much smaller than every other particle is

unknown. Indeed the Higgs may be the favoured mechanism to give mass to the standard model particles, but there is no explanation why each particle has the mass it does. In total the standard model contains at least nineteen free parameters.

There is much to be discovered to complete the standard model. Two experimental devices based on storage rings of muons that would further this aim are the neutrino factory and the muon collider. If constructed, the neutrino factory would enable a detailed study of neutrino physics and leptonic CP violation, whilst a muon collider's low background and high centre of mass energy would allow the Higgs and any super-symmetric particles to be studied.

1.2 The neutrino factory

1.2.1 Discovery of the neutrino

The history of weak physics is typical of that of particle physics in general: unexpected results lead to a flurry of theoretical activity to explain them. That said, it was more than thirty years between the observation of beta decay in 1898 and the postulation of a new neutral particle to explain it [2], and a similar length of time until this particle was detected in 1956 [3].

Beta particles are radiation in the form of electrons produced when a neutron turns into a proton in the nucleus of an atom (a down quark becoming an up quark). In 1914, Chadwick's observation of a continuous energy spectrum of beta particles [4] led to two conclusions: either the spectrum was due to an unexplained primary process (a two body decay should produce electrons of fixed energy), or it was a discrete spectrum being broadened by secondary processes.

Ellis and Wooster [5] devised an experiment to test these two hypotheses by measuring the absolute heat produced in a beta decay. This heat would thence either correspond to the mean value of the observed beta spectrum (if the first case were true), or would be the maximum of the observed beta spectrum. Their results gave a good match to the observed mean, but excluded the possibility that energy escaped as gamma radiation. Further work by Meitner and Orthman using ionisation tubes [6] would later disprove this possibility.

Pauli postulated the existence of a fourth body in the beta decay process. The problem of the observed spectrum of beta decay was solved if an electron and this new particle, the neutrino, were emitted together with a constant total energy. Fermi later developed the prediction into a theoretical description of beta decay.

The beta decay probability $n \rightarrow p + e^- + \bar{\nu_e}$ is given by Fermi's Golden Rule [7],

$$\Gamma = 2\pi \mid M_{fi} \mid^2 \rho(E_f),$$

where the matrix element M is given by the four point interaction with a strength equal to the Fermi constant, G_f, so that $\mid M_{fi} \mid^2 \approx G_F^2$. The cross section for neutrino scattering $\bar{\nu_e} + p \rightarrow n + e^+$ is related to the beta decay by a crossing symmetry. There are a total of four possible spin states for the leptonic e and ν: a singlet state S=0, and three triplet states S=1. It is necessary to average over initial states and sum over final states. The differential cross section is given by,

$$d\sigma = 8\pi G_F^2 \frac{E_e^2}{(2\pi)^3} d\omega,$$

where E_e is the electron energy. Hence the total cross section is given by,

$$\sigma = \int \frac{d\sigma}{d\omega} d\omega = \frac{4 G_F^2 E_e^2}{\pi}.$$

Following this, Reines and Cowan [8] proposed a technique to discover the neutrino. Due to the size of the Fermi cross section (around 10^{-46} m^2) they required an intense neutrino source (a nuclear reactor) and a heavy target to capture even a few of the particles using the inverse beta decay process ($\bar{\nu_e} + p \rightarrow n + e^+$). Their experiment consisted of four hundred litres of water mixed with cadmium chloride. The signature of a neutrino event was the positron annihilating into two simultaneous photons, and then the neutron slowing down and being captured by the cadmium, releasing another photon. This second capture process took up to seventeen microseconds. Reines and Cowan used the time delay and energy spectrum of the measured photons to reduce background from other interpretations and confirmed the existence of the neutrino, see figure 1.1.

The energy spectrum of the electron produced in the beta decay process of tritium is the most sensitive way to calculate an estimate of the neutrino mass. The decay is super-allowed (the only change in the nuclear state is the charge), hence the electron spectrum is determined by phase space, which is sensitive to the mass of the neutrino. An upper limit

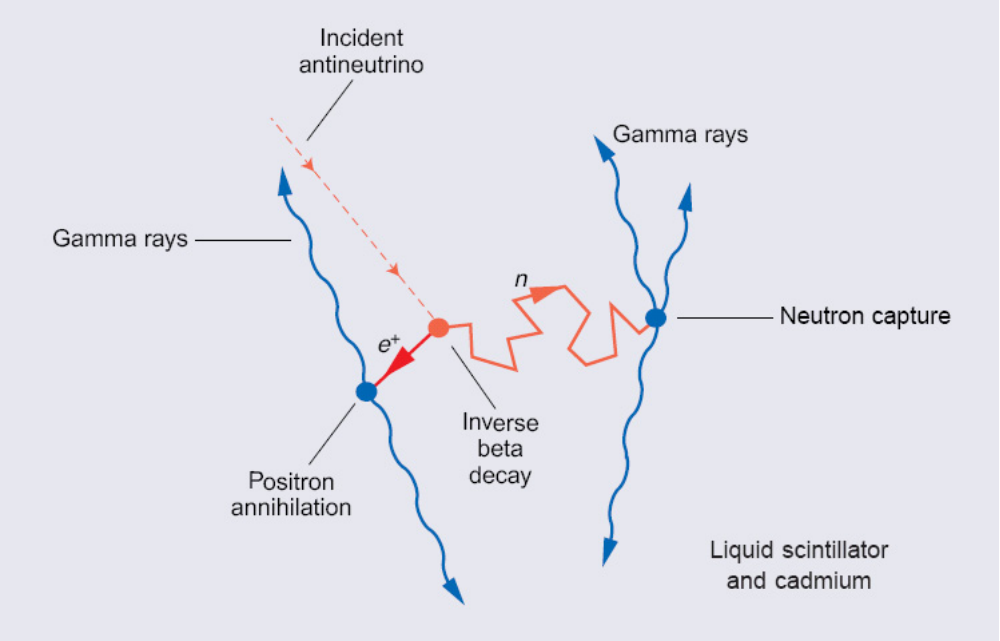

Figure 1.1: The underlying physics process in the Reines and Cowan experiment [8].

on the electron neutrino mass is 3 eV at present. It was this small and ambiguous nature of early mass limits and appealing to simplicity that suggested that neutrinos were massless.

1.2.2 Neutrino oscillations

At the same time as Reines and Cowan were discovering anti-neutrinos, Davis was studying reactor neutrinos using a chlorine target, testing whether the anti-neutrinos produced by the reactor would convert chlorine to argon (implying non-conservation of lepton number since an anti-neutrino would be converted into an electron). He saw no signal. In 1969 Davis started another experiment, this time to study neutrinos produced in the sun (an allowed reaction $\nu_e + {}^{37}\mathrm{Cl} \Rightarrow e^- + {}^{37}\mathrm{Ar}$) in a six hundred tonne target deep underground in the Homestake mine. In effect, the 10^{-46} m^2 neutrino interaction probability meant that, if captured, neutrinos would give insight into the conditions when they were produced by nuclear fusion deep inside the sun. However Davis observed a large deficit in the expected number of electron neutrinos captured. Quoting results in terms of Solar Neutrino Units (1 SNU corresponding to 1 capture per second from 10^{36} nuclei) the results from Davis experiment averaged over more than twenty years of data is 2.56 $\pm$ 0.16 (statistical error) $\pm$ 0.16 (systematic). The standard solar model (SSM) predictions as calculated by Bahcall et al is $7.7^{+1.2}_{-1.0} \pm 3.0$ SNU [9].

An explanation for Davis's observation is that neutrinos can mix in space and change flavour. Davis's experiment was only sensitive to one flavour of neutrinos (ν_e type), thus he saw less of these than he expected. The confirmation of neutrino oscillation only came more recently from the Sudbury Neutrino Observatory (SNO), discussed later, and were extended by data from neutrinos produced in the atmosphere and neutrinos from a reactor source.

Neutrino oscillations imply that neutrinos have mass since an oscillation can be thought of as a 2-body process in a Lorentz invariant frame, which cannot occur for a massless particle [10]. Hence the flavour states ν_e, ν_μ, and ν_τ are superpositions of states of neutrinos with a definite mass (similar to how K_0 and $\bar{K_0}$ are superpositions of K_l and K_s). All existing data suggest that the masses of neutrinos are much smaller than even the lightest leptons or quarks. The following text assumes that neutrinos interact with other particles as described by the standard model of electroweak interactions and that only three flavours of neutrinos exist (as determined by measurements of the Z boson resonance [11]), with a neutrino corresponding to each of the fundamental leptons.

The analogous quark mixing is well understood; quark fields enter into the electroweak current in a mixed form as described by Cabbibo-Kobayashi-Maskawa (CKM) mixing. However neutrinos differ from quarks in that they have no charge - it is not known whether neutrinos are Dirac particles (like quarks) or neutral Majorana particles. The difference is that in the Majorana scheme a neutrino is its own anti-particle, whereas in the Dirac scheme the two states are distinguishable. The implication of neutrinos being Majorana type particles would be that there is no conserved lepton charge. The theoretical see-saw mechanism that can account for the small mass of neutrinos also predicts that they are Majorana type [12].

The neutrino mixing matrix is characterised by certain parameters; in the 3x3 case, the matrix has three angles and either one or three physical phases (depending if neutrinos are Dirac or Majorana). Only the mass differences of neutrinos enter into oscillation probability - investigating neutrino mixing gives no insight into the physical nature of neutrinos with definite mass [13].

It is straight forward to derive neutrino oscillation probability equations [14]. The probability of oscillation is given by the modulus squared of the overlap of the observed flavour state with the time evolved initial state, which in vacuum just depends on the free particle

Hamiltonian. Setting $\hbar = c = 1$:

$$\mid \nu_\alpha > (t) = e^{-iH_0 t} \mid \nu_\alpha >,$$

where the flavour eigenstates, ν_α, are connected to the mass eigenstates, ν_i, through the leptonic mixing matrix, U, as discussed above:

$$\mid \nu_\alpha >= \Sigma_i U_{\alpha i} \mid \nu_i > .$$

Taking $t \approx L$, the modulus squared of the overlap of the flavour states then involves the mass difference between the states,

$$P(\nu_\alpha \longrightarrow \nu_\beta) = \Sigma_{i,j} U_{\alpha i} U^*_{\beta i} U^*_{\alpha j} U_{\beta j} e^{\frac{i\delta m^2_{ij} L}{2E}}.$$

Parameterizing U in terms of mixing angles and complex phases, assuming a mass scale $m_1 < m_2 \ll m_3$ such that $\Delta m^2_{23} \approx \Delta m^2_{13}$, where $\Delta m^2_{ij} = m^2_i - m^2_j$, and neglecting oscillation driven by a small mass scale and hence CP violating terms [15], gives for example:

$$P(\nu_e \longrightarrow \nu_\mu) = \sin^2(2\theta_{13}) \sin^2(\theta_{23}) \sin^2(\frac{\delta m^2_{23} L}{4E}). \tag{1.1}$$

The important points to note are:

1. Transition probability depends on the ratio L/E, where L is the length and E is the energy of the neutrino.

2. The condition, $\delta m^2_{23} L/4E \geq 1$, which must be satisfied, describes where experiments can observe neutrino oscillations.

3. Because of CPT invariance, the oscillation probability is the same for neutrinos and anti-neutrinos $P(\nu_\alpha \longrightarrow \nu_\beta) = P(\bar{\nu_\beta} \longrightarrow \bar{\nu_\alpha})$.

4. If CP invariance holds in the lepton sector $P(\nu_\alpha \longrightarrow \nu_\beta) = P(\bar{\nu_\alpha} \longrightarrow \bar{\nu_\beta})$.

1.2.3 Current oscillation results

There are a number of neutrino sources that have been studied: neutrinos from cosmic ray collisions in the earth's atmosphere, neutrinos created by the sun, and neutrinos made in nuclear fission reactors. The varying baselines and energies involved allow the study of a large range of parameters, but there are still gaps in knowledge that a neutrino factory would fill.

1. Atmospheric neutrinos: When high energy protons interact in the earth's atmosphere they produce a number of particles through strong interactions. Neutrinos come from decays of charged pions into muons and muon neutrinos, with additional muon and electron neutrinos made as the muons decay into electrons ($\pi \longrightarrow \mu + \nu_\mu$, $\mu \longrightarrow e + \nu_\mu + \nu_e$). Consideration of these process implies that, at low energy (< 1GeV) where all muons decay in the atmosphere, there should be two muon neutrinos for every electron neutrino. At higher energy the ratio will be larger than two, but is predictable. Experiments do not observe the two to one ratio because the muon neutrinos are missing. The favoured hypothesis for the observed data is that muon neutrinos oscillate into tau neutrinos.

Atmospheric neutrinos are particularly useful in a comparison of up and down events. The lepton produced in detected reactions travels roughly collinear to the direction of the neutrino, hence the neutrinos traveling up through the earth and those traveling down from the atmosphere can be separated. The relative number of muon neutrinos of up and down types, which have different oscillation baselines, gives strong evidence for the oscillation of muon neutrinos, see figure 1.2.

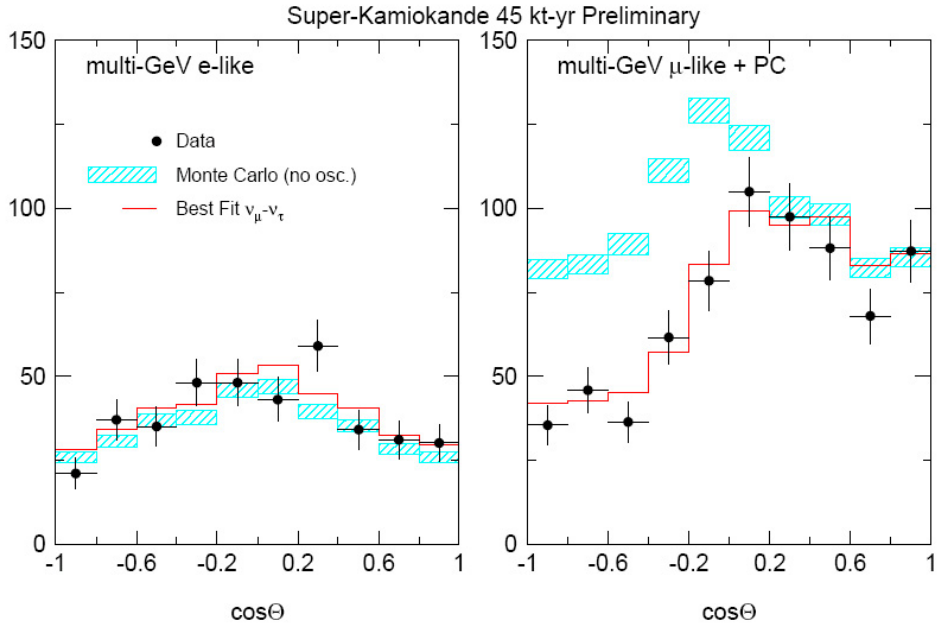

Figure 1.2: Fluxes of muon and electron type neutrinos as a function of angle as measured with Super K [16]. The electron type flux is as expected, but the muon type flux shows a deficit at large angles (distances).

2. Solar neutrinos: The sun's energy comes from reactions in the pp chain and CNO

cycle [17], which turn protons and electrons into helium and electron neutrinos: $4p+2e^- \longrightarrow He + 2\nu_e$. The total flux of neutrinos is fixed. Various reactions in these schemes produce neutrinos of differing energy. The highest flux (produced in the combination of two protons into deuterium) are of a low energy (<0.42 MeV), and the dominant source of neutrinos detected by experiments like Homestake and SNO [18] are those from the decay of beryllium, which have a maximum energy of 15 MeV, but a flux four orders of magnitude less than the deuterium neutrinos. All experiments attempting to measure the flux of solar electron neutrinos at the earth found a deficit compared to that predicted by the standard solar model. SNO, a neutrino detector, was the first experiment to be sensitive to other flavours of neutrinos. By using heavy water (D_2O) it had three channels for detecting neutrinos: a charged current $\nu_e + D \rightarrow e^- + p + p$, sensitive to electron type neutrinos; a neutral current $\nu_x + D \rightarrow \nu_x + n + p$, sensitive to all flavours of neutrino; and elastic scattering $\nu_x + e^- \rightarrow \nu_x + e^-$, sensitive to all flavours, but enhanced for ν_e. SNO could check if the total neutrino flux was compatible with that predicted by the SSM and also give evidence that other neutrinos make up some of the solar neutrino flux at the earth. SNO measured neutrino fluxes in the following detection channels (in units of 10^6 cm^{-2} s^{-1}):

Charge current channel = 1.76 ± 0.11

Neutral current channel = 5.09 ± 0.62

Elastic scattering channel = 2.39 ± 0.26

Comparing with the standard solar model flux prediction of 5.05 ± 1.0 showed agreement with the neutral current flux. But comparing the neutral current to the charge current implied that the hypothesis of no neutrino flavour change was disallowed by more than five standard deviations, see figure 1.3.

3. Reactor neutrinos: The solar neutrino results are reinforced by many reactor based experiments that study $\bar{\nu_e}$. Perhaps the most important is that of KamLAND [19]. Here the anti-electron neutrinos from several reactors across Japan are detected by the observation of inverse beta decay in a large liquid scintillator detector. Results were in good agreement with existing solar neutrino results and ruled out various mixing schemes. As figure 1.4 shows, previous reactor results did not have a long enough baseline to be sensitive to oscillations, but KamLAND was ideally placed to see a reduction compatible with the best-fit large mixing

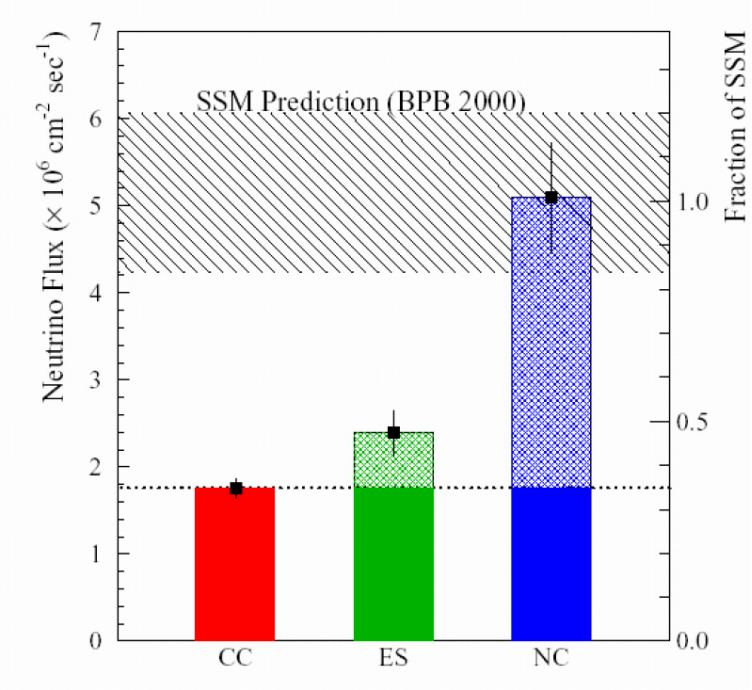

Figure 1.3: Results from SNO disallowing the no neutrino flavour change hypothesis [18].

angle prediction.

Assuming that neutrinos are Dirac particles, the neutrino mixing matrix can be written as,

$$U = \begin{pmatrix} c_{12} & s_{12} & 0 \\ -s_{12} & c_{12} & 0 \\ 0 & 0 & 1 \end{pmatrix} \begin{pmatrix} c_{13} & 0 & e^{-i\delta_{s13}} \\ 0 & 1 & 0 \\ -e^{-i\delta_{s13}} & 0 & c_{13} \end{pmatrix} \begin{pmatrix} 1 & 0 & 0 \\ 0 & c_{23} & s_{23} \\ 0 & -s_{23} & c_{23} \end{pmatrix},$$

where c_{12} corresponds to the cosine of mixing angle θ_{12}, and so on. Atmospheric neutrino measurements imply the mass difference $\mid \Delta m^2_{23} \mid \approx 2 \times 10^{-3}$ eV^2 while solar and reactor neutrino measurements imply $\mid \Delta m^2_{12} \mid \approx 5 \times 10^{-5}$ eV^2. Limits on the mixing angles from atmospheric neutrinos show θ_{23} is almost forty five degrees (maximal mixing). Solar measurements require θ_{12} between a few degrees and forty degrees (small or large mixing angle scheme), and the CHOOZ reactor experiment [20] indicated θ_{13} is smaller than ten degrees. These limits are shown in figure 1.5.

An important future result is that of MINOS [21], which is an accelerator based experiment to measure the ν_μ to ν_τ oscillation, consisting of a muon neutrino beam with near and far detectors built to search for tau particles produced from tau neutrinos. It hopes to have a sensitivity to Δm^2_{23} and $\sin\theta_{23}$ of better than 10%.

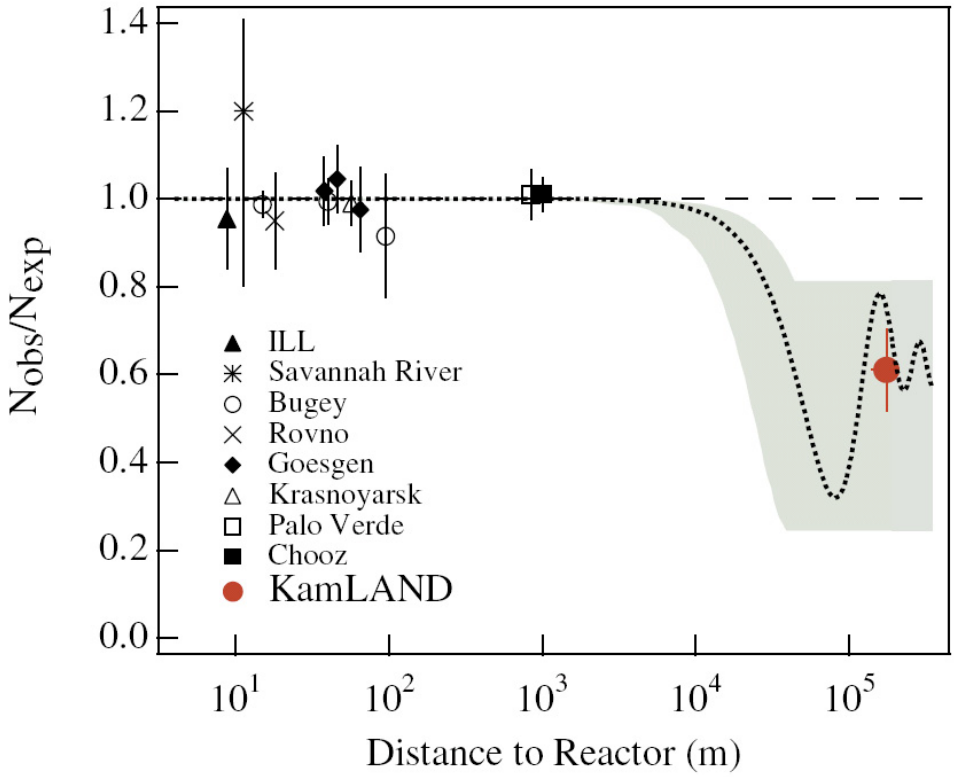

Figure 1.4: The measured $\bar{\nu_e}$ flux from various reactor experiments. The solid circle is the KamLAND result positioned at a flux corrected average distance from the Japanese reactors. The shaded region indicates the range of flux at 95 percent confidence from a global analysis of solar neutrino data. The dotted curve represents the best fit LMA prediction [19].

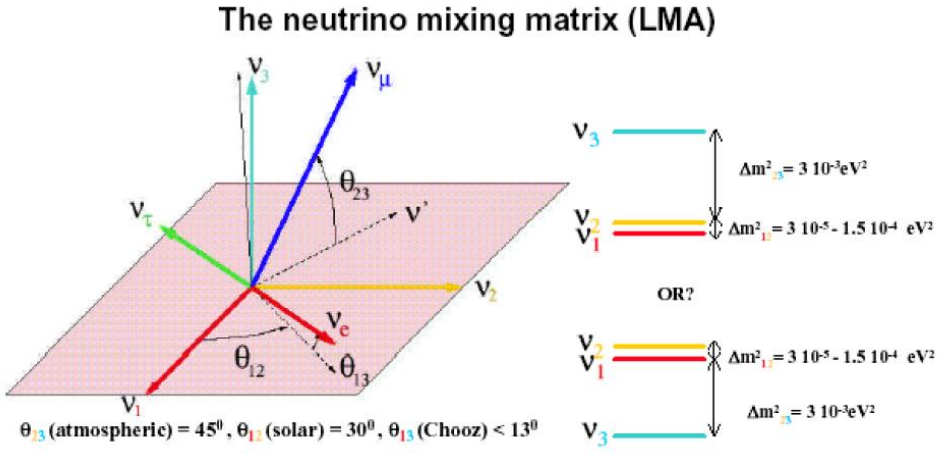

Figure 1.5: Likely values for the various mixing angles and mass differences in the large mixing angle scheme [22].

1.2.4 The discovery of the muon

The observation that the electron had a heavier lepton partner was perhaps even more surprising than the nature of the beta decay spectrum or the observation of missing solar neutrinos. The fundamental particles of the time were thought to be the proton, the electron, and the neutron. Understanding the nature of muons and how they are created is the first step to showing why they must be cooled before being of use to future experiments.

In 1935 Yukawa had predicted that an intermediate mass meson might be responsible for the strong force in the same way as the photon carried the electromagnetic force. His value of around 100 MeV/c^2 for the mass, which he obtained by combining the apparent range of the strong force and the uncertainty principle, was very close to the mass observed of a new particle by Street and Stevenson in their cloud chamber experiment [23]; it was natural to identify this new particle with the Yukawa meson. However experiments soon observed a decay chain of two particles – the decay product was shown to be a lepton heavier than an electron, named the muon, while the original particle was a meson, named the pion, which was not the Yukawa particle, but an important discovery in the building of the standard model.

The reason why charged pions decay into muons, and not the lighter and hence energetically favourable electrons, is because of spin and angular momentum. A pion has spin zero, so for it to decay into two spin half particles (lepton plus anti-neutrino), they must be produced with opposite spin or angular momentum; however, the weak force only interacts with left handed particles and right handed anti-particles. A massless neutrino is thus totally right handed (spin aligned with momentum) and the lepton produced in the decay must also be right handed to conserve angular momentum. Since muons are heavy they have a higher amount of right handed spin so the decay to muons is favoured.

$$\pi^+ \longrightarrow \mu^+ + \nu_\mu$$

$$\pi^- \longrightarrow \mu^- + \bar{\nu_\mu}$$

Pion decays offer a source of muons that could be used in a neutrino factory or muon collider. But by the nature of the decay, the phase space occupied by the muons is large and must be reduced for them to be useful, the techniques to do so will be covered in chapter 2. The motivation for building a neutrino factory is described forthwith.

1.2.5 Towards a neutrino factory

A neutrino factory is a storage ring of muons that decay into neutrinos. Muons decay into three particles with a lifetime of just over two microseconds at rest, as shown below. Muon decay thus provides an intense flux of neutrinos, either ν_μ and $\bar{\nu_e}$ in equal ratios, or $\bar{\nu_\mu}$ and ν_e. It is the flux ratios and types of neutrinos available to study that make a neutrino factory desirable.

$$\mu^- \longrightarrow \bar{\nu_e} + \nu_\mu + e^-$$

$$\mu^+ \longrightarrow \nu_e + \bar{\nu_\mu} + e^+$$

Several designs for a neutrino factory exist. One is shown in figure 1.6. The initial linac acts as proton source to provide a powerful beam of protons with an energy of a few GeV. This beam is fired into a nucleon rich target, such as solid carbon, or liquid mercury. The proton impact creates numerous particles. Pions and then muons are selected by a series of magnetic horns, or a magnetic focusing channel. The phase space volume of the muon beam is reduced by the technique of ionisation cooling, which is the main thread of this thesis and will be covered in much detail in what is to come. Last the muons are accelerated through a series of linear accelerators and injected into a bow-shaped storage ring. Once the muons are in this ring they will decay along the long straight baselines producing beams of neutrinos that point into an angular divergence that is typically less than 1 mrad.

The advantage of neutrino beams produced from muon storage is that it is possible to calculate the energy spectrum of the beam given the energy, divergence, and polarisation of the muons; the content of the beam is known, there is little contamination since the lepton numbers of the neutrinos in the beam are opposite; changing the sign of the stored muon beam produces a charge conjugate neutrino beam; and the energy of the neutrinos produced allows the oscillation of electron type into tau type neutrinos, which is unique to a neutrino factory.

1.2.6 Precise measurements of neutrino oscillations

A likely detector system for the neutrino factory would comprise a near and far detector to measure oscillation at different distances. The near detector will accept neutrinos produced over a larger angle and hence a larger energy spread due to its proximity to the storage ring.

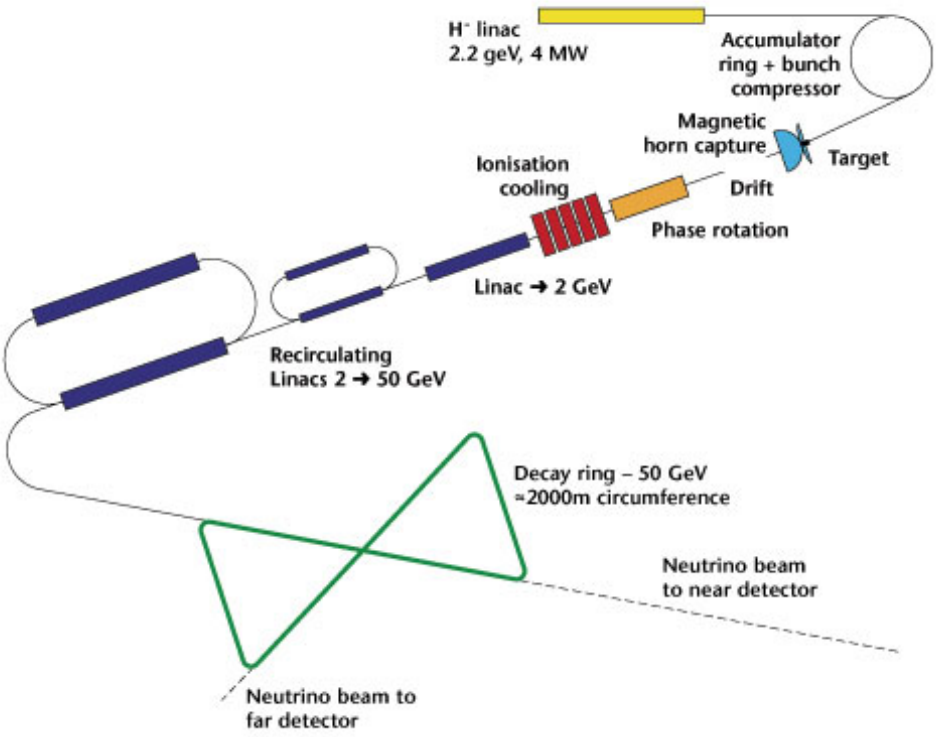

Figure 1.6: One of the possible designs for a neutrino factory [22].

The far detector will have a much smaller angular acceptance. The aim is to measure the oscillation probability as a function of the baseline and energy for all possible initial and final flavours. Neutrinos will interact in the far detector through charged current (CC) and neutral current (NC) weak interaction events. In CC events the lepton's charge and flavour tags the incoming neutrino [15].

The data sets produced are diverse [24]. The parent neutrino is identified by looking at the sign and charge of the detected lepton. For a storage ring of negative muons decaying to ν_μ and $\bar{\nu_e}$, the following cases can occur:

1. $\nu_\mu \longrightarrow \nu_\mu$ survival.
2. $\nu_\mu \longrightarrow \nu_e$ appearance.
3. $\nu_\mu \longrightarrow \nu_\tau$ appearance.
4. $\bar{\nu_e} \longrightarrow \bar{\nu_e}$ survival.
5. $\bar{\nu_e} \longrightarrow \bar{\nu_\mu}$ appearance.

6. $\bar{\nu_e} \longrightarrow \bar{\nu_\tau}$ appearance.

Reversing the sign of the stored muon produces six conjugate reactions.

The most important case is the detection of a wrong signed muon (channel 5, and equation 1.1). Since an electron is indistinguishable from a positron in detectors, this reaction gives information about the previously hard to study mixing angle θ_{13} (currently an upper limit) assuming a knowledge of $\mid \Delta m^2_{23} \mid$ and $\sin^2 \theta_{23}$ from future results from experiments like MINOS.

Figure 1.7 shows the improvement of precision in the value of θ_{13} when compared to future experiments. The plot shows calculated 90% confidence limits of the J-PARC-SuperKamiokande project; NUMI, a high energy off axis experiment; a projected future megaton water Cerenkov detector, J-PARC-HyperKamiokande; and two neutrino factory designs, one of which is a low energy facility without muon cooling. The left-most ends of the bars show the pure statistical sensitivity. The range of values allowed by the data increases when taking into account correlations with other oscillation parameters, but the neutrino factory also gives a first observation of $\nu_e \rightarrow \nu_\tau$ oscillations, which can be used with the study of wrong signed muons to remove these correlation systematics. Overall the neutrino factory would outperform conventional neutrino beams by about two orders of magnitude.

Also, the determination of ν_μ to ν_τ to high statistics will confirm what has already been observed in atmospheric neutrino experiments and is due to be further tested in up-coming accelerator experiments. It is important since it puts constraints on all of the appearance channels so that the unitarity of the mixing matrix can be checked. However what makes a neutrino factory tough to create is the need to store a very high number of muons in the storage ring, ideally 10^{20} per year [25].

1.2.7 Matter effects

So far discussion on neutrino oscillation has assumed that it takes place in vacuum. If matter is present then, because neutrinos can interact with matter, the oscillation probability changes. The probability of ν_e interacting with electrons is different to that of ν_μ or ν_τ, since in the first case the interaction can proceed through CC or NC weak interactions, whilst

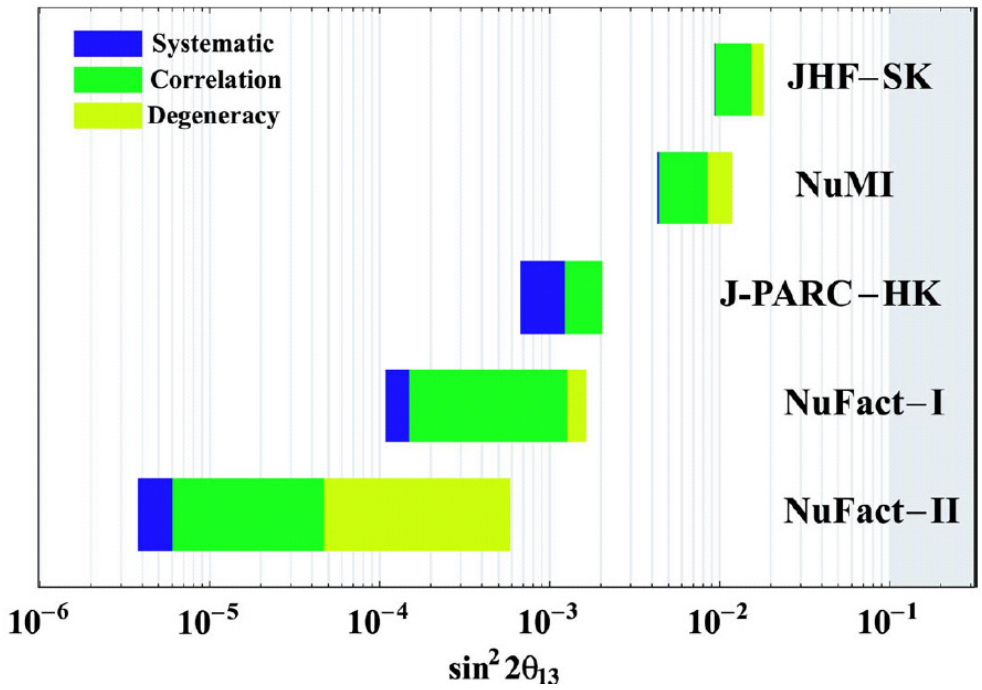

Figure 1.7: Sensitivity to mixing angle for various neutrino experiments [22].

in the second it can only occur through NC because of flavour constraints. Therefore the refractive indexes of ν_e and $\nu_{\mu,\tau}$ are not the same. So, if oscillation occurs, the differing refractive indexes are significant, for instance in the sun where the electron density is not constant [14].

Matter effects also offer a valuable physics channel to the neutrino factory. A study of the first direct observation of $\nu_e \rightarrow \nu_\mu$ also allows the determination of the sign of Δm^2_{23} and hence can remove the ambiguity from the mass hierarchy scheme. To do so it is necessary to detect wrong sign muons for the cases of having μ^+ and μ^- in the storage ring. If $\Delta m^2_{23} < 0$ there should be fewer wrong sign muons observed when positive muons are stored than when negative muons are stored. Conversely, for $\Delta m^2_{23} > 0$ there should be higher wrong sign muon rate when positive muons are stored. Hence measuring the two spectra gives a definite measure of the sign of Δm^2_{23}. A simulation performed by Barger et al [26] illustrates the differences in the spectra for the two cases of initial muon charge, see figure 1.8.

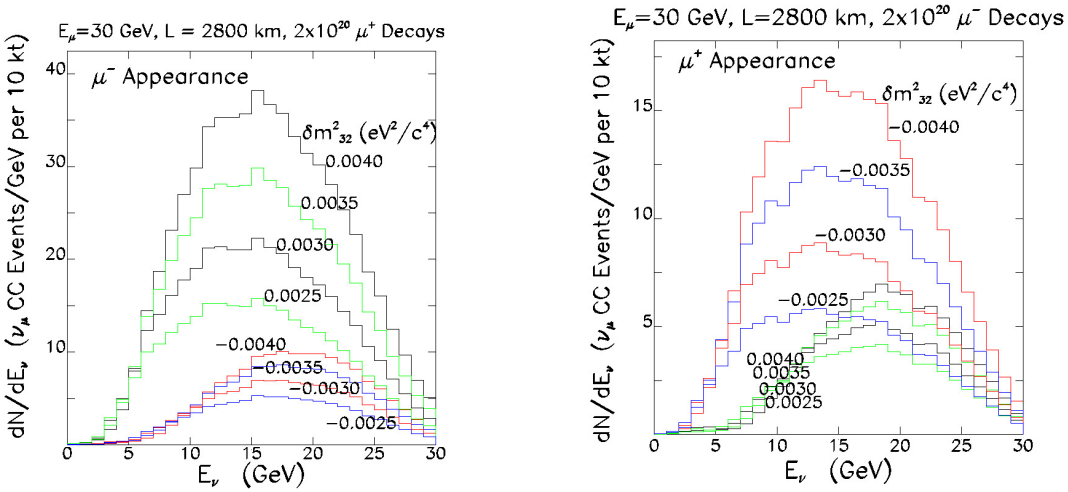

Figure 1.8: The left hand plot shows the predicted energy spectra of wrong sign muon tagged CC events for various δm^2_{32} values with positive muons in the storage ring. The right hand plot shows the same thing for negative muons in the storage ring. The differences in spectra for the two mass hierarchies are clearly visible [26].

1.2.8 Leptonic CP violation searches

CP violation in neutrino physics could be caused by either the Dirac phase or the Majorana phase. However flavour neutrino oscillations are insensitive to the Majorana CP violating phases [27]. Like matter effects, CP Violation in the neutrino sector modifies the measured $\nu_e \leftrightarrow \nu_\mu$ oscillation. Figure 1.9 shows the predicted ratio of $N(\bar{\nu_e} \rightarrow \bar{\nu_\mu})/N(\nu_e \rightarrow \nu_\mu)$ at a neutrino factory [22]. For a fixed energy, with no CP violation or matter effects, this ratio should be 0.5 because of the different cross sections involved. As the baseline increases the ratio is enhanced or suppressed by matter effects depending on the sign of Δm^2_{23}. The width of the bands shows the change in the phase from $-\frac{\pi}{2}$ to $+\frac{\pi}{2}$. At long distance the matter effects dominate over possible CP violation. However with a baseline of a few thousand kilometers, precise measurements of the ratio could be sensitive to CP violating effects.

1.2.9 Other physics potential

Varied physics can be carried out with a neutrino factory, which can be divided into two categories: physics potential arising from the neutrino beam itself, and physics arising from the other parts that make up the facility. For instance, an intense beam of muons allows the study of rare muon decay modes. The flux of such a beam is typically three or four times

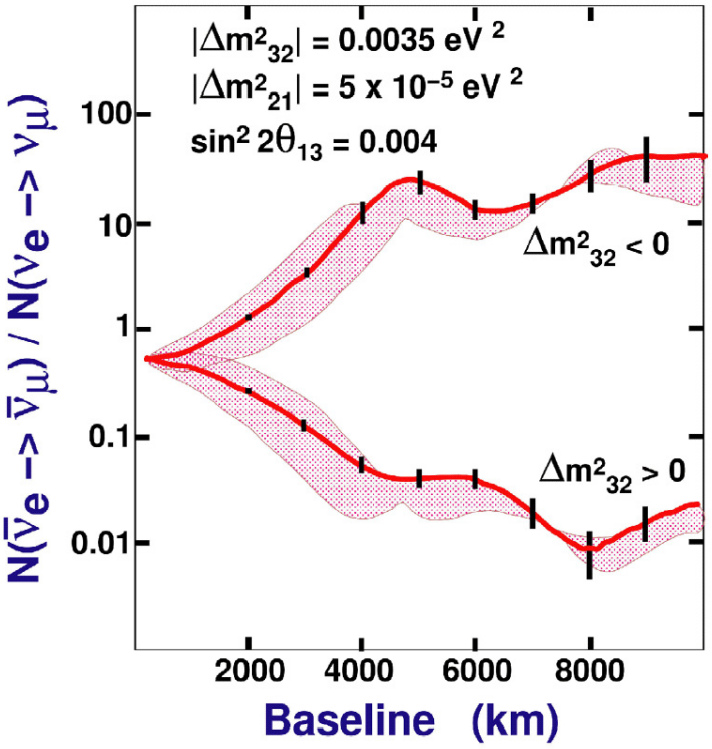

Figure 1.9: The difference between the number of wrong sign muon events seen by a detector for different mass hierarchy, assuming a given value of θ_{13} and mass differences [22].

that of any existing or proposed source [22]. Rare muon decay modes are a stringent test on the standard model; additionally, standard model parameters, such as muon lifetime and magnetic moment, are measurable to an unprecedented accuracy.

Deep inelastic scattering on protons with an intense neutrino beam allows separate measurements of the effects of valence quarks and sea quarks across a high range of the Bjorken scaling variable [28]. Current experiments using neutrinos from pion decay are blighted by poor knowledge of the energy spectrum, the large nuclear targets required, and the contamination of neutrinos and anti-neutrinos. Traditional neutrino deep inelastic scattering experiments produce global fits for parton distribution functions. A neutrino beam from a neutrino factory allows the determination of the individual parton distributions for all light quarks and anti-quarks. The determination of the strong coupling constant is possible from observing the scaling violations of the structure functions (neutrinos do not couple directly to gluons). Measuring elastic scattering of neutrinos on electrons, or neutrinos on nucleons, allow a calculation of the weak mixing angle θ_W with a precision of around 0.0001 (a factor of twenty improvement on the current best) [15].

1.3 The muon collider

1.3.1 Electroweak unification and symmetry breaking

The idea that all forces are a manifestation of one ultimate force has always been popular. Newton postulated that the force of gravity behind everyday mechanics on earth is the same force that holds planets in place. Maxwell proved that electricity and magnetism are part of the same phenomenon, electromagnetism. Einstein showed that time and space were part of the same four dimensional space-time. In the second half of the twentieth century scientists began to theorise ways of making a gauge invariant quantum field description of the interaction behind radioactivity, the weak force. Unlike the electromagnetic force, which appeals to gauge invariance to formulate a re-normalisable field theory, early weak theory using an intermediate vector boson formalism contained divergences.

To remove these, the natural first prescription is to take an analogous view to quantum electrodynamics, except with the charged current weak force being carried by the W boson instead of the photon. However weak theory deals with two new charges on top of the electric charge (Q): the weak isospin charge (I^W) and the weak hyper-charge (Y). The three are related through Y = Q/e - I_3^W so that conservation of electric charge and weak isospin charge implies conservation of hyper-charge. The hyper-charge conservation also follows from acting with a unitary phase transformation on the free lepton Lagrangian density.

The weak isospin charge, I_3^W, is a neutral current, which appears naturally from expressing the weak interaction through two dimensional special unitary operators, SU(2). This neutral current couples either electrically neutral leptons, or electrically charged leptons to one another. The charged currents also couple charged leptons to neutral leptons. Apart from a constant factor the neutral weak isospin current contains an electromagnetic current term in it:

Neutral weak isocurrent, $J_3^\alpha = \frac{1}{2}[\bar{\Psi}_{\nu_l}^L(x)\gamma^\alpha\Psi_{\nu_l}^L(x) - \bar{\Psi}_l^L(x)\gamma^\alpha\Psi_l^L(x)]$,

Electromagnetic current, $s^\alpha = -e\bar{\Psi}_l(x)\gamma^\alpha\Psi_l(x)$.

Thus a deep connection between the two currents is evident, although there is a very obvious difference between the weak and the EM force; namely, that the EM force acts over vast distance scales whilst the weak forces are confined to within atomic radii. Defining a

field invariant under U(1) transformation and a field invariant under SU(2) transformation, it is possible to write down a leptonic Lagrangian that is invariant to both and hence also the action of the weak isospin and hyper-charge currents (SU(2)xU(1)). With properly chosen couplings the photon and Z boson fields are a mixture of these two invariant isospin and hyper-charge fields (which are not observed). Thus the electroweak unification is complete, and conclusive experimental evidence (excluding a zero value of the Weinberg angle) exists to support the theory [29].

The difference in range of the weak and electromagnetic force is because the weak bosons are massive, while the photon is massless. But gauge invariance implies that fundamental gauge bosons are massless (like photons and gluons and the bosons in the unification scheme just detailed). Clearly, this is not true for what is observed in the electroweak sector; somehow, W and Z bosons have acquired a large mass. The mechanism that accounts for this is called spontaneous symmetry breaking. An analogy occurs in the spontaneous magnetisation of iron: the forces that couple the spin are rotationally invariant, yet in the ground-state they must point in some specific direction resulting in magnetisation. To obtain spontaneous symmetry breaking in a system requires the following:

1. Excited states of the system are unique and gauge invariant under transformations.

2. The ground state of the system is degenerate and hence has no gauge invariance.

3. On arbitrarily selecting one of the ground states the symmetry is lost.

The ground state in field theory is the vacuum. Hence this must be a degenerate state; it must have a non zero expectation value in the new field that will break the symmetry in the electroweak sector. The Higgs boson was theorised as carrying the required field. It is a spin 0 particle, and its field has a non-zero expectation value in the vacuum. Applying the Higgs mechanism to SU(2)×U(1) leads to the creation of one massless boson (the photon, as required), and four massive bosons (the three weak bosons and the Higgs itself). Interestingly, the coupling of the Higgs in the new Lagrangian is proportional to mass, so that heavier particles couple more strongly to the Higgs field. Hence the vacuum should be full of massive Higgs bosons that particles will interact with, and it is the interaction with this field that gives mass to the standard model particles.

However although low energy couplings and fermion masses are logarithmically sensitive

to some energy scale λ, where the standard model breaks down and a more fundamental theory takes hold, all scalar squared-masses are quadratically sensitive to λ. Thus the mass of the standard model Higgs depends on a bare-mass from the fundamental theory and the quadratic correction. Since these two contributions are from separate sources it is unlikely that the standard model mass is significantly smaller than either [30]; the mass of the physical Higgs should be at least of order λ^2. If λ is not around the electroweak symmetry breaking scale, 1 TeV, the only way to have a Higgs mass around M_Z is to have an unnatural cancellation between the bare mass and the quadratic dependence. This seems unlikely since the two have different origins. Super-symmetry solves this problem by postulating a super-symmetric partner for each fermion and boson that exists. But since these particles are not observed this is not an exact symmetry and should have a breaking scale of less than a few TeV to avoid the same fine tuning problems.

1.3.2 Studying the Higgs

The Large Hadron Collider (LHC) is expected to begin running within the next five years. It has a center of mass energy of 14 TeV and expects to detect the Higgs boson and perhaps super-symmetric particles. This is because in standard Higgs formalism,

$$M_H = \sqrt{2\lambda}V,$$

where V is part of the vacuum expectation value and is constrained from the mass of the W and Z boson to be 246 GeV [31]. If value of λ is too large it will make the theory non-perturbative (theoretically, if not physically, undesirable). By looking at the re-normalisation group evolution equation, it is possible to fix the value to keep the theory perturbative up to at least $Q^2 = M_H^2$ which gives an upper bound on the mass of the Higgs based on unitarity constraints and the scattering of longitudinal W and Z bosons of $M_H < 800$ GeV. Similarly, from the same re-normalisation group equation a lower bound on the mass of the Higgs is found to be $M_H > 70$ GeV, see figure 1.10.

It is also possible to use loop corrections involving Higgs bosons to further constrain the mass. This is the same approach that led to the prediction of the mass of the top quark in electroweak physics, however the dependence on the Higgs mass is not as strong so more data is required. In the summer of 2004 the LEP + SLD Electroweak working group reported $M_H = 114^{+69}_{-45}$ GeV and $M_H < 260$ GeV to 95% confidence [32].

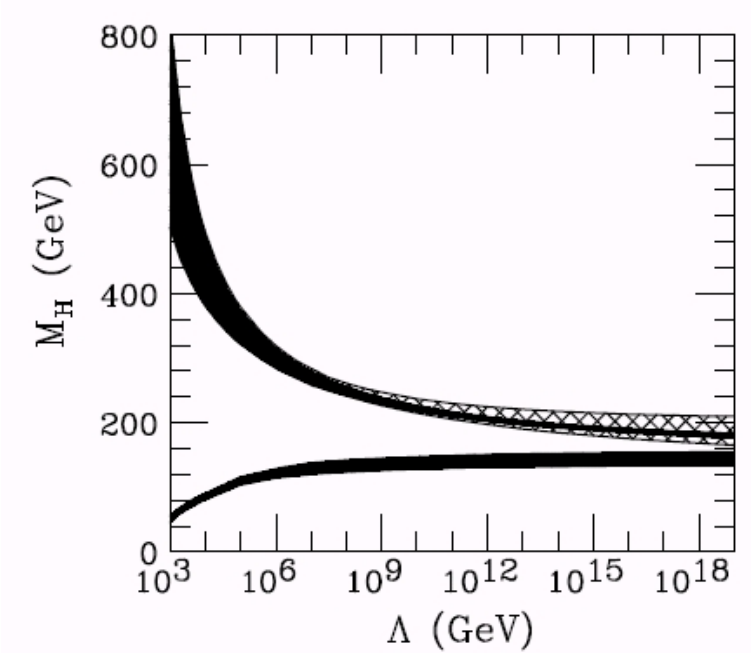

Figure 1.10: Combined bounds for the Higgs mass as a function of scale λ up to which theory is perturbative and the vacuum is stable [31].

The mass of the Higgs seems to be in a range that is just outside the reach of current machines. But alongside the high mass, the Higgs couplings make it hard to produce, let alone infer its presence in detectors. Historic and future searches are summarised in table 1.2. The LEP energy would have enabled the Higgs to be found with a mass of up to $M_{H,max} \approx \sqrt{s} - M_Z = 115$ GeV.

Unfortunately, the energy of LEP was limited by synchrotron radiation. While electron machines have an advantage over hadron machines due to the point-like nature of leptons (there is reduced background, and the fundamental electron takes the full center of mass energy in a collision), a circular collider is handicapped by synchrotron radiation, which is the radiation necessarily produced by a relativistic accelerating charge. Quantitatively, it is possible to express the instantaneous radiated power per turn in a circular collider (the power radiated is a factor γ^2 larger than in linear acceleration since the velocity acceleration cross product does not vanish) [33].

$$P = \frac{2}{3}\frac{e^2}{4\pi\epsilon_0 m^2 c^3}\frac{\beta^4\gamma^4}{\rho^2}$$

The instantaneous loss is very small - only 7 μW for LEP at 100 GeV. But the total energy loss per turn is the integral of this around the radius of curvature ρ. This is over 2

Collider	Process	Max $\sqrt{s}$	experiments	status
SLC	e^+e^-	100 GeV	SLD	finished 1998
LEP	e^+e^-	208 GeV	Aleph, Delphi, Opal	finished 2000
HERA	ep	330 GeV	H1, Zeus	running
Tevatron	$p\bar{p}$	1.96 TeV	CDF, D0	running
LHC	pp	14 TeV	Atlas, CMS, LHCb, Alice	future

Table 1.2: Experiments that have and will search for the Higgs boson

GeV for LEP [34], which is a large amount of energy lost from the ring each turn making it inefficient to go to higher energy. The next experiments to look for Higgs used heavier protons and anti-protons instead of electrons.

The Tevatron is a proton-anti proton collider at Fermilab. It can reach a much higher energy than LEP, but due to the three quark nature of protons, all of this energy is not available in a hard collision. The Higgs is an electroweak particle, but quarks interact via the strong force. Instead of a clean signal, the initial partons can emit QCD radiation, and the remnants of the collided hadrons can interact. The largest production channel for the Higgs is two gluons. The cross section for this (for a 115 GeV Higgs) is roughly one picobarn, compared with the total proton cross section of 30 millibarn emphasises how hard it is to detect the Higgs in the Tevatron or LHC. A high luminosity is necessary to reduce the signal-to-noise ratio. It is also important to have good acceptance for leptons in the detector and to be able to tag bottom quarks. If a Higgs candidate is discovered it is essential to be able to test that it is truly a Higgs by looking at how it couples to leptons, bosons, and like particles. The next linear collider, an electron-positron machine, could do this task if the LHC discovers the Higgs (The LHC is not a clean enough environment to study the various couplings itself).

So if physics beyond the standard model appears through new particles in electroweak symmetry breaking, or in the super-symmetric sector, precise measurements of their properties will be required to explain the underlying processes. High background rules out using protons, and synchrotron radiation makes using electrons undesirable in circular colliders. Muons do not suffer either of these problems: they are point-like and have a mass two hundred times greater than the electron, which means that the coupling with the Higgs would be larger. Thus a circular lepton collider using muons could go to larger energy and offer a larger Higgs production channel. Building such a collider is a natural progression from

putting muons into a storage ring to create a neutrino factory.

1.4 Summary

The standard model is a thorough description of much of the subatomic world, but it is not the final answer. In electroweak physics there have been many surprises, for example neutrinos seem to oscillate in vacuum, suggesting they have mass. At present only loose limits on neutrino mass are available, and the hierarchy is not known. The overall implication of the nature of neutrinos on the lepton sector is important; if neutrinos are Majorana particles leptonic charge is not strictly conserved. The unification of electromagnetism and the weak force was a triumph of particle physics, but questions about the origins of mass led to the postulation of a particle that has still not been observed. And while super-symmetry has been suggested as a way to solve the mass hierarchy problem and unify all the fundamental forces, no experiment has yet had a high enough range of energy to see super-symmetric particles.

In order to test hints of physics lying outside of the standard model it will be necessary to use muons: neutrino factories consisting of a storage ring of muons will give important insight into neutrino oscillation parameters, masses, and leptonic CP violation; while building a muon collider offers a greater energy reach than any present experiment for studying the Higgs boson and precision measurements of any super-symmetric particles discovered.

However muons are hard to store. They must be produced in pion decays and are short lived, decaying in microseconds. The nature of their production means that any beam of muons will have large transverse divergence in momentum. The transverse size of the beam must be reduced so that the muons fit into a storage ring for a neutrino factory, and reduced further to achieve a good luminosity if they are to be collided. At the same time the particles need to be kept into longitudinal bunches so that they can be re-accelerated. These requirements present their own problems. A neutrino factory would need of order 10^{20} muons stored and decaying in a ring per year in order to operate to the required sensitivity.

Chapter 2

Muon ionisation cooling

Muons produced from pion decay have a large and diffuse phase space density. To fit inside a typical accelerating aperture, the transverse size of the beam must be reduced by orders of magnitude and at the same time the muons must fit longitudinally into an RF bucket for acceleration. Muons require prompt, six dimensional cooling. Transverse cooling could be achieved using a technique where muons are passed through absorbers and then re-accelerated in RF cavities. This so-called ionisation cooling is a theoretical concept to date. A muon ionisation cooling experiment (MICE) has been proposed at the Rutherford Appleton Laboratory. This chapter outlines the theory behind muon cooling, derives emittance equations and evaluates the suitability of various materials. It then examines the MICE experimental set-up, looks at techniques for longitudinal and six dimensional cooling, and discusses the potential problems of simulating MICE and other cooling schemes.

2.1 The principle of ionisation cooling

Muon cooling is necessary for both a neutrino factory and a muon collider. Affecting both machines is the need to get a diffuse muon beam to fit inside the aperture of a storage ring before the muons decay. A collider has an additional constraint that the luminosity of the machine is dependent on how tight the beam is focused.

For a three dimensional system of positions and momenta, related through first order differential equations, the phase space describes possible values of (x, y, z, p_x, p_y, p_z). This phase space must be reduced for a neutrino factory or muon collider to work. However Liouville's theorem [35] states that conservative forces cannot increase or decrease the volume occupied by a beam in phase space - a focusing quadropole can decrease the area of a charged particle beam, but at the same time it will increase its transverse momentum spread. Focusing does not reduce the phase space density at all; what is needed is a way to reduce both the beam's size and divergence i.e. to cool the beam. In this work the x, y plane is taken to be transverse when discussing emittance, which is not the same x used conventionally to

refer to $\mathrm{d}E/\mathrm{d}x$ along the direction of motion.

The short life of muons rules out conventional beam cooling methods, however a technique first proposed in 1981 [36] that suggest passing the beam through absorbers before restoring longitudinal momentum in RF cavities is feasible. It is equivalent to a thermodynamic compression doing work on a beam under isothermal conditions. This method of ionisation cooling is a violation of Liouville's theorem, achieved by using energy loss. The transverse phase space coordinates of a beam can be reduced by passing the beam through an absorber, where the particles lose energy along their direction of motion, and then restoring the lost energy in the longitudinal component of momentum using acceleration. But when charged particles pass through the absorber they experience both energy loss and multiple scattering. Whilst the former does not affect the beam divergence to first order, the latter will, see figure 2.1. A material is needed that has low multiple scattering and high energy loss. The best material is one with low atomic number.

As the transverse phase space is reduced, the longitudinal phase space grows because of three factors:

1. The energy loss fluctuations in the absorber (straggling) cause an increased spread in energy.

2. The negative slope of the energy loss curve also causes an increased spread in energy (fast muons lose less energy than slower ones).

3. The particles themselves have a range of velocities so the bunch lengthens over time.

Cooling is carried out near to the energy loss minimum (a momentum around 200 MeV/c for muons in liquid hydrogen, see figure 2.2) since to cool at lower momenta means that the energy loss curve is rapidly decreasing with energy (increasing straggling) and while to cool at higher momenta gives a slight benefit because of the positive slope, the energy needed to restore momenta in the RF increases [38].

A way around the increase in longitudinal phase space that does not depend on cooling at higher momenta is to exchange some of the beam's initial longitudinal size for an increase in the transverse size, which is more readily reduced. This is called emittance exchange [39]. The technique depends on splitting the path of the particles in the beam depending on their energy. A dipole magnet can bend the beam such that the higher energy particles have a

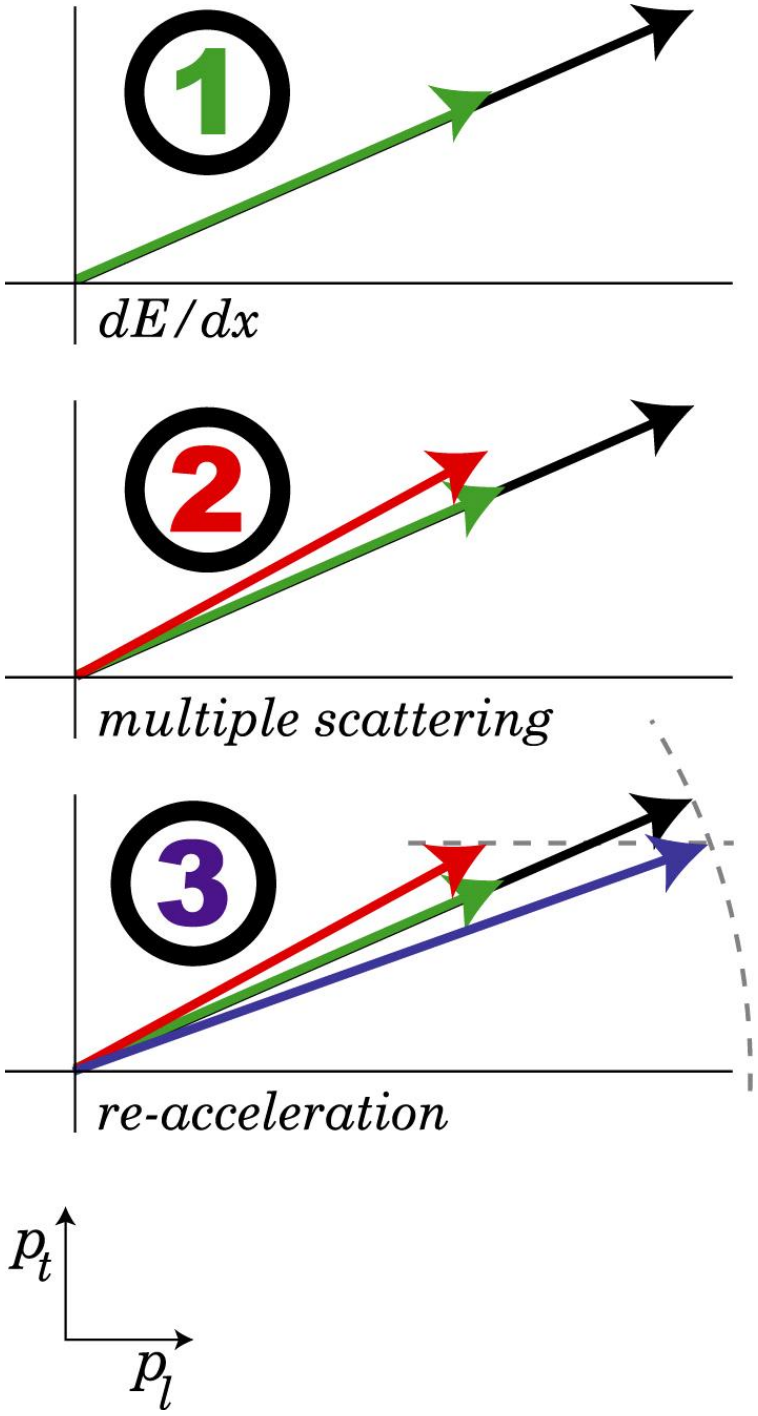

Figure 2.1: A simplified view of muon ionisation cooling [37]: in step 1, the muon loses energy along the direction of motion; at the same time it will also multiple scatter, shown in step 2; step 3 shows that by applying re-acceleration, the result is that the beam has less transverse momentum spread than before. If this process is repeated, gradually the envelope of the beam will focus down to some minimum size.

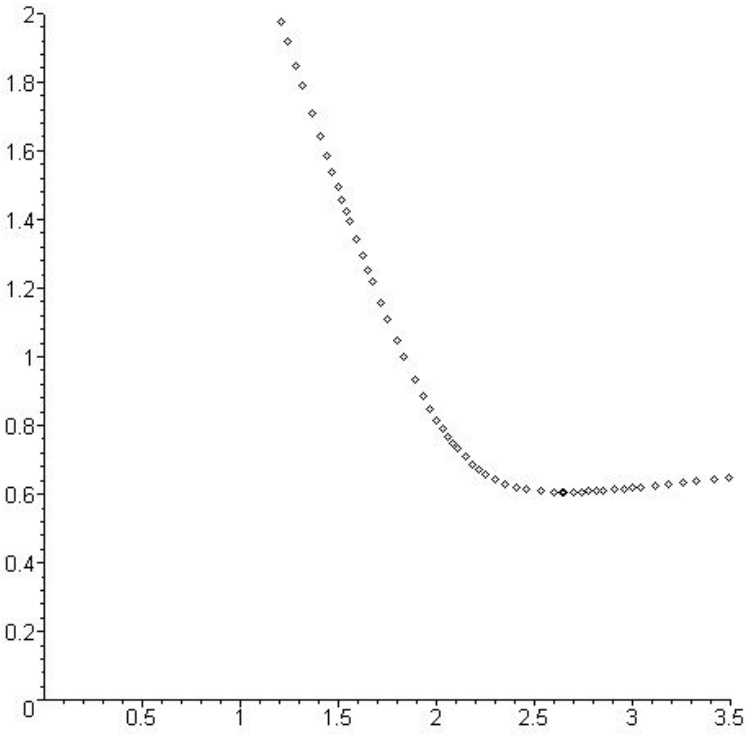

Figure 2.2: Ionisation energy loss ($\mathrm{MeVg^{-1}cm^{-2}}$) against log(momentum) (log MeV/c) for liquid hydrogen, calculated using the Bethe Bloch formula [1].

larger radius of curvature. The beam is thus correlated in momentum and position, and can be passed into a wedge shaped absorber such that the particles with higher energy cross a thicker piece of absorber and lose more energy. The result is that the energy spread of the beam is reduced but the width and hence transverse size of the beam is increased. An alternative is to use a dipole magnet filled with a gaseous absorber so that positive dispersion gives higher energy muons a larger energy loss due to their increased path, see figure 2.3. In general, either technique followed by transverse cooling is equivalent to six-dimensional cooling.

2.2 Emittance

Cooling is discussed quantitatively in terms of emittance [41]. A beam's emittance represents the volume of phase space occupied by the beam. It is defined below, where σ is a root mean square of the property, $i = x, y, z$, and $1/mc$ is introduced to express emittance in units of length [42],

$$\epsilon_{i,n} \equiv \sigma_i \sigma_{p_i} / mc.$$

Figure 2.3: Emittance exchange carried out with a dipole and wedge shaped absorber, or gaseous dipole cavity [40].

The six dimensional normalised emittance is given by $\epsilon_{6,n} \equiv \sqrt{\det \mathrm{V}/(mc)^6}$ where V is the covariance matrix of x, p_x, y, p_y, z, and p_z. Assuming no correlation between the space coordinates and momenta this reduces to $\epsilon_{6,n} = \epsilon_{x,n}\epsilon_{y,n}\epsilon_{z,n}$. The relationship between these normalised emittances and the unnormalised emittance is,

$$\epsilon_n \equiv \beta\gamma\epsilon.$$

The transverse beam sizes in terms of the emittance are,

$$\sigma_x^2 = \beta_x\epsilon_x \qquad \sigma_y^2 = \beta_y\epsilon_y,$$

where β_x and β_y are the transverse optical function [43] of the focusing lattice in the x and y direction, a low β_i corresponding to strong focusing in that direction.

It is important to note that although emittance is a strictly conserved quantity in the absence of material, normalised emittance is not conserved if there is a spread of P_z in a beam and will grow even in a drift space due to energy straggling effects [44].

2.2.1 Cooling derivation

Cooling a beam corresponds to a reduction of emittance. Thus differentiating the normalised emittance to quantify the change in emittance inside an absorber gives,

$$\frac{d\epsilon_n}{dz} = \beta\gamma\frac{d\epsilon}{dz} + \epsilon\frac{d\beta\gamma}{dz}. \tag{2.1}$$

Now using the relation,

$$\frac{d\beta\gamma}{dz} = \frac{1}{\beta mc^2}\frac{dE}{dz}, \tag{2.2}$$

the second term represents the energy loss in the absorber [45]. This can be re-written in a recognizable form using the emittance relations and $E = \gamma mc^2$ leaving,

$$\frac{d\epsilon_n}{dz} = \beta\gamma\frac{d\epsilon}{dz} - \frac{\epsilon_n}{\beta^2 E}\langle\frac{dE}{dz}\rangle, \tag{2.3}$$

where the $\langle dE/dz\rangle$ represents the average energy loss. The first term in 2.3 can be expanded in terms of the covariance matrix definition of emittance [41], noting that,

$$\frac{d\epsilon}{dz} \equiv \frac{1}{2\epsilon}\frac{d\epsilon^2}{dz}. \tag{2.4}$$

Thus in the x-$x\prime$ plane,

$$\epsilon^2 = \text{ det V } = \det\begin{pmatrix} \sigma_{xx} & \sigma_{xx\prime} \\ \sigma_{xx\prime} & \sigma_{x\prime x\prime} \end{pmatrix} = \sigma_{xx}\sigma_{x\prime x\prime} - \sigma_{xx\prime}^2. \tag{2.5}$$

Performing the differentiation of ϵ^2 then gives,

$$\beta\gamma\frac{d\epsilon}{dz} = \frac{\beta\gamma}{2\epsilon}\frac{d\epsilon^2}{dz} = \frac{\beta\gamma}{2\epsilon}\left(\sigma_{xx}\frac{d\sigma_{x\prime x\prime}}{dz} + \sigma_{x\prime x\prime}\frac{d\sigma_{xx}}{dz} - 2\sigma_{xx\prime}\frac{d\sigma_{xx\prime}}{dz}\right). \tag{2.6}$$

The terms in the bracket represent the evolution of the moments of the optical function, which can be expanded to become,

$$\frac{d\sigma_{xx}}{dz} = 2\sigma_{xx\prime},$$

$$\frac{d\sigma_{xx\prime}}{dz} = \sigma_{x\prime x\prime} - k^2\sigma_{xx},$$

$$\frac{d\sigma_{x\prime x\prime}}{dz} = \sigma_{x\prime x\prime} - 2k^2\sigma_{xx\prime},$$

where k^2 is the focusing strength [46]. Hence,

$$\beta\gamma\frac{d\epsilon}{dz} = \frac{\beta\gamma}{2\epsilon}\left(\sigma_{xx}(\sigma_{x\prime x\prime} - 2k^2\sigma_{xx\prime}) + \sigma_{x\prime x\prime}(2\sigma_{xx\prime}) - 2\sigma_{xx\prime}(\sigma_{x\prime x\prime} - k^2\sigma_{xx}\right). \tag{2.7}$$

Note that the covariance matrix V can be written in terms of the Twiss parameters so that $\text{V} = \epsilon\begin{pmatrix} \beta_[t] & -\alpha \\ -\alpha & \gamma \end{pmatrix}$, and $\sigma_{xx} = \epsilon\beta_t$. And also that $\sigma_{x\prime x\prime} = \sigma_\theta^2$. Hence the first term in the brackets of equation 2.6 represents multiple scattering. The second and third terms cancel with the help of the first. This leaves,

$$\beta\gamma\frac{d\epsilon}{dz} = \frac{\beta\gamma}{2}\left(\beta_t\sigma_\theta^2\right). \tag{2.8}$$

In the Gaussian approximation the change in angle is represented by a projected scattering,

$$\sigma_\theta^2 = \left(\frac{14[MeV]}{\beta cp}\right)^2 \frac{z}{L_R}, \tag{2.9}$$

where L_R is the radiation length [45]. Making this substitution and using relativistic relations allows the common form for the change of emittance to be reproduced:

$$\frac{d\epsilon_n}{dz} = -\frac{\epsilon_n}{\beta^2 E}\langle\frac{dE}{dx}\rangle + \frac{\beta_t(14MeV)^2}{2\beta^3 E m_\mu L_R}. \tag{2.10}$$

The equation contains two terms; the first reduces emittance, while the second increases it. These are the cooling and heating terms. Clearly the cooling term must be greater than the heating term for net cooling to occur; ideally, a material with a high ionisation energy loss and a large radiation length (low scattering) is required. Qualitatively the Z^2 dependence of $1/L_R$ compared to the Z dependence of dE/dx suggests using a low Z material.

2.2.2 Comparing absorber materials

In order to evaluate the suitability of various absorbers it is possible to write the cooling and heating equation in terms of an equilibrium emittance, ϵ_{n_∞}, and a cooling length, λ, defined by,

$$\frac{d\epsilon_n}{dz} = \frac{-\epsilon_n}{\lambda} + \frac{\epsilon_{n_\infty}}{\lambda}, \tag{2.11}$$

where,

$$\lambda = \beta^2 E\langle\frac{dE}{dz}\rangle^{-1} \qquad \epsilon_{n_\infty} = \frac{\beta_t(14MeV)^2}{2\beta m_\mu L_R}\langle\frac{dE}{dx}\rangle^{-1}.$$

For a fixed β_t the figure of merit is thus $L_R\langle\frac{dE}{dx}\rangle$ – a higher number gives more cooling. The suitability of several different materials is shown in table 2.1. The relative 4-D cooling is calculated as the ratio of the equilibrium emittance to that of hydrogen. Hydrogen offers the most cooling, and the relative cooling decreases with increasing Z. However this is not the full story, since by its nature hydrogen must be contained in a material with a higher atomic number. Liquid hydrogen (LH_2) requires cryogenics and windows, while gaseous hydrogen requires high density and even thicker windows. Studies have shown that a liquid hydrogen absorber contained in thin aluminium windows would lower the relative cooling to between 0.65 and 0.8 [46], which is still the best cooling performance (however there is a serious issue of heat dissipation in hydrogen, because the intense beam of muons with a rate of roughly few$\times 10^{14}$ per second entering each absorber deposits around 600 Watts). Li and LiH are

Material	Z	Density gcm^{-3}	$\langle\frac{dE}{dX}\rangle$ $MeVg^{-1}cm^2$	L_R gcm^{-2}	$\langle\frac{dE}{dX}\rangle L_R$ MeV	Relative 4-D Cooling
H	1	0.0708	4.12	61.3	252.6	1.0
He	2	0.1249	1.94	94.3	182.9	0.524
Li	3	0.534	1.58	82.8	130.8	0.268
LiH		0.78	1.89	79.3	149.9	0.352
Be	4	1.848	1.61	65.2	104.9	0.172
C	6	2.265	1.78	42.7	76.0	0.091
Ar	18	0.0018	1.52	19.6	29.6	0.014
Pb	82	11.4	1.12	6.37	7.1	0.001

Table 2.1: Candidate cooling materials and their performance.

solid, but require a lower β_t for the same equilibrium emittance. On top of the containment and safety concerns there is a lack of accurate data for the scattering of muons in a hydrogen absorber, although new data on muon scattering in liquid hydrogen has recently been taken by MUSCAT and will be examined in chapter 5.

2.3 MICE

Getting muon ionisation cooling right is important for the performance of a neutrino factory, because of the complicated cryogenic and RF set-up, it is also one of the major costs. In 2003 a proposal was submitted to the United Kingdom's Rutherford Appleton Laboratory (RAL) for a muon ionisation cooling experiment (MICE [22]). The aim was to show that it is possible to make a cooling channel that gives the desired performance for a neutrino factory, and to investigate various conditions to give limits to the feasibility.

2.3.1 Overview

The MICE experiment is a section of a full cooling channel, consisting of three liquid hydrogen absorbers and two sets of accelerating cavities in a magnetic channel (four cavities per set). In effect this gives two complete cooling cells, with the third absorber being in place for symmetry reasons and to absorb any dark currents from the cavities that would produce x-rays affecting the particle trackers. The experiment has spectrometers at each end to measure the properties of the muon beam, which is obtained on site from the RAL synchrotron (ISIS).

The main parts of the experiment are shown in figure 2.4: the incoming muons encounter a lead diffuser that tunes the input emittance; a time of flight measurement acts as a particle identification; a spectrometer measures the position, angle and momentum, followed by the cooling channel itself. The cooling section is from the first part of the 201 MHz cooling channel of the US feasability study II [24]. Superconducting coils provide the focusing, such that the magnetic field changes sign at the center of each absorber. After the cooling section, the position, angle, and momentum of the outgoing particles are measured, while particle identification by means of a Cerenkov counter and calorimeter eliminates muons that have decayed in the apparatus.

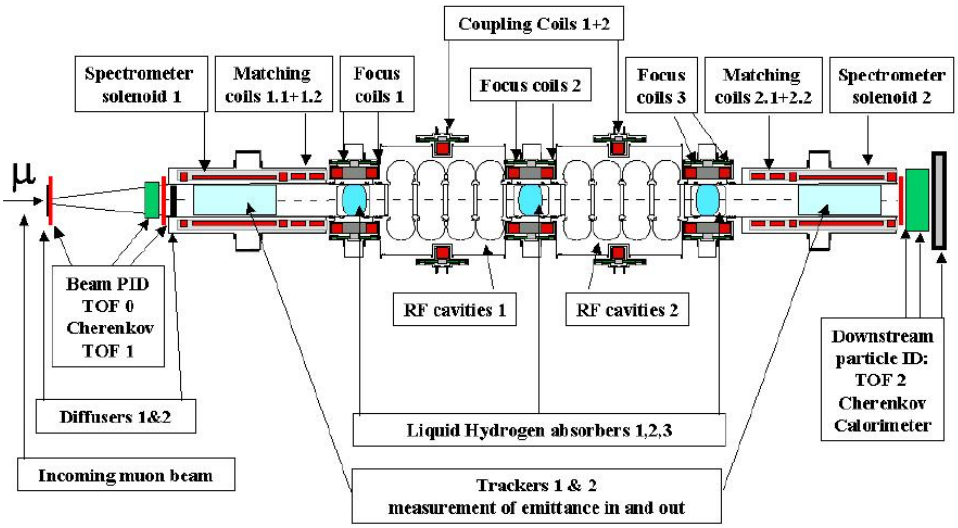

Figure 2.4: An overview of the MICE experiment [22].

2.3.2 Production and selection of muons

At RAL there is a 800 MeV proton synchrotron, ISIS. This uses a Penning H^- ion source and accelerates the ions along a 665 kV channel before injection into the main ring in pulses 200 μs long. When entering the synchrotron an aluminium oxide stripping foil removes the electrons from the ions, leaving protons, which are put into two bunches and accelerated to the full energy. Prior to extraction the bunches become 100 ns long and are separated by 230 ns. To produce the muon beam for MICE, on selected pulses, a small titanium target (10x10x1 mm^3) will dip into the outer halo of the proton beam just before extraction. Pions produced in this collision emerge through a thin window towards the muon beam line, see

figure 2.5.

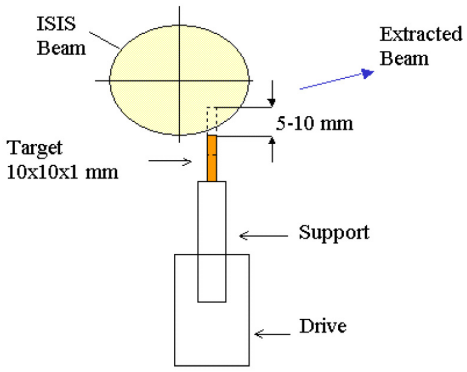

Figure 2.5: A target to produce the MICE muon beam from the ISIS synchrotron. Seen along the direction of the ISIS beam [22].

2.3.3 Absorbers

MICE uses three liquid hydrogen absorbers placed in a large gradient focusing magnetic field to minimise heating. Each absorber measures 35cm and has a diameter of 30cm, holding 21 litres of liquid hydrogen, see figure 2.6. All three contain two sets of windows with a vacuum between them. The design of the container aims to minimise multiple scattering, maintain a uniform absorber temperature, and operate safely. They are designed to handle a heat input of around 100 W. Most of the heating comes from thermal radiation through the RF window at room temperature (15 W), whilst the beam itself and any dark currents contribute less. Each absorber has an internal helium cooled heat exchanger to maintain a stable temperature. A real neutrino factory with a 3×10^{14} muons per second would require absorbers that can withstand more like 500W if an average of 11 MeV is lost per second [47].

2.3.4 RF system and magnetic channel

The purpose of the RF is to keep the muon bunch longitudinally focused and to re-accelerate the individual particles after they have passed through the absorber. Following the design from Study II, MICE uses eight 201 MHz cavities, but due to limited power it will have a gradient of 8 MV/m (opposed to 12 MV/m) and provide a peak voltage of 21 MV [22]. This could be increased temporarily with reduced temperature operation or by applying the power to fewer cavities. To achieve a high shunt impedance the aperture is terminated using

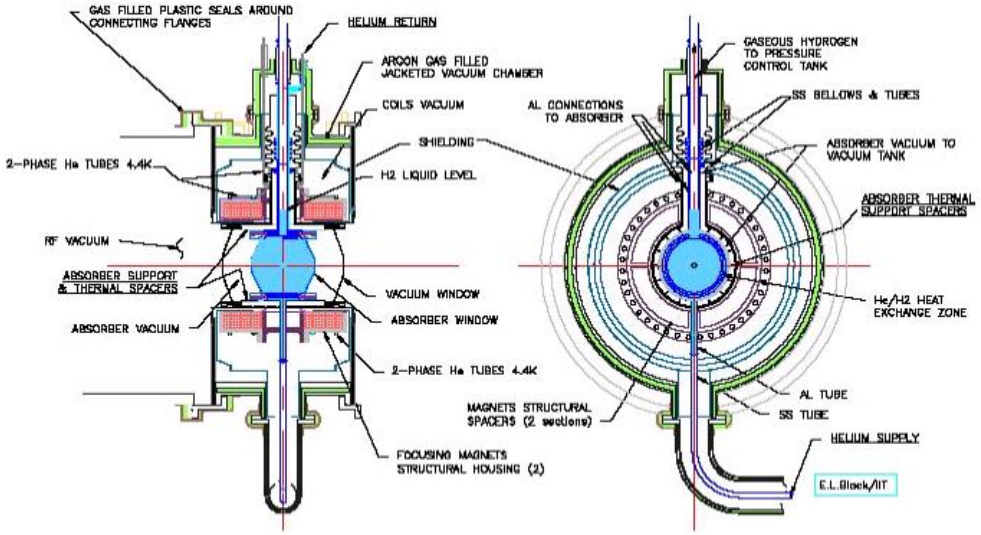

Figure 2.6: A liquid hydrogen absorber that will be used in MICE [22].

	Transverse emittance	Longitudinal emittance
Initial Beam	20 mm rad	2000 mm rad
Neutrino factory constraint	2 mm rad	150 mm rad
Muon collider constraint	50 μm rad	70 mm rad

Table 2.2: Emittance constraints for a neutrino factory and muon collider [49].

thin (1mm) beryllium foil windows, which are almost transparent to muons but present a conducting boundary for the RF-field. A schematic of the RF is shown in figure 2.7.

2.3.5 Performance

The main constraint for a neutrino factory is the acceptance of the storage ring, see table 2.2. A muon collider has an additional constraint since the beam emittance affects the collider luminosity and a high luminosity is important since the collision cross section falls as the square of the energy. Hence the required emittance reduction for a muon collider is higher. The muon collider requires the muon beam to undergo roughly two orders of magnitude reduction in transverse emittance. This is beyond the reach of a lattice like MICE. Though note that downstream acceleration can relax the transverse emittance requirement to order 15 mm [50]. Figure 2.8 shows a simulation of the cooling performance of MICE using a simulation program called ICOOL, which will be discussed in chapter 4. The set up includes the effect of windows and RF, the steep drops correspond to the absorber position and the

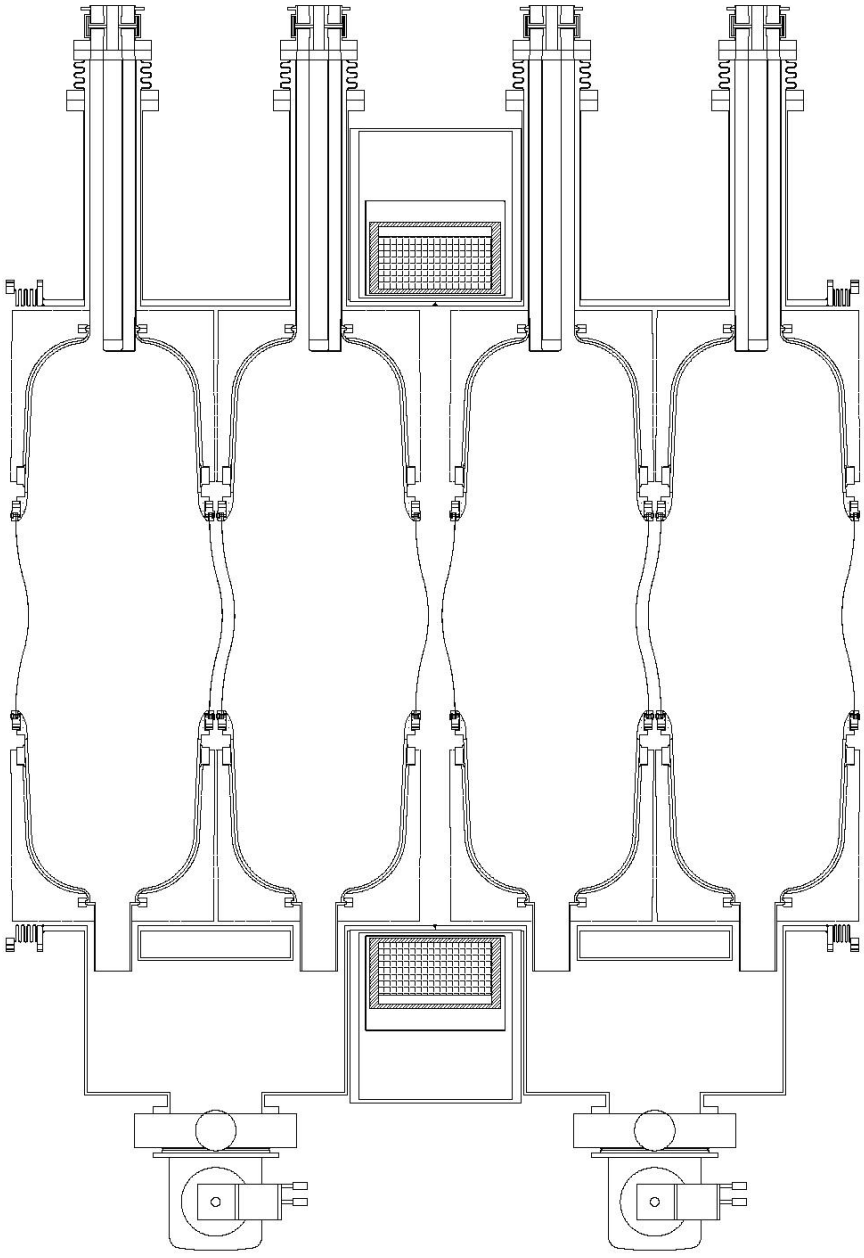

Figure 2.7: The RF system for MICE. The coupling coil is the hatched box on the top and bottom of the diagram and the beryllium windows are shown [48].

slow rises are then the RF re-acceleration, with the effect of the rf taking place in four sections just visible. The reduction in emittance over this length of channel is of order 10%.

Also, a cooling section like MICE does not solve the problem of longitudinal cooling at all, because the energy spread in the beam is increased by transverse cooling. One way of getting around this is by using emittance exchange before transverse cooling. While a linear MICE channel can be extended to any length in principle this is constrained by cost and space, and for a given β_T and material, the equilibrium emittance defines the absolute cooling limit.

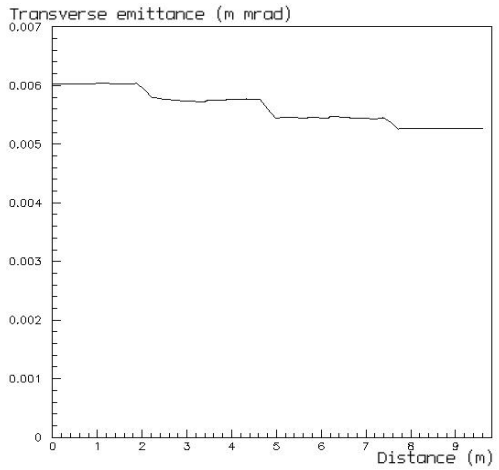

Figure 2.8: A simulation of the cooling performance of MICE using ICOOL.

2.4 Six dimensional cooling: the RFOFO ring

Whilst early studies assumed that transverse cooling and emittance exchange would take place in alternate steps (because the transverse cooling needs a straight channel and the longitudinal requires bending) this produced a problem of matching the two types of cooling lattice. Recently progress has been made with a design achieving simultaneous six dimensional cooling in rings. The most realistic modeling has been done with the RFOFO cooling ring [49]. The RFOFO ring is so named because it consists of a focusing-drift-focusing solenoid lattice (FOFO). The R prefix is nomenclature for the magnetic cell having the same length as the geometric cell.

The RFOFO employs a single cell for doing both transverse cooling and emittance exchange. The ring uses a similar lattice to MICE with the crucial difference being the presence

of bending magnets to give dispersion and wedge absorbers to ensure simultaneous longitudinal cooling. The circular nature means that repeated revolutions can give more cooling at a lower cost. The ring uses solenoidal focusing to increase angular and momentum acceptance. One design has a 33 m circumference made up of twelve identical 2.75 m cells, see figure 2.9.

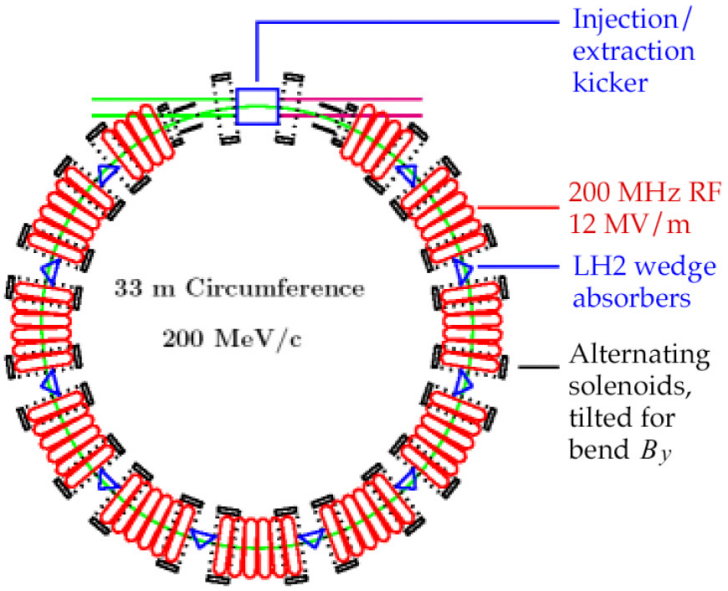

Figure 2.9: A schematic of the RFOFO ring [49].

2.5 The difficulty in simulating muon cooling

With no accurate experimental data on muon cooling, estimates of cooling performance are based on simulations. It is vital for an experiment like MICE not only to to demonstrate cooling, but also to show that simulation codes agree with experiment. MICE is only a section of what might be a long cooling channel for a neutrino factory, and the bridge between the two designs is having confidence in the code used. Hence MICE must be as realistic as possible and incorporate the engineering details simulated in a full cooling channel. Herein lies a problem though, since muon cooling is iterative, any slight discrepancy between simulation and experiment is multiplied up between each absorber and RF.

Unfortunately the energy loss and multiple scattering distributions vital to muon cooling are both non-Gaussian. Talking about the mean square scattering angle, or mean energy loss, is insufficient since both are affected by a large tail, and possibly correlations. The

Particle Data Group expressions for energy loss and multiple scattering are one parameter estimates: the Bethe-Bloch formula incorporates mean ionisation potential and the Moliere distribution uses the radiation length of the absorber material. Scattering is particularly uncertain. The only previous data on the scattering of particles in low Z materials comes from the 1942 experiment carried out by Andrievsky et al. The experiment looked at 2.7 MeV/c electrons on thin strips of material down to Lithium. Results showed that as Z decreased the agreement with Moliere worsened, see figure 2.10.

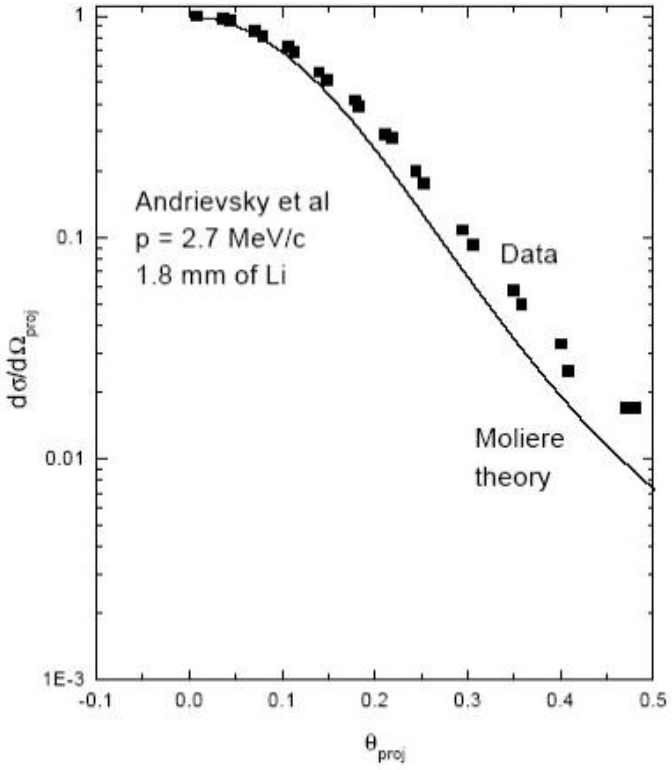

Figure 2.10: Andrievsky et al measurement for electron scattering on lithium [51].

Current estimators of energy loss and multiple scattering are based on models created when today's computing power was not readily available. The simplifications they make are unnecessary and the following chapter outlines a derivation from first principles of the proper cross section for the collisions of charged particles in matter.

2.6 Summary

Muon ionisation cooling is a novel technique to reduce the emittance of a beam of muons by passing the beam through an absorber and then reaccelerating it in the longitudinal direction. It is yet to be shown experimentally although MICE hopes to demonstrate transverse cooling using a section of a full neutrino factory cooling scheme. The language of cooling codes beam dynamics in terms of emittance, the phase space of the beam. The aim of cooling is to reduce the emittance of a beam in six dimensions. By differentiating the description of a beam's emittance it is possible to show that cooling depends on a balance between maximising energy loss and minimising multiple scattering.

Different materials will contribute different amounts of energy loss and scattering, but due to the dependence on atomic number, the best absorber candidates are simple elements with low atomic numbers. Best of all is hydrogen, but this is difficult to employ as it needs to be contained in some vessel before use. However a comparison of various candidates shows that liquid hydrogen plus containment still gives the best cooling performance.

MICE aims to be realistic demonstration that transverse cooling can be achieved. It will contain three liquid hydrogen absorbers housed in thin aluminium vessels and RF acceleration. The incoming muon beam can be tuned to various emittances and the outgoing emittance measured. The experiment is primarily an engineering challenge, but could be used to check simulations. However MICE only cools in the transverse direction. Longitudinal cooling is hard to achieve, but a way around this is to use emittance exchange. Alternatively there are designs that achieve simultaneous six dimensional cooling, for instance the RFOFO ring.

The results of MICE could still be important because muon cooling is an iterative process based on non-Gaussian energy loss and scattering distributions. The results will help to provide faith in the performance of a full cooling channel. However present simulations of energy loss and multiple scattering are based on simplified derivations dating back many years. Any lack of accuracy will be multiplied up many times in a full cooling channel; what is needed is a first principles derivation of the cross section for muons in liquid hydrogen.

Chapter 3

The theory of charged particles in matter

The simulation of muon cooling is important, and there is some doubt whether traditional approaches model the energy loss and scattering of muons in liquid hydrogen to a sufficient accuracy. This chapter presents a rigorous derivation from first principles of the double differential cross section (in energy loss and transverse momentum transfer) for muons in liquid hydrogen, developed by Allison. This approach emphasises that collisions can cause both energy loss and scattering, and this leads to a correlation between the two that has not been considered elsewhere. A method of evaluating distributions using this new cross section is then discussed, focusing on the implementation of a probability folding technique over a traditional Monte-Carlo, and an analysis of any potential systematic error is carried out. Last, the extension of the technique to other potential cooling materials is considered and some of the traditional shortcomings are re-evaluated in light of this derivation.

3.1 The double differential cross section

3.1.1 Maxwell's equations in (k, ω) space

Maxwell's equations for a general charge density ρ and current density $\mathbf{J}$ are,

$$\begin{aligned} \mathrm{curl}(\mathbf{E}) &= -\frac{\partial \mathbf{B}}{\partial t}, & (3.1)\\ \mathrm{curl}(\mathbf{H}) &= \mathbf{J} + \frac{\partial \mathbf{D}}{\partial t}, & (3.2)\\ \mathrm{div}(\mathbf{B}) &= 0, & (3.3)\\ \mathrm{div}(\mathbf{D}) &= \rho. & (3.4) \end{aligned}$$

These can be rewritten using potentials $\mathbf{A}$ and $\boldsymbol{\phi}$. For a charge q moving in a vacuum at velocity $\boldsymbol{\beta}c$ and passing the origin $r = 0$ at time $t = 0$, $\rho = q\boldsymbol{\delta}^3(\mathbf{r} - \boldsymbol{\beta}ct)$ and $\mathbf{J} = \boldsymbol{\beta}c\rho$.

$$\begin{aligned} \mathbf{E} &= -\frac{\partial \mathbf{A}}{\partial t} - \mathrm{grad}(\boldsymbol{\phi}), & (3.5)\\ \nabla^2\mathbf{A} + \epsilon_0\mu_0\frac{\partial^2 \mathbf{A}}{\partial t^2} &= \mu_0\mathbf{J}, & (3.6) \end{aligned}$$

$$\mathbf{B} = \mathrm{Curl}(\mathbf{A}), \tag{3.7}$$

$$-\nabla^2\boldsymbol{\phi} + \epsilon_0\mu_0\frac{\partial^2\boldsymbol{\phi}}{\partial t^2} = \frac{\rho}{\epsilon_0}, \tag{3.8}$$

where the definition of $\mathbf{A}$ is made by choosing the Lorentz gauge,

$$\mathrm{div}(\mathbf{A}) + \epsilon_0\mu_0\frac{\partial\boldsymbol{\phi}}{\partial t} = 0. \tag{3.9}$$

The electric and magnetic fields are distinguishable by measurement. The $\mathbf{D}$ and $\mathbf{H}$ fields are related through the dielectric polarisation and magnetism. These are functions of the dielectric permittivity and magnetic permeability of the medium, which in turn are functions of frequency. It is not possible to work with Maxwell's equations in position-time space since the permittivity and permeability are not constant. The Fourier transforms are needed, i.e.

$$\mathbf{E}(\mathbf{r},t) = \frac{1}{\sqrt{2\pi}}\int_{-\infty}^{+\infty}\tilde{\mathbf{E}}(\mathbf{r},\omega)e^{-i\omega t}d\omega.$$

However, in a non uniform medium, or at the atomic level, the relationship between the polarisation and magnetisation is not local in space either and depends on the electric field at other places,

$$\tilde{\mathbf{D}}(\mathbf{k},\omega) = \epsilon(\mathbf{k},\omega)\epsilon_0\tilde{\mathbf{E}}(\mathbf{k},\omega).$$

This enforces a four dimensional Fourier transform to express Maxwell's equations in ($\mathbf{k}$,ω) space. So in general for some field $\mathbf{X}$,

$$\mathbf{X}(\mathbf{r},t) = \frac{1}{(2\pi)^2}\int_{-\infty}^{+\infty}\int_{-\infty}^{+\infty}\int_{-\infty}^{+\infty}\int_{-\infty}^{+\infty}\tilde{\mathbf{X}}(\mathbf{k},\omega)e^{i(\mathbf{k}.\mathbf{r}-\omega t)}d\omega d^3\mathbf{k}.$$

When this transform is applied to Maxwell's equations, all of the differential operators become simple factors: the grad operator brings down a factor $i\mathbf{k}$, and taking curl gives a factor $i\mathbf{k}\times$. So Maxwell's equations (3.5 - 3.8) in ($\mathbf{k}$,ω) space become,

$$\tilde{\mathbf{E}} = i\omega\tilde{\mathbf{A}} - i\mathbf{k}\tilde{\boldsymbol{\phi}}, \tag{3.10}$$

$$\tilde{\mathbf{A}} = \frac{1}{\mathbf{k}^2 - \epsilon\epsilon_0\mu\mu_0\omega^2}\mu\mu_0\tilde{\mathbf{J}}, \tag{3.11}$$

$$\tilde{\mathbf{B}} = i\mathbf{k}\times\tilde{\mathbf{A}}, \tag{3.12}$$

$$\tilde{\boldsymbol{\phi}} = \frac{1}{\mathbf{k}^2 - \epsilon\epsilon_0\mu\mu_0\omega^2}\frac{\tilde{\rho}}{\epsilon\epsilon_0}. \tag{3.13}$$

The definition of $\mathbf{A}$ in the Lorentz gauge transforms into $\mathbf{k}.\tilde{\mathbf{A}} - \epsilon\epsilon_0\mu\mu_0\omega\tilde{\boldsymbol{\phi}} = 0$.

3.1.2 Energy loss of a charged particle

The field responsible for slowing down a charged particle in matter is the longitudinal electric field pulling on the charge, $ze(\mathbf{E}\cdot\boldsymbol{\beta})/\mid\boldsymbol{\beta}\mid$, where the field at time t is evaluated at $\mathbf{r}=\boldsymbol{\beta}ct$ corresponding to the position of the charge. The rate of work is force×velocity and thus the rate of energy change with distance (dE/dx) is,

$$\langle\frac{dE}{dX}\rangle=-\frac{ze}{\beta}\mathbf{E}(\boldsymbol{\beta}ct,t)\cdot\boldsymbol{\beta}.$$

An electromagnetic wave can interact with medium constituents and composite structures (constituent and resonant scattering). The former has a typically small, energy independent cross section, the latter large, and dependent. From the view of muon cooling, the constituents are electrons and nuclei, the composites are atoms and molecules. Here the formalism deals with the collision between muons and one hydrogen molecule.

Following the previous discussion it is possible to calculate the value of the **E** field with Fourier transforms. The transform of the input charge and current density are given by,

$$\begin{aligned}\tilde{\rho}(\mathbf{k},\omega) &= \frac{1}{(2\pi)^2}\int_{-\infty}^{\infty}\int_{-\infty}^{\infty}\int_{-\infty}^{\infty}\int_{-\infty}^{\infty}e\boldsymbol{\delta}^3(\mathbf{r}-\boldsymbol{\beta}ct)e^{-i(\mathbf{k}.\mathbf{r}-\omega t)}d^3\mathbf{r}dt, &(3.14)\\ &= \frac{e}{2\pi}\delta(\omega-\mathbf{k}.\boldsymbol{\beta}c), &(3.15)\\ \tilde{\mathbf{J}}(\mathbf{k},\omega) &= \boldsymbol{\beta}c\frac{e}{2\pi}\delta(\omega-\mathbf{k}.\boldsymbol{\beta}c), &(3.16)\end{aligned}$$

where the relation $\int_{-\infty}^{\infty}e^{i\alpha t}dt=2\pi\delta(\alpha)$ has been used. These densities plugged into Maxwell's equations 3.11 and 3.13 yield a value of the potentials $\tilde{\mathbf{A}}$ and $\tilde{\boldsymbol{\phi}}$,

$$\tilde{\mathbf{A}}=\frac{q}{2\pi}\frac{\mu\mu_0\boldsymbol{\beta}c}{\mathbf{k}^2-\epsilon\epsilon_0\mu\mu_0\omega^2}\mu\mu_0\delta(\omega-\mathbf{k}.\boldsymbol{\beta}c),$$

$$\tilde{\boldsymbol{\phi}}=\frac{q}{2\pi}\frac{1/\epsilon\epsilon_0}{\mathbf{k}^2-\epsilon\epsilon_0\mu\mu_0\omega^2}\delta(\omega-\mathbf{k}.\boldsymbol{\beta}c),$$

and these yield values of the **E** field through equation 3.10, which can then be inverse Fourier transformed back to give the required result:

$$\mathbf{E}(\boldsymbol{\beta}ct,t)=\frac{1}{(2\pi)^2}\int_{-\infty}^{\infty}\int_{-\infty}^{\infty}\int_{-\infty}^{\infty}\int_{-\infty}^{\infty}[i\omega\tilde{\mathbf{A}}-i\mathbf{k}\tilde{\boldsymbol{\phi}}]e^{i(\mathbf{k}.\boldsymbol{\beta}ct-\omega t)}d^3\mathbf{k}d\omega.$$

This implies that energy is lost steadily, but this is not the case. The frequency integral should be reinterpreted as the probability of losing an energy $\hbar\omega$:

$$\langle\frac{dE}{dX}\rangle=\int....d\omega=-\int N\frac{d\sigma}{d\omega}\hbar\omega d\omega, \qquad (3.17)$$

which introduces the idea of a differential cross section. More fully the expression for energy loss can be written as,

$$\langle\frac{dE}{dX}\rangle = -\frac{q^2}{\beta^2}\frac{i}{(2\pi)^3}\int_{-\infty}^{\infty}\int_{-\infty}^{\infty}\int_{-\infty}^{\infty}\int_{-\infty}^{\infty}[\frac{\omega\mu\mu_0}{k^2}\frac{\beta^2ck^2-\omega\mathbf{k}.\boldsymbol{\beta}}{k^2-\epsilon\epsilon_0\mu\mu_0\omega^2}-\frac{\mathbf{k}.\boldsymbol{\beta}}{\epsilon\epsilon_0k^2}]\delta(\omega-\mathbf{k}.\boldsymbol{\beta}c)e^{i(\mathbf{k}.\boldsymbol{\beta}ct-\omega t)}d^3kd\omega \tag{3.18}$$

The imaginary part of the equation will be removed by combining positive and negative ω shortly since energy loss must be a real number. First though, note that for non-magnetic media μ=1 and to make any predictions the value of $\epsilon(k,\omega) = \epsilon_1 + i\epsilon_2$ is needed over the physical region. There are two regions where the value is important:

1. The resonance region at low k.

2. The electron constituent scattering region at or near the free electron line of figure 3.1.

These regions are defined by considering the interactions of a charged particle in a medium. For interactions with the atom there will be a spread of momenta for a given energy loss, so the resonance region will be broad in (Pl,Pt). In collisions with constituent electrons, kinematic considerations imply a tight correlation between the energy loss and momentum transfer, and these are represented by a line in (Pl,Pt) space that turns over at the end to represent backward scattering. Cerenkov radiation will occur in regions where ϵ is pure imaginary [52]. A rough sketch of this is shown in figure 3.1.

The real part of ϵ is given in terms of the imaginary part by the Kramers-Kronig relation [53],

$$\epsilon_1(\omega) = 1 + \frac{2}{\pi}\int_0^{\infty}\frac{\omega'\epsilon_2(\omega')}{\omega'^2-\omega^2}.$$

The relationship is a result of causality; the electrical response of a medium must follow its excitation. A knowledge of ϵ_2 thus leads to knowledge of ϵ_1. ϵ_2 describes absorption in a medium. It is thus related to the photo absorption cross section σ_γ as a function of ω,

$$\epsilon_2 = \frac{Nc}{\omega}\sigma_\gamma(\omega),$$

where N is the number density of atoms. However this relationship only applies to real photons. For a virtual field with general value of (k,ω), ϵ_2 depends on the detailed quantum matrix elements of a medium. The generalised oscillator strength density $f(k,\omega)$ relates $\epsilon_2 = \frac{\pi\omega_p^2}{2\omega}f(k,\omega)$ where ω_p is the plasma frequency. Unitarity demands that $\int f(\omega)d\omega = 1$. In first order perturbation theory the generalised oscillator strength density is given in terms

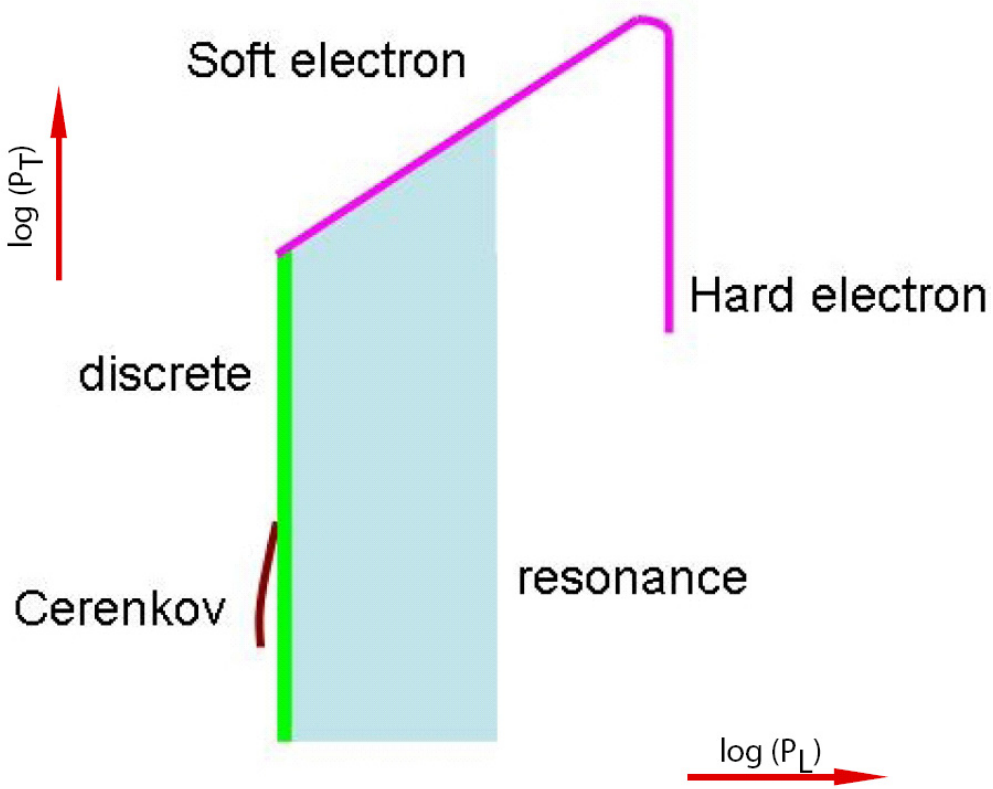

Figure 3.1: A rough sketch of the electron interaction areas in liquid hydrogen.

of transition matrix elements for the bound and unbound energy levels, E_n, of the atom. It can be shown [54] that,

$$\epsilon_2(k,\omega) = \frac{Ne^2\pi}{\epsilon_0} \sum_n |\langle n | \sum_{j=1}^{Z} \frac{e^{(ik.r_j)}}{k} | 0 \rangle|^2 .$$

In the resonance region the Dipole approximation holds, $\tilde{\lambda} \gg r$, or $k \cdot r \ll 1$: the exponential term can be expanded in a multi-pole series. The monopole term vanishes due to orthogonality. The dominant dipole term is independent of k. Higher orders will be neglected in the following analysis, but the effect of omitting them will be considered as a possible systematic error. Hence $f(k,\omega)$ is independent of k in the resonance region and it can be directly related to the photon absorption cross section.

In constituent scattering there will be a large amplitude when $\omega = \frac{\hbar k^2}{2m}$ (from the kinematics of the recoil of an initially stationary electron) so it's possible to approximate $f(k,\omega) \approx \delta(\omega - \frac{\hbar k^2}{2m})$ the amplitude being determined by the sum rule. The two variants of f can be combined using a step-function [54]. The integration over frequencies less than ω may be interpreted as counting the fraction of electrons that are effectively free at frequency ω.

Hence ϵ_2 can be calculated and the value of ϵ_1 is obtained with the Kramers-Kronig relation. In general, input data of photo absorption cross section are given in the low density limit, for which $\epsilon_1 = 1$; in what follows, the preceding value of $\sqrt{\epsilon_1}$ will be dropped from the photo absorption cross section as it is implicit.

Returning to equation 3.18 with the formulas for ϵ in hand, substitute $d^3k = 2\pi k^2 d(\cos(\theta))dk$ and integrate over $\cos(\theta)$ using the delta function $\delta(\omega - k.\beta c) = \delta(\omega - k\beta c\cos(\theta)) = 1/(k\beta c)\delta(\cos(\theta) - \omega/(k\beta c))$, which gives,

$$\langle\frac{dE}{dX}\rangle = -\frac{q^2}{\beta}\frac{i}{(2\pi)^3}\int_{-\infty}^{\infty}\int_{\frac{\omega}{\beta c}}^{\infty}\frac{\omega}{k}[\mu_0\frac{\beta^2c^2k^2-\omega^2}{k^2-\epsilon\epsilon_0\mu_0\omega^2}-\frac{1}{\epsilon\epsilon_0}]dk\,d\omega,$$

with the lower bound of k dependence put in explicitly. Combine positive and negative ω using the relation $\epsilon(-\omega) = \epsilon^*(\omega)$, required if the electric susceptibility function is to be a function of time [53]. The ω integration thus runs from 0 to ∞,

$$\langle\frac{dE}{dX}\rangle = -\frac{q^2}{2\pi^2\beta c^2}\int_0^{\infty}\int_{\frac{\omega}{\beta c}}^{\infty}\frac{\omega}{k}[\mu_0(\beta^2c^2k^2-\omega^2)\mathrm{Im}(\frac{1}{k^2-\epsilon\epsilon_0\mu_0\omega^2})-\mathrm{Im}(\frac{1}{\epsilon\epsilon_0})]dkd\omega.$$

Then putting in the formula for ϵ and integrating over k gives [55],

$$\begin{aligned}\langle\frac{dE}{dX}\rangle &= -\frac{z^2e^2}{4\pi^2\beta^2c^2\epsilon_0}\int_0^{\omega_{max}}d\omega\times[Nc\sigma(\omega)\ln(\frac{1}{\sqrt{(1-\beta^2\epsilon_1)^2+\beta^4\epsilon_2^2}})\\ &\quad+\omega(\beta^2-\frac{\epsilon_1}{\mid\epsilon\mid^2})\phi+\frac{Nc}{\mid\epsilon\mid^2}\sigma(\omega)\ln(\frac{2m\beta^2c^2}{\hbar\omega})+\frac{Nc}{\omega\mid\epsilon\mid^2}\int_0^{\omega}\sigma(\omega')d\omega'],\end{aligned}$$

where $\hbar\omega_{max}$ is the largest energy transfer kinematically allowed in the collision of an incident mass M and stationary electron m;

$$\omega_{max} = \frac{2m\beta^2\gamma^2c^2}{\hbar}(1+\frac{m^2}{M^2}+\frac{2m\gamma}{M})^{-1},$$

where,

$$\phi = \arctan(\frac{\epsilon_2\beta^2}{1-\epsilon_1\beta^2}).$$

The expression above for dE/dX relates directly to the energy-loss cross section $d\sigma/d\omega$, with $\omega = k_L\beta c$:

$$\begin{aligned}\frac{d\sigma}{d\omega} &= -\frac{z^2\alpha}{\pi\beta^2c}[\frac{c}{\omega}\sigma(\omega)ln(\frac{1}{\sqrt{(1-\beta^2\epsilon_1)^2+\beta^4\epsilon_2^2}})+\frac{1}{N}(\beta^2-\frac{\epsilon_1}{\mid\epsilon\mid^2})\phi\\ &\quad+\frac{c}{\omega\mid\epsilon\mid^2}\sigma(\omega)ln(\frac{2m\beta^2c^2}{\hbar\omega})+\frac{c}{\omega^2\mid\epsilon\mid^2}\int_0^{\omega}\sigma(\omega')d\omega'].\end{aligned}\tag{3.19}$$

If N refers to electrons then this is the cross section per electron. It could equally be the cross section per atom (or molecule) with suitably defined σ and N. There are four terms in the

square brackets of equation 3.19 that will be interpreted physically in what follows. The first two terms refer to energy loss through transversely polarised photons; of these, the second describes Cerenkov radiation in the limit of a transparent medium where $\epsilon_2 \to 0$ and the sign of the second term changes from positive to negative at the Cerenkov threshold ($\beta^2 = 1/\epsilon_1$). In the transparent limit the natural logarithm in the first term becomes $\frac{1}{\sqrt{(1-\beta^2\epsilon)^2}} = \gamma^2$ as seen in the Bethe Bloch formula. This term contains the physics of the relativistic rise in $\mathrm{d}E/\mathrm{d}x$, the saturation in the density effect, and the contribution of absorption. Because the second term can go negative it must be interpreted together with the first term. In the presence of absorption the physical distinction between absorbed free photons (second term) and absorbed virtual photons (first term) is not valid. The third term describes energy loss through longitudinally polarised photons. The last term describes Rutherford scattering by constituent electrons that are effectively free.

The Rutherford interpretation can be seen explicitly after manipulation. Noting that the last term is non zero for such energy at which the photo absorption cross section is zero, giving $\mid \epsilon \mid^2 = 1$, it is possible to perform the integration $\int_0^\infty \sigma(\omega\prime)d\omega\prime = \frac{\pi e^2}{2\epsilon_0 mc}$ so that in terms of an energy transfer $E = \hbar\omega$, $\frac{d\sigma}{dE} = \frac{2\pi z^2\alpha^2\hbar^2}{m\beta^2E^2}$. The relativistic constraint for a stationary target given energy, E, and 3-momentum, k, is $(mc + E/c)^2 - \hbar^2k^2 = m^2c^2$. Hence $E = \frac{\hbar^2Q^2}{2m}$ where the 4-momentum transfer squared is $\hbar^2Q^2 = \hbar^2k^2 - \frac{E^2}{c^2}$. Substitution of these terms gives the well known Rutherford cross section for point like charges [56],

$$\frac{d\sigma}{dQ^2} = \frac{4\pi z^2\alpha^2}{\beta^2Q^4}.$$

This is an important validation of the cross section just derived. The high energy reduction to the Rutherford cross section comes out of the manipulation of Maxwell's equations; it has not been inserted by hand. A similar validation is shown from seeing Cerenkov radiation in the non-absorption region where ϵ is imaginary [52].

3.1.3 Constituent scattering by electrons and nuclei

So far no attempt has been made to include the scattering from the nucleus. This is because the energy loss from a scatter is inversely proportional to mass; nuclear scattering gives negligible contribution. For hydrogen the difference is a factor of 0.0005. However nuclear scattering does contribute to large 3-momentum transfer. It is necessary to analyse the

charged particle's interactions in terms of Pl and Pt. Much of this goes over the same ground as the energy loss analysis. The mass difference between the nucleus and the electron removes any interference between the atomic and electron scattering cross section and that of the nuclear and allows them to be combined.

In an elastic collision between a point charge of mass m and velocity β and a stationary charge of mass M, there will be a 4-momentum transfer of $\hbar^2 Q^2$ where $Q^2 = k_L^2 + k_T^2 - \omega^2/c^2$ and a constraint from the projectile mass conservation: $m^2c^2/\hbar^2 = (E^2/c^2 - p^2)/\hbar^2 = (E/\hbar - \omega)^2/c^2 - (p/\hbar - k)^2$ or,

$$k_L = \frac{\omega}{\beta c} + \frac{\hbar Q^2}{2\beta\gamma mc}.$$

Similarly, the target mass constraint gives,

$$\omega = \frac{\hbar Q^2}{2m}.$$

In the relativistic case k_L is thus $\frac{\omega}{\beta c}[1 + m/(\gamma M)]$ and not $\omega/(\beta c)$ as in the non-relativistic treatment of the energy loss. The cross section will be Rutherford with a modifying form factor $F(Q^2)$ being the Fourier transform of the target charge distribution,

$$\frac{d\sigma}{dQ^2} = \frac{4\pi\alpha^2}{\beta^2 Q^4} \times (F(Q^2))^2.$$

The Rutherford cross section must be modified at high and low Q^2 for both electron constituent and nuclear scattering. For collisions with electrons at low Q^2, there is a factor that depends on ω describing the number of electrons that are effectively free (with the remainder taking part in resonant scattering). At high Q^2 electron constituent scattering is point like, but needs a modification for the electron spin (described by Dirac scattering [53]). Modifications to nuclear collisions take account of the finite size of the nucleus at high Q^2 and the shielding of the nucleus by atomic electrons at low Q^2. For a general nucleus the form factor may be derived from the Saxon-Woods description of the nuclear charge density [57]. The Thomas-Fermi model describes the atomic electron shielding [58]. This model is poor for examining atomic structure itself as it does not account for density variations due to the shell structure of atoms, but is a good account of the potential due to all atomic electrons seen by an incident particle in a scattering process. For hydrogen the exact wave-function is known (atomic at least).

3.1.4 Energy loss and scattering

Using Maxwell's equations to find the electromagnetic field acting on a charge there is need to consider energy loss and scattering together. As has been discussed, collisions with constituent electrons tend to give both energy loss and transverse momentum transfer. Going back to equation 3.18 and combining positive and negative frequencies using $\epsilon(-k,-\omega) = \epsilon^*(k,\omega)$ as before gives,

$$\begin{aligned}\langle\frac{dE}{dX}\rangle &= -\frac{e^2}{\beta}\frac{i}{(2\pi)^3}\int_0^\infty\int_{-\infty}^\infty\int_{-\infty}^\infty\int_{-\infty}^\infty \delta(\omega-\mathbf{k}.\boldsymbol{\beta}c)\times \\ &\Big([\frac{\omega\mu\mu_0}{k^2}\frac{\beta^2ck^2-\omega\mathbf{k}.\boldsymbol{\beta}}{k^2-\epsilon\epsilon_0\mu\mu_0\omega^2}-\frac{\mathbf{k}.\boldsymbol{\beta}}{\epsilon\epsilon_0k^2}]e^{-i(\mathbf{k}.\boldsymbol{\beta}c-\omega)t} \\ &-[\frac{\omega\mu\mu_0}{k^2}\frac{\beta^2ck^2-\omega\mathbf{k}.\boldsymbol{\beta}}{k^2-\epsilon^*\epsilon_0\mu\mu_0\omega^2}-\frac{\mathbf{k}.\boldsymbol{\beta}}{\epsilon^*\epsilon_0k^2}]e^{-i(\mathbf{k}.\boldsymbol{\beta}c-\omega)t}\Big)d^3kd\omega.\end{aligned}$$

Now instead of integrating over k to leave an energy loss cross section, integrate over ω using the δ function:

$$\langle\frac{dE}{dX}\rangle = -\frac{2e^2}{(2\pi)^3\beta}\int_{-\infty}^\infty\int_{-\infty}^\infty\int_{-\infty}^\infty\Big[\frac{\mathbf{k}.\boldsymbol{\beta}c\mu\mu_0}{k^2}\mathrm{Im}(\frac{\beta^2ck^2-(\mathbf{k}.\boldsymbol{\beta})^2c}{k^2-\epsilon\mu(\mathbf{k}.\boldsymbol{\beta})^2})-\frac{\mathbf{k}.\boldsymbol{\beta}}{\epsilon_0k^2}\mathrm{Im}(\frac{1}{\epsilon})\Big]d^3k$$

Separating k into its longitudinal and transverse components, and relating the energy loss differential on the left hand side to $-\int\int\int\frac{d^3\sigma}{d^3k}N\omega d^3k$ gives,

$$\begin{aligned}\frac{d^3\sigma}{d^2k_Tdk_L} &= \frac{2e^2}{(2\pi)^3\beta^2cN\hbar k_L}\Big[\frac{k_L\beta\mu}{\epsilon_0k^2}\mathrm{Im}(\frac{\beta^2k^2-\beta^2k_L^2}{k^2-\epsilon\mu\beta^2k_L^2})-\frac{k_L\beta}{\epsilon_0k^2}\mathrm{Im}(\frac{1}{\epsilon})\Big] \\ &= \frac{\alpha}{\pi^2\beta N(k_L^2+k_T^2)}\Big[\beta^2k_T^2\mathrm{Im}(\frac{1}{k^2-\epsilon\beta^2k_L^2})-\mathrm{Im}(\frac{1}{\epsilon})\Big] \\ &= \frac{\alpha\epsilon_2}{\pi^2\beta N(k_L^2+k_T^2)}\Big[\frac{\beta^4k_L^2k_T^2}{(k_L^2(1-\epsilon_1\beta^2)+k_T^2)^2+(\epsilon_2\beta^2k_L^2)^2}-\frac{1}{|\,\epsilon\,|^2}\Big].\end{aligned}$$

Then, writing $d^2k_T = 2\pi k_Tdk_T$ the right hand side is integrated over the azimuthal direction of momentum transfer,

$$\frac{d^2\sigma}{dk_Tdk_L} = \frac{2\alpha\epsilon_2k_T}{\pi\beta N(k_L^2+k_T^2)}\times\Big[\frac{\beta^4k_L^2k_T^2}{(k_L^2(k_T^2+k_L^2(1-\epsilon_1\beta^2))^2+\epsilon_2^2\beta^4k_L^4}-\frac{1}{|\,\epsilon\,|^2}\Big]. \tag{3.20}$$

This is the required double differential cross section for a charge passing through media. To apply it to muons passing through liquid hydrogen just requires the relevant data.

3.2 Input data

The double differential cross section depends on the input particle mainly through its velocity and the square of the magnitude of the charge. Only for the hardest collisions do any of the

other properties like mass, spin, magnetic moment, or structure start to take effect. The medium requires much more detailed information: there is the density, composition, and the photo absorption cross section for each constituent atom or molecule.

The photo absorption cross section is derived partly from theory and partly through experiment. The data is always constrained by sum rules. Both modern data and high quality ground state wave functions exist for molecular hydrogen. Berkowitz [59] gives a detailed discussion of the various calculations and empirical checks made on the H_2 photo absorption cross section. In general, photo absorption cross sections are defined in the limit of zero density. The effect of finite density must be considered. This contributes to five separate effects on both the photo absorption cross section and the charged particle cross section itself [60]:

1. The chemical effect: atomic electrons may be more tightly bound if their atoms are in a chemical compound. In this case photo absorption spectra for the compound should be used instead of the constituent atoms.

2. The medium shift effect: regardless of chemical composition, the outer electrons of a liquid will be affected by the surrounding atoms. Their binding energy will be lowered when compared to those in gaseous atoms and molecules. The scale of this reduction will be a fraction of the plasma energy of the material. This effect will have a role in liquid hydrogen.

3. The medium broadening effect: another effect of neighboring atoms in liquids compared to gasses is that the discrete energy levels are broadened into bands. This mechanism accounts for the formation of conduction bands in metals. Again this will have an energy scale related to a fraction of the plasma energy.

4. The density effect: the effect of polarisation on the energy loss cross section for relativistic moving charges [61]. This does not affect ϵ_2 or photo absorption, but it is already fully taken into account through the influence of ϵ_1 on the energy loss cross section.

5. The Cerenkov effect: a further influence of the polarisation of the medium that has been included in the cross section.

The medium effects can be evaluated by considering the influence they have on observable properties of the material in question. The Thomas-Reiche-Kuhn sum rule [62] acts as a safety net in that it constrains the total photo absorption cross section. From the Kramers-

Kronig relation the dielectric permittivity in the low frequency (optical) region can be written as,

$$\epsilon_1(0) = 1 + \frac{2Nc}{\pi} \int_0^\infty \frac{\sigma_\gamma(\omega)}{\omega^2} d\omega.$$

This is a directly measurable property and is sensitive to the binding energy of the most loosely bound electrons. It is thence possible to lower the binding energy by some small fraction of the plasma energy to get the observed dielectric permittivity (or refractive index) to agree with what is calculated using the above formula. With a suitable discrete shift chosen, it can then be used to give an energy scale by which the discrete lines should be broadened into a Gaussian profile. At the density of liquid hydrogen the plasma energy is 7.6 eV. With a broadening of 0.2eV the photo absorption cross section corresponds to a dielectric permittivity of 1.214, which is 0.022 below the experimental value of 1.236. A discrete shift of -0.8eV is sufficient to achieve agreement between the calculated and observed values. Any uncertainty in both of these methods contributes to a systematic error, which will be evaluated later.

The photo absorption cross section of a homogeneous mixture is thus almost the addition of the constituent parts. The form factor for each nucleus is evaluated separately, neglecting any chemical effects in the outer parts of the atom. This is valid because the net effect of shielding depends on factors of order $\ln(Q_{\mathrm{Max}}/Q_{\mathrm{Min}}) \approx \ln(r_{\mathrm{atom}}/r_{\mathrm{nucleus}})$. A change in the effective atomic radius of 1% would have only about a 0.1% effect on scattering. Figure 3.2 shows the input photo absorption cross section for liquid hydrogen.

3.3 The liquid hydrogen cross section

Using the theory and input data described above it is possible to calculate and draw a three dimensional plot of the cross section, as shown in figure 3.3. The probability varies over ten orders of magnitude. The top most band is the nuclear scattering line, it is clearly separated from the line due to electron scattering. The electron constituent scattering line runs parallel to the nuclear scattering line and joins onto the top of the P_T independent atomic scattering region. To the far right of the plot the cross section turns back on itself representing backward scattering of the muon in the center of mass system.

Collisions with constituent electrons give rise to correlated energy loss and scattering

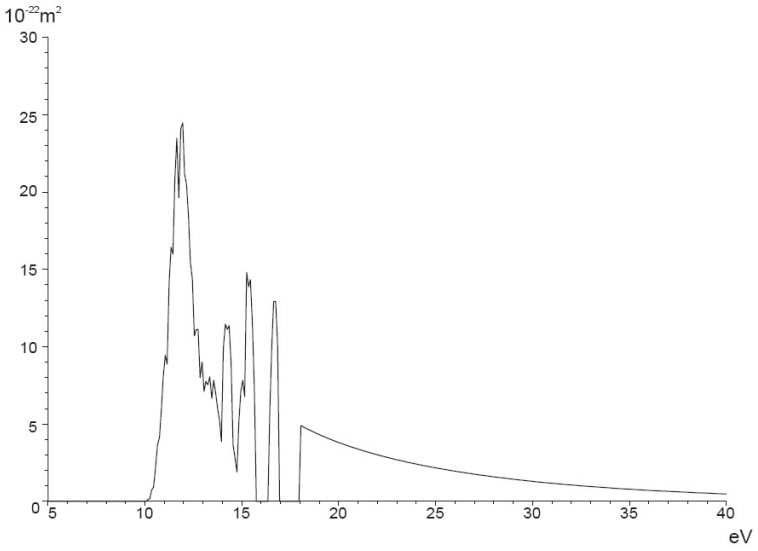

Figure 3.2: The photo absorption spectrum for liquid hydrogen, including the line broadening and discrete energy level shift. The x-axis shows energy in eV, the y-axis cross section in m^2 [59].

transfers (the same is true for nuclear scattering, but the tiny energy loss contribution from nuclear with respect to electron scattering negates the effect). This direct correlation has not been expressed before in traditional approaches to energy loss and scattering, which deal with the two phenomena separately. Whether this will lead to an observable effect when muons pass through liquid hydrogen depends on the relative contribution of electrons to energy loss and scattering.

The total number of collisions at a given momentum can be evaluated by numerical integration. The number falls roughly as $1/\beta^2$ and then plateaus. At high energy the changes are related to the increase in kinematic limits and a hardening of the end spectrum; the number of collisions remains fairly constant. It is also possible to calculate the contributions from various mechanisms, as in table 3.1, which also shows the total number of collisions per metre. The energy loss values can also be calculated directly from the cross section by integration over energy. The 98% root mean square projected transverse momentum transfers are taken from a study of 10 mm of liquid hydrogen using the method outlined in the next section.

The results show that around half of the energy loss and half of the scattering come from collision with constituent electrons. The rest of the energy loss is attributed to resonance scattering (continuum and discrete), whilst nuclear recoil and the Cerenkov effect do not

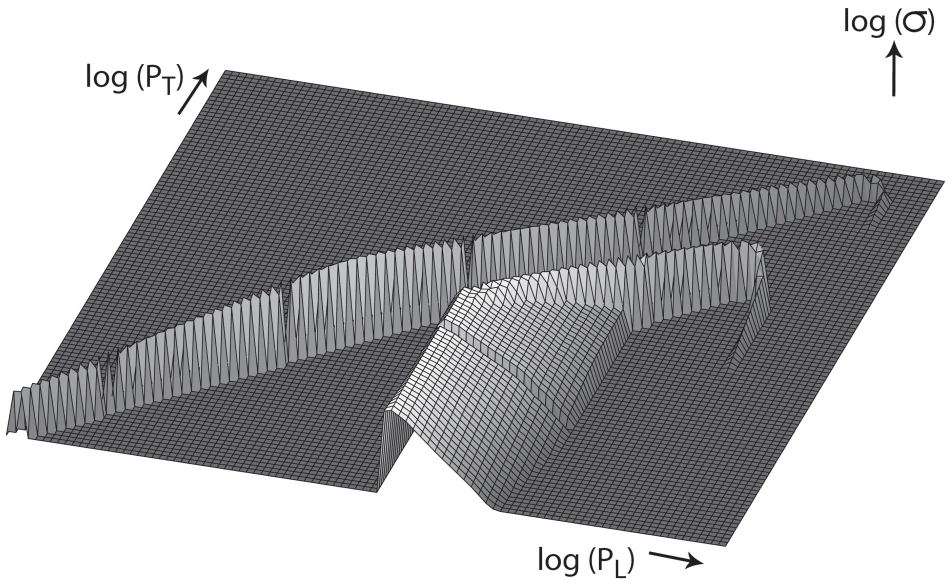

Figure 3.3: The liquid hydrogen energy loss and scattering differential cross section for 2 GeV/c muons. The x-axis is energy loss, the y-axis transverse momentum transfer. This is a log-log-log plot. The range goes from 3×10^{-8}eV to 3×10^{9} eV on the x-axis, and 10 eV/c to 2×10^{9} eV/c on the y-axis.

have a major role. All mechanisms show a $1/\beta^2$ dependence in the non-relativistic region. In the relativistic region the resonance scattering reaches a plateau due to the density effect. Energy loss through electron scattering continues to grow as the kinematic limit increases. Nuclear scattering contributes a similar amount of the transverse momentum transfer to the electron scattering. There is a small, but relevant contribution from resonant scattering. Again, there is a slight increase in electron contribution as the momentum and kinematic limit rises. From this it is possible to conclude that correlations in scattering and energy loss due to collisions with constituent electrons are important at the cross section level for muons in liquid hydrogen. To see if an effect will exist outside of this requires an examination of complete distributions of muons passing through thick absorbers.

3.4 ELMS

To evaluate distributions of energy loss and scattering, an energy loss and multiple scattering program (ELMS) was written to use the cross section derived in the previous sections to generate distributions of muons passing through a given thickness of liquid hydrogen

Muon momentum MeV/c	200	2000	20000
Collisions $10^6 m^{-1}$	0.970	0.893	0.892
Mean dE/dx $MeVcm^2g^{-1}$			
All mechanisms	4.302	4.272	4.896
nuclear recoil	0.002	0.002	0.012
electron recoil	2.180	2.391	2.997
resonance, continuum	1.108	0.971	0.973
resonance, discrete	0.994	0.835	0.834
Cerenkov	0.018	0.071	0.072
98 % RMS P_T MeV/c in 10mm of liquid hydrogen			
All mechanisms	0.3941	0.3573	0.3583
nuclear recoil	0.2675	0.2316	0.2309
electron recoil	0.2652	0.2444	0.2414
resonance, continuum	0.0606	0.0540	0.0538
resonance, discrete	0.0549	0.0489	0.0487

Table 3.1: Mean contribution of different energy loss and scattering mechanisms in liquid hydrogen.

absorber. ELMS first calculates the cross section for a thin slab of liquid hydrogen, then generates a probability distribution of energy loss and transverse momentum transfer by folding multiple collision probabilities (from sub-divided layers) over a number of divisions of the path length. Here, thin means that the cross section is constant across the absorber and scattering gives negligible path change. A thickness of β^2 mm is used because of the cross section dependence on β^2.

The folding is carried out numerically for the longitudinal and two dimensional transverse momentum. Starting with a very thin sample so that the probability of scattering twice in the layer is less than one in 10^6 (since the required final accuracy is better than 1 in 10^3), the layers are folded, doubling the total thickness each time until the required thickness (β^2 mm) is reached. Equation 3.21 shows how the probability of two layers is combined. With the probability of losing a combined energy from layer one and layer two being the sum over all posible combinations of energy one and energy two. This is done with logarithmic bins in ELMS so there is a slight rounding error (around 1%) in choosing which bin a combined energy loss or momentum must go into, while the multiplication becomes a sum of logarithms.

$$P(\epsilon_{12}) = \int P(\epsilon_1)P(\epsilon_2 - \epsilon_1)d\epsilon_1, \tag{3.21}$$

ELMS repeats this for 238 discrete momenta from 5 MeV/c to 50 GeV/c to build up a

Momentum MeV/c	mean	mode	rms	fwhm	1%ile	10%ile	50%ile	90%ile	99%ile
100	4.61	4.99	0.317	0.693	4.07	4.25	4.56	5.04	5.55
200	3.05	2.82	0.456	0.430	2.52	2.65	2.92	3.57	4.86
400	2.80	2.43	0.884	0.467	2.17	2.29	2.55	3.46	6.78
1000	2.90	2.35	2.16	0.450	2.10	2.21	2.47	3.52	10.09
2000	3.02	2.35	4.10	0.457	2.09	2.20	2.46	3.53	12.09
4000	3.15	2.35	6.86	0.458	2.09	2.20	2.46	3.59	13.37
10000	3.31	2.37	13.44	0.470	2.09	2.20	2.46	3.55	14.15
20000	3.54	2.43	38.06	0.475	2.08	2.20	2.46	3.58	13.17
40000	3.73	3.00	71.82	0.544	2.08	2.20	2.46	3.56	12.17

Table 3.2: Statistical analysis of the energy loss (MeV) of muons of various momenta in 10cm of liquid hydrogen.

Momentum MeV/c	mean	mode	rms	fwhm	1%ile	10%ile	50%ile	90%ile	99%ile
100	2.05	1.70	1.14	2.56	0.228	0.734	1.90	3.55	5.46
200	1.54	1.24	1.12	1.90	0.163	0.535	1.38	2.62	4.54
400	1.57	1.25	1.16	1.90	0.168	0.546	1.41	2.70	4.51
1000	1.57	1.22	1.46	1.93	0.164	0.535	1.40	2.69	4.81
2000	1.57	1.23	1.10	1.92	0.164	0.533	1.39	2.72	5.03
4000	1.60	1.24	1.80	1.89	0.165	0.535	1.40	2.71	5.21
10000	1.60	1.23	1.62	1.87	0.167	0.536	1.40	2.72	5.34
20000	1.61	1.23	1.49	1.88	0.166	0.539	1.40	2.75	5.49
40000	1.60	1.22	1.64	1.90	0.168	0.532	1.40	2.72	5.31

Table 3.3: Statistical analysis of the transverse momentum transfer (MeV/c) of muons of various momenta in 10cm of liquid hydrogen.

range of probability distributions. Folding was chosen ahead of a Monte Carlo database of energy and momentum transfer pairs, because the latter is statistically unsafe due to the cross section's high dependence on Q^2 over a range of ten orders of magnitude coupled to the large cumulative distance covered by, for instance, 10^5 muons crossing 10cm of liquid hydrogen.

To track muons through a general thickness of abosrber is then just a matter of sampling from the relevant probability distribution to get an energy loss and transverse momentum transfer pair, with interpolation to compensate for momentum differences and truncated steps at the edge of the absorber if necessary. Examples of distributions generated by native ELMS are shown in figures 3.4 and 3.5. Tables 3.2 and 3.3 show a selection of statistical moments for a range of different muon momenta.

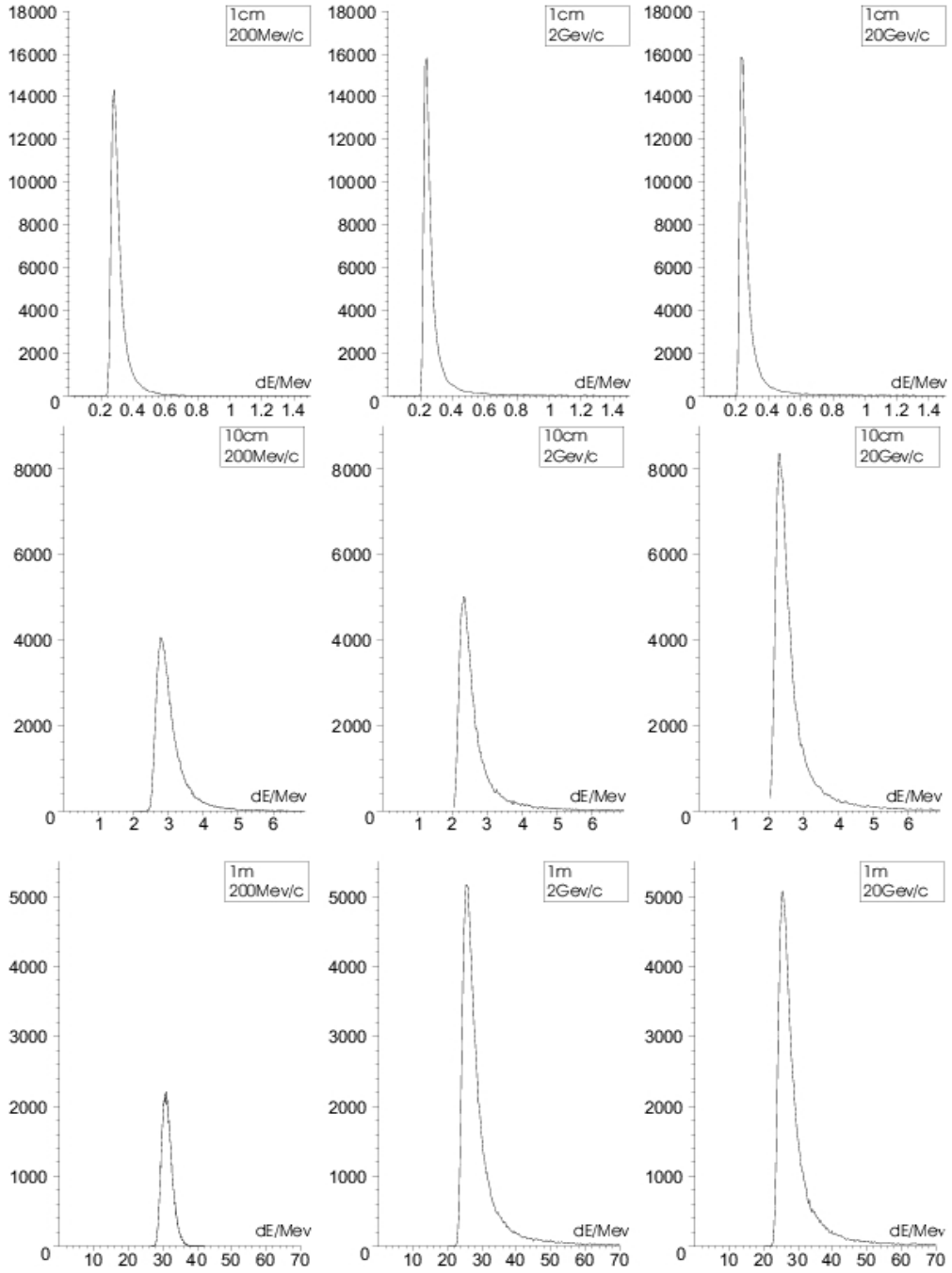

Figure 3.4: Distributions of energy loss for 10^5 muons passing through 1cm, 10cm, and 1m of liquid hydrogen of incident momenta of 200 MeV/c, 2 GeV/c, and 20 GeV/c.

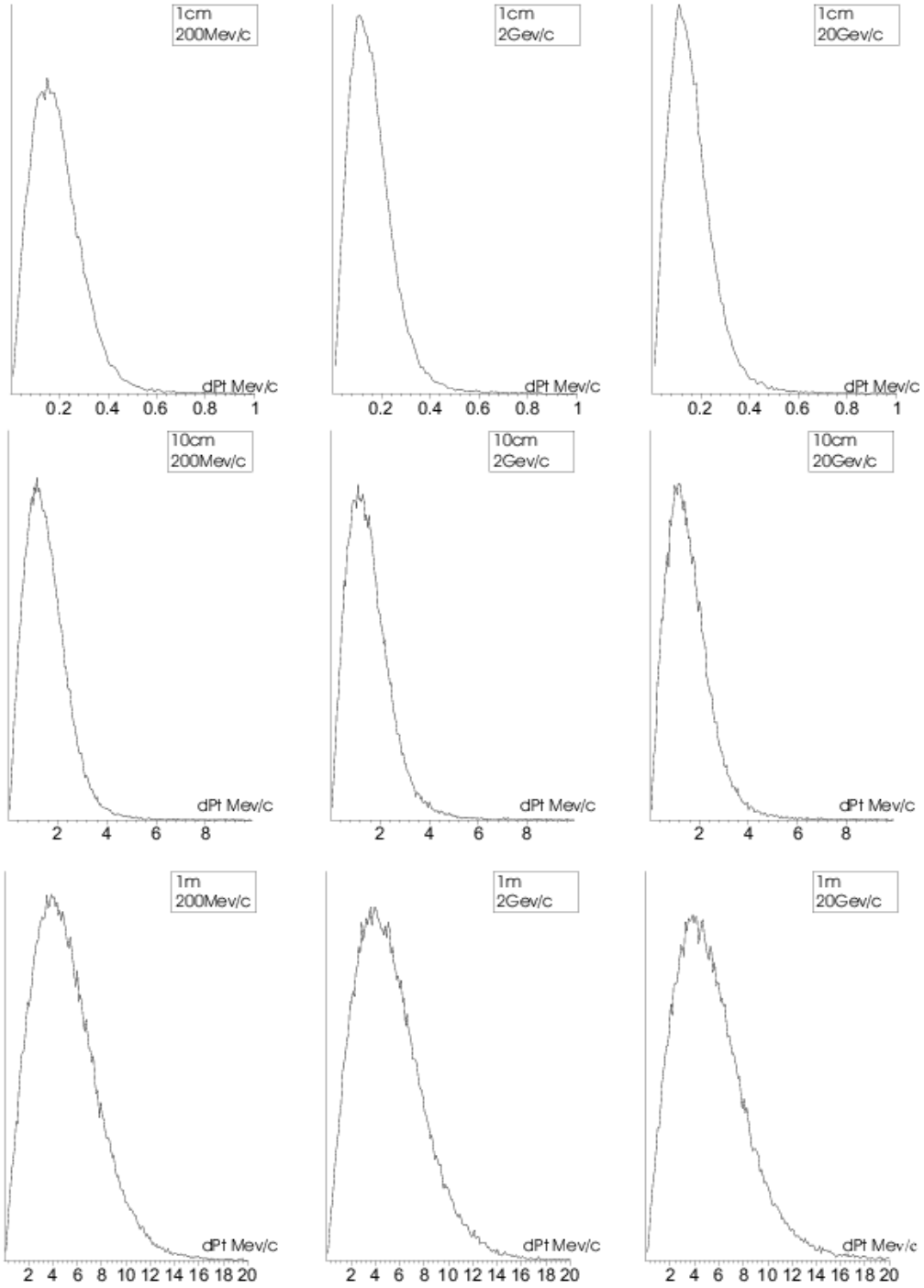

Figure 3.5: Distributions of the magnitude of transverse momentum for 10^5 muons passing through 1cm, 10cm, and 1m of liquid hydrogen of incident momenta of 200 MeV/c, 2 GeV/c, and 20 GeV/c.

Momentum	Thickness			
MeV/c	1mm	10mm	100mm	1m
100	0.40	0.37	0.28	
200	0.43	0.48	0.43	0.48
400	0.38	0.44	0.38	0.42
1000	0.33	0.41	0.41	0.44
2000	0.33	0.35	0.36	0.34
4000	0.31	0.35	0.35	0.41
10000	0.25	0.29	0.31	0.32
20000	0.29	0.25	0.25	0.28
40000	0.25	0.22	0.23	0.25

Table 3.4: The correlation coefficient C as described in equation 3.22 between energy loss and momentum transfer for muons of various momenta passing through different thicknesses of liquid hydrogen.

3.5 Correlations in energy loss and scattering

3.5.1 First order correlations

The energy loss and scattering differential cross section contains a class of collisions in which large energy loss is combined with significant scattering. These are the hard collisions with constituent electrons. Random fluctuations in the number of such collisions will generate correlations in the energy loss and scattering of a sample of mono-energetic muons passing through an absorber, even if its thickness is very small.

From distributions of energy loss and scattering it is possible to evaluate the effect of the cross section correlation, which are significant for liquid hydrogen at the sub-mm level, over a range of thicknesses. This correlation, C, is characterised by equation 3.22 where $\langle E \rangle$ represents the root mean square energy loss, $\bar{E}$ represents the mean energy loss, etc. See table 3.4, though notice that by its nature this measure of correlation will be affected by both first and second order correlation effects.

$$C = \frac{\mathrm{d}\langle Pt \rangle}{\mathrm{d}\langle E \rangle} \frac{\bar{E}}{\bar{P}t} \tag{3.22}$$

3.5.2 Second order correlations

In a thick absorber, a muon that loses greater than average energy early on necessarily has a larger cross section for increased scattering, and a highly scattered muon will traverse a longer path length and may lose more energy. Hence a simulation program that treats energy loss and scattering separately will still see a second order correlation in the energy loss and scattering of a distribution of muons, e.g. in ICOOL. If the first order effect in the ELMS cross section is important in a realistic scenario then it would be expected that the ELMS distribution exhibits more correlation. Figure 3.6 shows the results of plotting the ten energy loss deciles (first ten percent, second ten percent, etc) against the mean Pt of each decile for 10^5 muons passing through a simple 10cm slab of liquid hydrogen, with no containment vessel or fields using both ELMS and ICOOL.

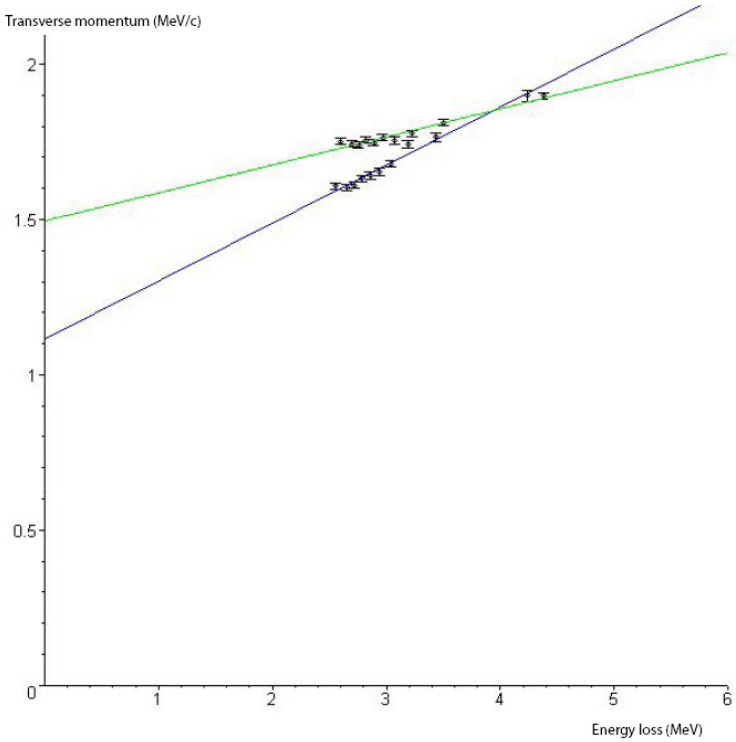

Figure 3.6: Correlations in energy loss and scattering: the ten energy loss deciles plotted against the mean Pt for each decile for 10^5 muons passing through a 10cm block of liquid hydrogen. The black line is for an ELMS simulation, while the green line is for an ICOOL simulation.

The ELMS simulation shows a significantly larger correlation than ICOOL, and the effect of this in full muon cooling simulations will be examined in chapter 4. Qualitatively though, a correlation suggests that those muons in a bunch that scatter more than the average muon

will have also lost more energy and will find themselves towards the back of the bunch. Hence such highly scattered muons will receive more re-acceleration in the RF fields, negating the effect of the high scattering. In other words, the first order correlations may make it easier to cool muons.

3.6 Systematic effects

The following systematic effects affect the ELMS predictions; they are summarised quantitatively in tables 3.5 and 3.6:

1. Higher mulitpole excitation: the cross section was derived under the dipole approximation. Sensitivity to higher multipoles is gauged from the results shown in table 3.5 where the resonance cross section has been enhanced by a factor $\frac{Q.a}{4}$ for the line labelled multipole enhancement. These generally show a few percent difference, though it is important to notice that this enhancement is a large one over the whole resonance region.

2. Density shift and line broadening: these systematics arise from adjusting the gaseous hydrogen photo absorption spectrum so that the calculated refractive index matches that observed in liquid hydrogen. The table shows the effect of halving the applied density shift, and doubling the width of discrete lines.

3. Form Factors and Spin: these are very well known for hydrogen. However the sensitivity to them is important if ELMS is to be extended to other materials and is shown by the lines in table 3.5 for which Mott scattering was used instead of Dirac scattering; the Thomas-Fermi model was used for the atomic electron density instead of the hydrogen atomic wavefunction; and the Saxon-Woods potential used as a measure of the proton shape instead of the Rosenbluth potential [53].

4. Bremsstrahlung: this is the energy loss of a charged particle due to its acceleration in the electric field of nuclei. However at the energy of principal interest to muon cooling the effect is negligible. Bremsstrahlung rises to give a contribution of 1% of the total energy loss at a muon momentum of 50 GeV/c, see table 3.6.

Overall the ELMS predictions should be accurate to one or two percent.

	ELMS values		Changes to ELMS values due to variations					
			Theory	Photoabsorption data		Form factor and spin		
		stat. error	Multi-pole	reduced shift	reduced line width	Mott e-μ	Thomas Fermi	Saxon Woods
Collisions 10^6 m^{-1}	0.970		+.041	-.014	0.000	0.000	+.052	0.000
Energy Loss, MeV								
Tabulated	3.046		+.084	+.003	0.000	0.000	0.000	0.000
Mean	3.045	0.001	+.086	+.006	+.005	-.001	+.005	-.001
Most prob.	2.804	0.004	+.084	+.007	+.009	-.003	+.006	0.000
RMS	0.456		+.005	+.002	+.003	+.004	+.002	-.009
FWHM	0.503	0.003	+.003	+.003	+.016	+.004	+.018	+.014
1%-ile	2.525	0.001	+.087	+.010	+.006	+.003	+.007	+.002
10%-ile	2.654	0.001	+.085	+.006	+.003	0.000	+.004	+.002
50%-ile	2.923	0.001	+.084	+.004	+.006	-.001	+.003	+.001
90%-ile	3.573	0.004	+.076	+.005	-.005	-.010	+.001	-.014
99%-ile	4.868	0.018	+.099	+.009	+.037	+.014	+.024	-.042
Modulus of Transverse Momentum Transfer, MeV/c								
Mean	1.541	0.004	+.008	-.006	+.005	+.005	+.017	-.002
Most prob.	1.201	0.010	-.002	+.001	+.021	-.001	+.033	-.019
RMS	1.120		+.213	+.023	+.053	+.155	+.117	-.066
FWHM	1.891	0.006	-.024	+.001	-.004	-.014	+.010	-.026
1%-ile	0.163	0.003	+.004	+.001	+.001	+.004	+.001	+.005
10%-ile	0.535	0.003	-.001	0.000	+.008	+.001	+.006	+.005
50%-ile	1.384	0.003	+.006	+.004	+.010	+.006	+.017	+.004
90%-ile	2.622	0.006	+.017	-.012	+.004	+.010	+.035	+.017
99%-ile	4.544	0.038	-.063	-.122	-.187	-.134	-.109	-.180
Projected Transverse Momentum Transfer, MeV/c								
RMS	1.361		+.098	-.035	+.026	+.061	+.046	-.042
FWHM	2.718	0.024	+.029	-.010	+.030	+.038	+.022	+.051
90%-ile	1.530	0.004	+.009	+.006	+.014	+.011	+.026	+.002
99%-ile	3.029	0.014	+.030	-.044	+.024	-.007	+.012	-.044
RMS 98% lowest	1.131		-.001	-.006	+.004	-.001	+.011	+.003

Table 3.5: The effect of systematic uncertainties on the energy loss and scattering of 200 MeV/c muons passing through 10cm of liquid hydrogen.

Momentum (GeV/c)	2	3	6	13	26	51
Bremsstrahlung (MeV cm^2g^{-1})	0.001	0.003	0.006	0.012	0.024	0.051

Table 3.6: Bremsstrahlung contribution to total energy loss, compare with the total energy loss in this range, which rises from 4.3 to 4.9 MeV cm^2g^{-1}.

3.7 Extension to other materials

The photo absorption spectra for various low Z elements are available for the gaseous state. There is an obvious difficulty though in that lithium, lithium hydride, carbon, etc are solids: there is no available refractive index with which to adjust the energy levels of the gaseous element so that the calculated refractive index matches the observed. As a comparison, figure 3.7 shows the difference between using atomic and molecular hydrogen, both calculated with ELMS. There is no effect in scattering, but a shift in the position of the energy loss distribution of around 0.2 MeV cm^2 g^{-1}. A similar effect might be predicted for other elements, although the shift in energy levels required to properly move from gaseous to solid phase is greater.

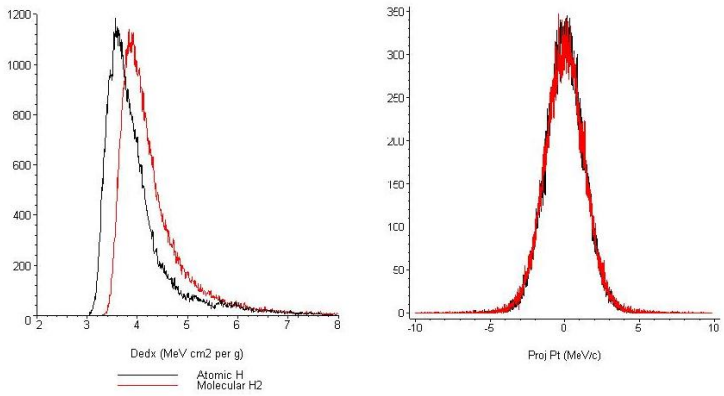

Figure 3.7: Energy loss and Scattering for molecular and atomic hydrogen for 200 MeV/c muons in 10cm of absorber [63].

Figures 3.8 and 3.9 show a comparison of the dE/dx and Pt^2 moments of the cross section for liquid hydrogen, and also lithium and carbon using the gaseous photoabsorbtion spectrum with no shift calculated with ELMS. They are compared to the Particle Data Group values for liquid hydrogen and the solid state of lithium and carbon (graphite). Although these are log plots it is apparent that the energy loss is in better agreement than the scattering. In

the low momentum range the PDG overestimates the variance of Pt^2 compared to ELMS, and the discrepancy increases as Z decreases. This phenomenon is explained by the analysis in the following chapter. Correlations, too, will be more important in lower Z materials, but the coefficient is not analysed here.

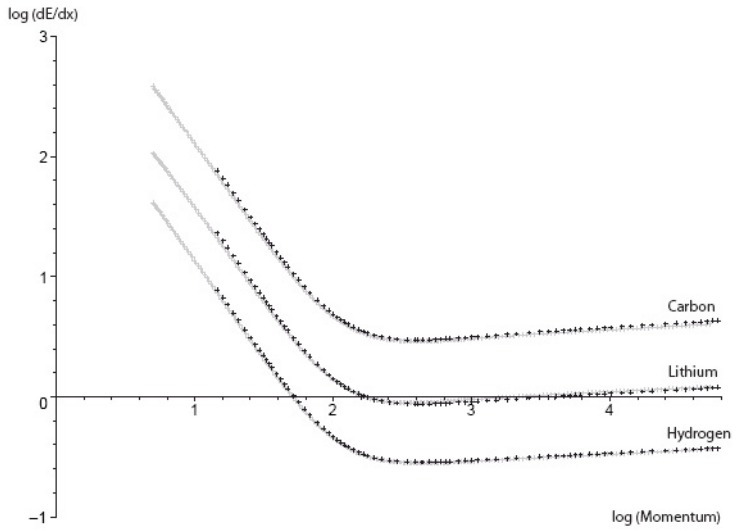

Figure 3.8: log(dE/dx, MeV cm^{-1}) for hydrogen, lithium, and carbon materials using ELMS (grey) compared to the Particle Data Group predictions (black) against log(momentum, MeV/c) [63].

3.8 Traditional shortcomings

Traditional models of energy loss and scattering, namely the Bethe-Bloch formula of ionisation energy loss and Moliere theory of scattering, give fast estimates that were especially useful when today's computing power was not available and when the energy of particles being studied was lower. But they also consist of simplifications that reduce their effectiveness when applied to muon cooling simulations.

3.8.1 Energy loss

The standard Bethe Bloch formula as quoted in the Particle Data Group [1] and used in figures 3.8 and 3.9 is,

$$\langle\frac{dE}{dX}\rangle = -kz^2\frac{Z}{A}\frac{1}{\beta^2}[\frac{1}{2}(\ln(\frac{2m\beta^2\gamma^2c^2}{I^2}E_{kin}^{max}) - \beta^2 - \frac{\delta}{2}]. \tag{3.23}$$

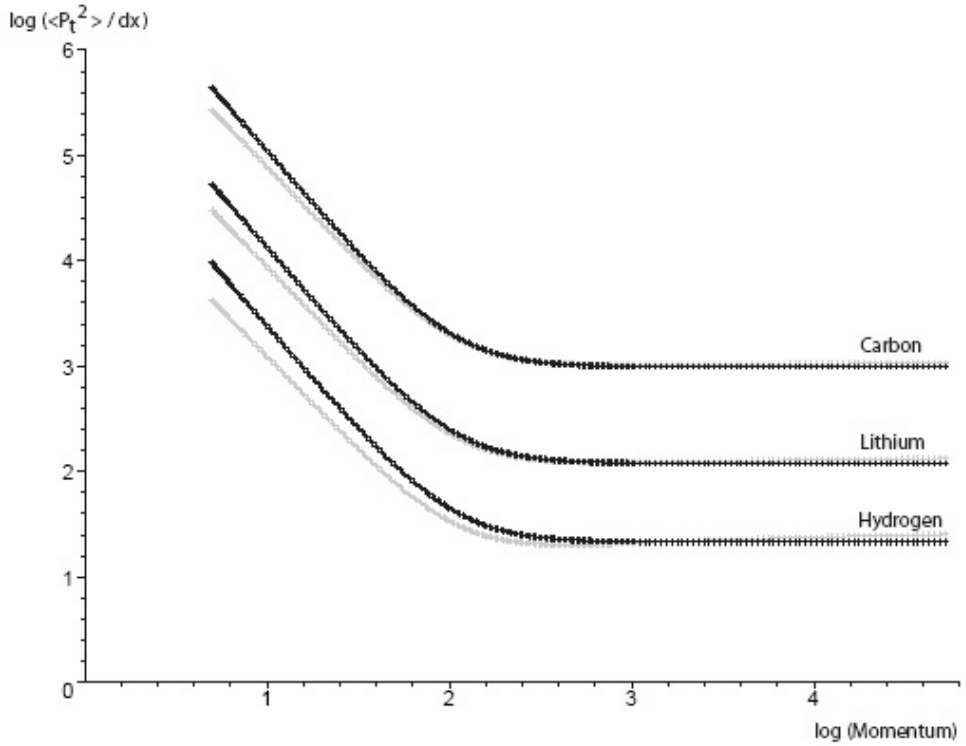

Figure 3.9: $\log(< Pt^2 > /dx$, MeV/c cm^{-1}) for hydrogen, lithium and carbon using ELMS (grey) compared to the Particle Data Group predictions (black) against log(momentum, MeV/c).

There are four assumptions necessary to reduce equation 3.19, which was derived from first principles, to the form of the Bethe-Bloch [52]. These assumptions are not appropriate for modern experiments. In applications that require high accuracy, like the simulation of muon cooling, the calculation should be done as in ELMS:

1. The incident velocity is below the Cerenkov threshold for all ω and $\epsilon_1 \approx 1$.
2. The attenuation length is $\ll$ wavelength, or $\epsilon_2 \ll 1$, and low density $\epsilon_1 = 1$.
3. Incident beam has no spin (Mott scattering).
4. $m \ll M$ and $\gamma \ll \frac{M}{m}$ for incident mass m and target mass M.

3.8.2 Multiple scattering

There is nothing controversial about the Rutherford formula or the form factors required at high and low Q^2. Where difficulty arises is in the large range of Q^2 and subsequent attempts to model a large number of small single scatters by multiple scattering distributions related to diffusion equations. In a simple treamtent the multiple scattering follows a roughly Gaussian distribution [7],

$$P(\theta)d\theta = \frac{2\theta}{<\theta^2>} e^{\frac{-\theta^2}{<\theta^2>}} d\theta.$$

Various more advanced models attempt to describe the multiple scattering of charged particles by atoms [64]. All are mathematically related, for instance Moliere theory [65] starts by assuming small angles and expands in Bessel functions whilst Lewis [66] develops a theory valid for any angle by using Legendre polynomials and then goes over into the small angle limit.

Moliere's theory is popular, partly because it does not assume any special form for the diffrential scattering cross section, however it must reduce to the Rutherford form at large angles. It is usual to see a $Z(Z+1)$ term in the formalism as a modification instead of Z^2 to include scattering off both the nucleus and the electron made by Bethe [67]. It can be seen that this increases the term by a factor of two when considering hydrogen, but has a smaller effect as Z increases. However the modification is only true if the cross section for electron and nuclear scattering is equal. This is not the case at small and large angles. Worse, as Tollestrup [68] notes, the kinematics of the scattering limits the maximum scattering angle of

	ELMS	GEANT auto	GEANT 1mm	GEANT 2mm
Mean dE, MeV	3.046	3.093	3.089	3.090
Median dE	2.888	2.928	2.924	2.926
90%ile dE	3.623	3.715	3.703	3.707
99 %ile dE	5.099	5.315	5.321	5.356
Mean P_t, MeV/c	1.681	1.774	1.585	1.640
RMS98 proj. P_t	1.321	1.405	1.264	1.306

Table 3.7: Comparison of ELMS and GEANT (4.5.2 Patch 02): 10^5 muons with a momentum of 200 MeV/c passing through 10cm of LH2 with $\rho = 0.0708$ g cm^{-3}. GEANT was run for three cases: auto-set step sizes, forced 1mm step size, and forced 2mm step size. The statistical errors on the results are less than 1% for all variables except the 99%ile. Looking at the data, GEANT tends to overestimate dE by a couple of percent and overestimates P_t by around 5%, though predictions vary up to 10% dependant on step size.

muons from electrons to be the mass ratio, m_e/m_μ, which is approximately five milliradians. So using $Z(Z+1)$ across the whole range of angle is not accurate.

3.8.3 Simple comparisons

A simple comparison with GEANT [69], which uses a form of the Bethe-Bloch energy loss formula, and Lewis theory for the scattering distribution is shown in table 3.7. Referring to the table shows that the energy loss is not much affected by changing step size, and agrees with ELMS to a few percent. However multiple scattering shows greater deviation, crucially and perhaps unsuprisingly this deviation fluctuates wildly with changing step size.

It is also straight forward to calculate the range of muons in liquid hydrogen and compare this with what is given by the Particle Data Group, see figure 3.10. The agreement is good, the stopping power of a material is directly related to the energy loss. It is scattering that seems to be less accurate when relying on traditional approaches; thankfully, the MUSCAT experiment has evaluated the scattering of muons in various materials, including two lengths of liquid hydrogen. This experiment, and a direct comparison between the scattering distributions measured and predicted by ELMS and GEANT are the subject of chapter 5.

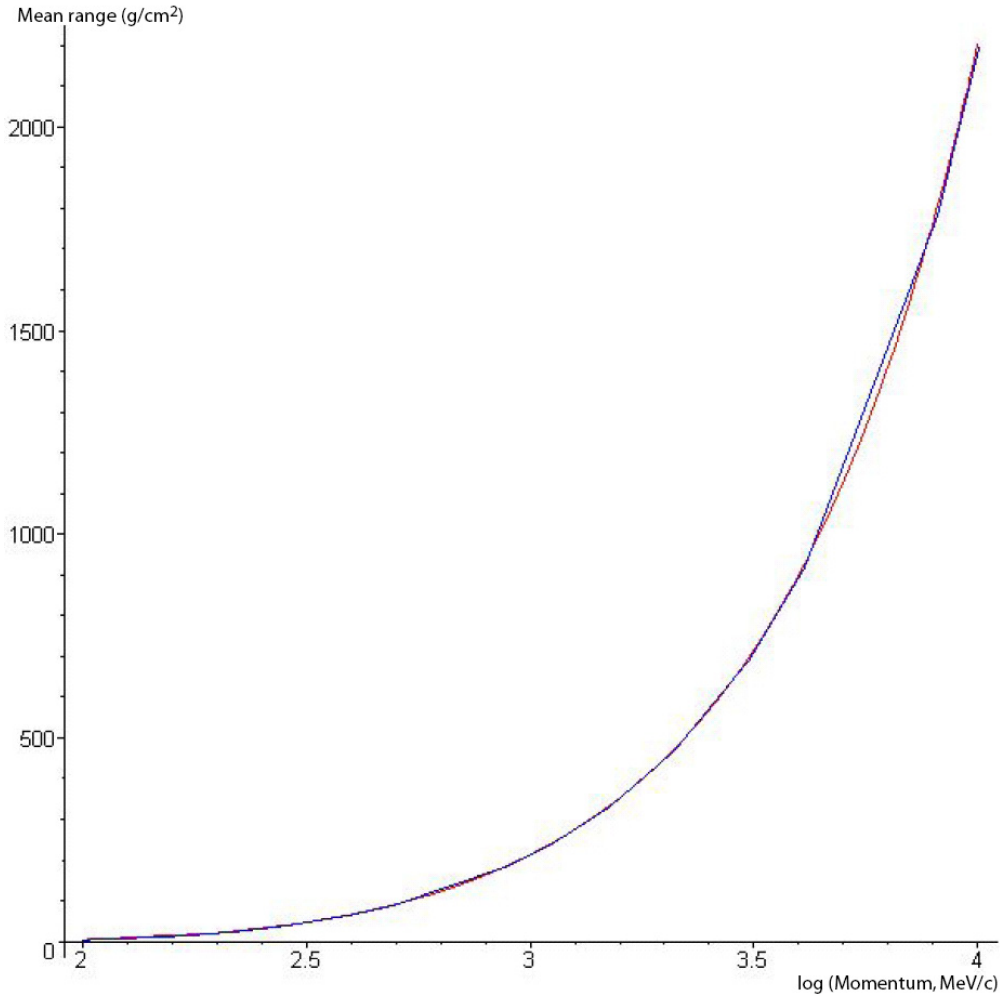

Figure 3.10: The mean range (gcm^{-2}) of 10^5 muons in liquid hydrogen from ELMS (blue) and the Particle Data Group prediction (red) against $\log_{10}$ of the initial longitudinal momentum in MeV/c.

3.9 Summary

A rigorous derivation of the cross section for muons in liquid hydrogen allows the errors on energy loss and scattering to be reduced to one or two percent. The method relies only on Maxwell's equations and well known theory including causality, the dipole approximation, dispersion, oscillator strength sum rules, and point charge scattering at high and low Q^2. The necessary input data is the photoabsorbtion cross section of the scattering material, its density and refractive index, and the incoming particles momentum and mass.

The cross section for muons in liquid hydrogen shows that collisions with constituent electrons gives a correlated contribution to energy loss and scattering that is not considered by traditional calculations. This effect is important at the cross section level: constituent electron scattering provides about half of the energy loss and half of the scattering in liquid hydrogen. To evaluate the effect in thicker samples, a program called ELMS was written. ELMS works in two stages to first generate folded probability distributions for the energy loss and scattering, working on thin slices of material such that the cross section across them is constant. In the second stage it then samples from these distributions to track particles through an absorber of a given thickness. The distributions produced are not only correlated over a large range of thicknesses (with the multiple scattering effects tending to wash out correlation at higher thickness), but when compared with traditional simulation code (which is only correlated for kinematic reasons), ELMS shows a much larger correlation coefficient.

The main systematic error in the ELMS approach is neglecting higher multipole interactions in the high Q^2 resonance region. There is a smaller effect from correcting the photo absorption cross section to account for the non-zero density of real material. The effects of Bremsstrahlung are unimportant below several GeV. There is no reason ELMS cannot be extended to use other materials, the systematic error analysis showed that results were accurate to less than a percent when using the Saxon-Woods nuclear model and the Thomas-Fermi atomic shielding for hydrogen. The study of such materials is less pertinent to muon cooling though, as liquid hydrogen gives the lowest equillibrium emittance and the potential benefits of correlations in scattering and energy loss are less pronounced for higer atomic number.

Last, the inherent trouble caused by simplifications of traditional approaches were re-

iterated. The Bethe Bloch formula can be derived from the rigorous cross section if several unrealistic conditions are satisfied. In these days of high computer power the simplifications made to Moliere theory are unnessecary and dangerous in places, especially for low Z material. For this reason it is unsurprising to see that energy loss predictions agree much better than scattering for hydrogen. However no traditional approach considers them together with a correlated cross section. In order to evaluate the effect of using the ELMS cross section it will be necessary to apply it to realistic cooling scenarios; namely, the set-ups discussed in chapter 2.

Chapter 4

Simulation of muon cooling

The ELMS cross section is incorporated into the energy loss and scattering routines used by a muon cooling simulation program called ICOOL. This enables complex cooling geometries complete with realistic windows and RF cavities to be studied, here the MICE channel and an RFOFO ring. Given that the cross section derived in the previous chapter contained correlated energy loss and scattering contributions from electron collisions, it is also important to be able to test the effect of turning off the correlation. This is achieved by double sampling two independent pairs of energy loss and scattering angle and combining one angle with the other energy loss to give a physical Pl and Pt. A detailed examination of the scattering in a simple slab of liquid hydrogen shows that native ICOOL overestimates scattering compared to ELMS. This does not have a large effect in MICE, but is significant when considering a longer channel, especially the RFOFO which cools down to equilibrium emittance. ELMS in ICOOL predicts a 30% reduction in the equilibrium emittance in the RFOFO when compared to native ICOOL and this is confirmed by an independent test of the change of emittance in a beam near equilibrium in a simple slab with a β_T similar to cooling situations.

4.1 Native ICOOL

ICOOL [66] is a FORTRAN 77 tracking program used to simulate muon cooling in three dimensions. It can follow single particles through materials and magnetic fields, not limited to, but mainly, muons in the range of 1 MeV/c to 1 GeV/c. The physics processes include multiple scattering, energy loss, straggling, delta rays, and decays (the latter are not considered in this analysis). These are dealt with by separate subroutines and are taken from GEANT [70]. The step size is either a fixed user-defined length in any given region, or adaptive dependent on the field and likely energy loss and scattering that will be encountered.

The mean value of the energy loss is computed using the Bethe-Bloch formula including the density effect. Fluctuations in the mean energy loss may be sampled from a Gaussian, Landau, or Vavilov distribution [70]. Multiple scattering is computed either from a number

of Gaussian distributions, or with Rutherford single scattering and the traditional Moliere approach. Moliere is switched to plural Rutherford scatters if the number of scatters in a given step becomes less than twenty (a point where the Moliere approximation becomes invalid).

The incident beam can be generated as a Gaussian in position and momentum, or read from an input file. It is possible to insert a number of beam correlations: muons can be given an angular momentum suitable for starting inside a solenoidal field, the longitudinal phase space can be prepared to fit the beam inside an RF bucket, and the transverse phase space can be given an arbitrary set of Twiss parameters [43]. Though it is important to note that memory requirements limit the number of particles to around 10^5 for complex geometries.

ICOOL is set up so that it can be run in stages, it is thus possible to simulate long channels that cool a beam down to equilibrium emittance. This chapter will compare the original ICOOL energy loss and scattering routines to the effect of bypassing these routines and using the ELMS approach instead.

4.2 ELMS in ICOOL

Given a probability distribution for a muon crossing a thickness of β^2 mm at a given momentum as generated by the ELMS process, it is fairly straight forward to sample from this distribution to give a (correlated) pair of energy loss and transverse momentum transfers. Transplanting this into the existing ICOOL code is achieved by bypassing the existing routines for energy loss and scattering, and calling a new routine that uses ELMS when the material flag is liquid hydrogen. In principle the ELMS bypass could be extended to other cooling materials. Omitting the original routines for liquid hydrogen means that the procedures for dealing with spin and helicity conservation are skipped in this material. However this will not have any effect on the emittance of the beam.

Incorporating ELMS into ICOOL is not completely seamless due to a step size conflict between ICOOL and ELMS: ELMS continues to step through β^2 mm, whilst the step size used in ICOOL can in principle be any size, and this is passed to the ELMS routine for simulation. Conflict between these two values only results in a systematic problem when the step size evaluated by ELMS is less than around 0.1mm. Here ELMS adjusts the energy loss

and multiple scattering relative to the decreased step size. But if this is done too many times it will tend to decrease the width of the scattering and energy loss distribution; qualitatively, a distribution made out of ten 0.1 mm steps with a tenth of the energy loss and scattering of a 1 mm step is narrower than a distribution of just the one 1 mm step. For instance at 200 MeV/c, β is 0.88 mm, so leaving ICOOL on a standard 1 mm step size means that an interpolation from ELMS on a 0.12 mm path must occur each step through the material. It is important to limit these instances and force ICOOL to take a step size of at least a few millimeters in liquid hydrogen, which will be dealt by the ELMS routine in β^2 steps. Figure 4.1 shows an illustration of this. Taking steps of 1 cm and 5 mm were shown to give equivalent results within the limits of statistics for a complex cooling channel. In general 5 mm was used.

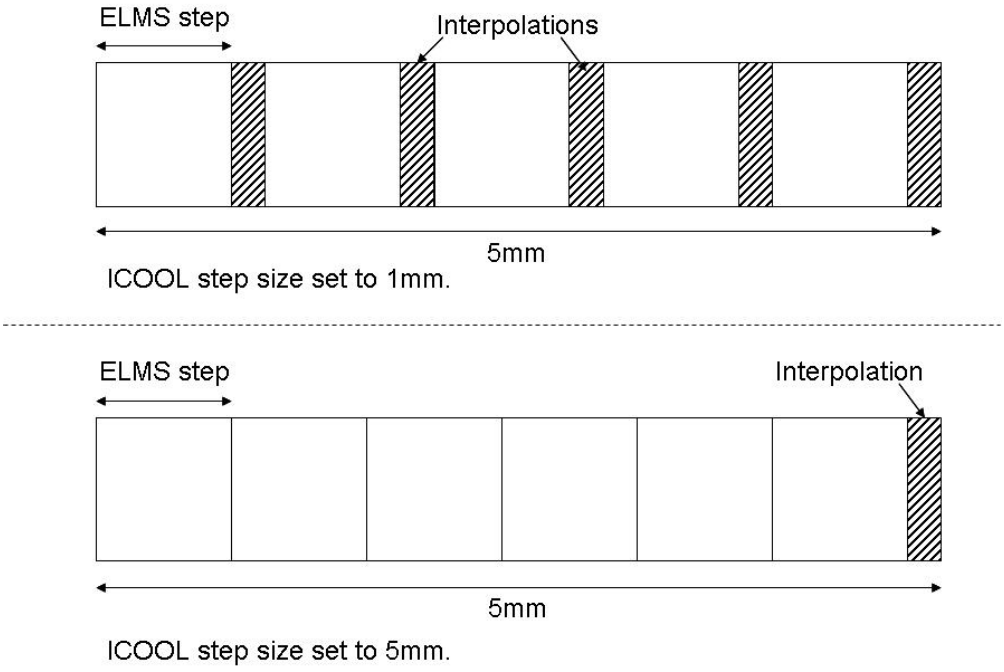

Figure 4.1: Avoiding a conflict between step sizes by setting the ICOOL step in liquid hydrogen to 5 mm: the top picture shows what happens for 200 MeV/c muons going through 5 mm of absorber if the step is set to 1 mm, the bottom what happens if the step is set to 5 mm. In the first case there are five normal steps through the ELMS routine, each accompanied by an interpolation step; in the second there are six normal steps and just one interpolation (an interpolation is practically unavoidable on exiting the absorber material).

4.2.1 The effect of correlations

Whilst the cross section and probability distribution derived from it have first order correlations in them, the effect of these correlations cannot be inferred from comparing ELMS routines in ICOOL with native ICOOL or GEANT. What is needed is a way to treat energy loss and scattering independently in ELMS; in other words, picking two pairs of longitudinal and transverse momentum transfers and combining them.

Care must be taken in the way these two pairs are combined, since to naively combine one Pl with the other Pt could lead to an unphysical situation where the total momentum increases. The correct way to deal with the pairs is to combine them into two pairs of energy losses and scattering angles, then put one energy loss with the other angle and convert these back into a physical (Pl, Pt). Thus the effects of the first order cross section correlation can be assessed in any situation that ICOOL can simulate. Version 2.92 of ICOOL was used for the advanced work and features an option to use ELMS subroutines and this uncorrelation technique as standard.

4.3 Simulating a liquid hydrogen slab

The first comparison between ELMS in ICOOL and native ICOOL was to look at the simple case of a cylindrical block of liquid hydrogen with no windows or fields. This was first done for 10 cm of liquid hydrogen with 10^5 muons at 200 MeV/c. The initial beam was mono-energetic with no transverse momentum. This comparison was done to test the implementation of the correlation switch offered by ELMS in ICOOL. The distributions of energy loss and transverse momentum for these muons are shown in figure 4.2, while figure 4.3 shows a graph of the ten energy loss deciles and the mean transverse momentum transfer for each decile. As expected, native ICOOL and uncorrelated ELMS in ICOOL show a similar shallow slope, but the slope for the correlated ELMS in ICOOL is steeper. The distributions for correlated and uncorrelated ELMS agree, but the scattering distribution for standard ICOOL is higher. Also checked, but not shown, was the agreement between the ELMS engine running inside and outside of ICOOL. From this it was possible to conclude that the implementation in ICOOL worked and that correlation removal was dealt with properly.

Figures 4.4, 4.5, and 4.6 show distributions of $\log(Pt^2)$for decreasing thicknesses of liquid

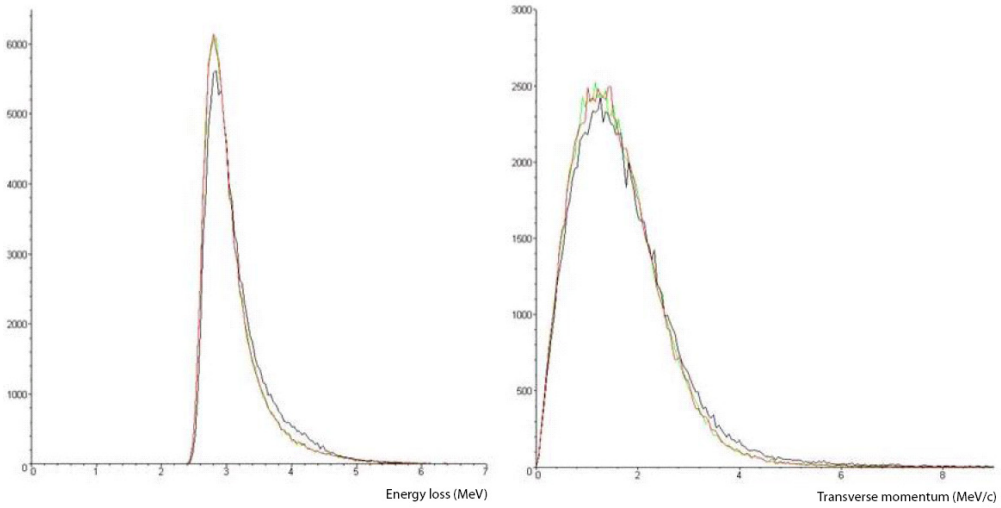

Figure 4.2: Distributions of energy loss and scattering for muons at 200 MeV/c in a 10 cm slab of liquid hydrogen. Standard ICOOL is shown in black, ELMS in ICOOL in red, and uncorrelated ELMS in ICOOL in green.

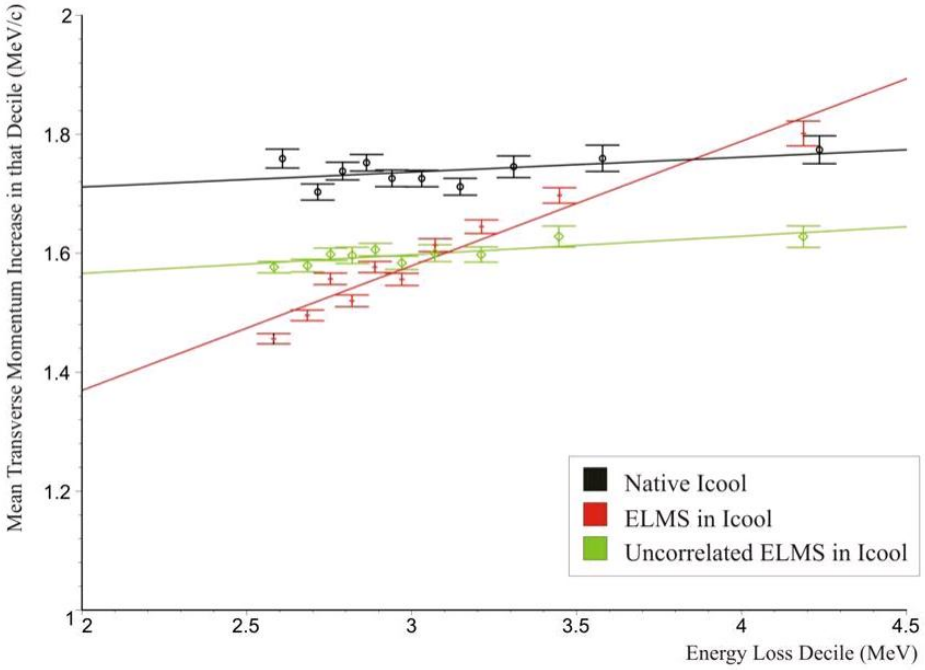

Figure 4.3: Correlations in energy loss and scattering for ELMS in ICOOL versus standard ICOOL and ELMS in ICOOL uncorrelated: a plot of the mean momentum transfer for each energy loss decile, calculated from the distributions in figure 4.2.

hydrogen and the ratio between the results from native ICOOL and ELMS in ICOOL. These runs were done with 10^4 muons and have broadly similar properties: They all show an agreement in the central scattering region, however beyond a certain point the ratio of ICOOL to ELMS in ICOOL begins to rise to a factor of two difference and higher at the largest angles, i.e. native ICOOL predicts higher scattering than ELMS above a given angle, though note that the low number of events in the outer bins means there are large error bars on the ratio of events at high P_t^2. Removing the largest scatters by considering the 98% mean square scattering angle still shows a difference between ELMS in ICOOL and native ICOOL. For 10cm it is 8.66 $\times 10^{-5}$ rad^2 for native ICOOL and 7.51 $\times 10^{-5}$ rad^2 for ELMS in ICOOL. The PDG quoted value is 8.4 $\times 10^{-5}$ rad^2.

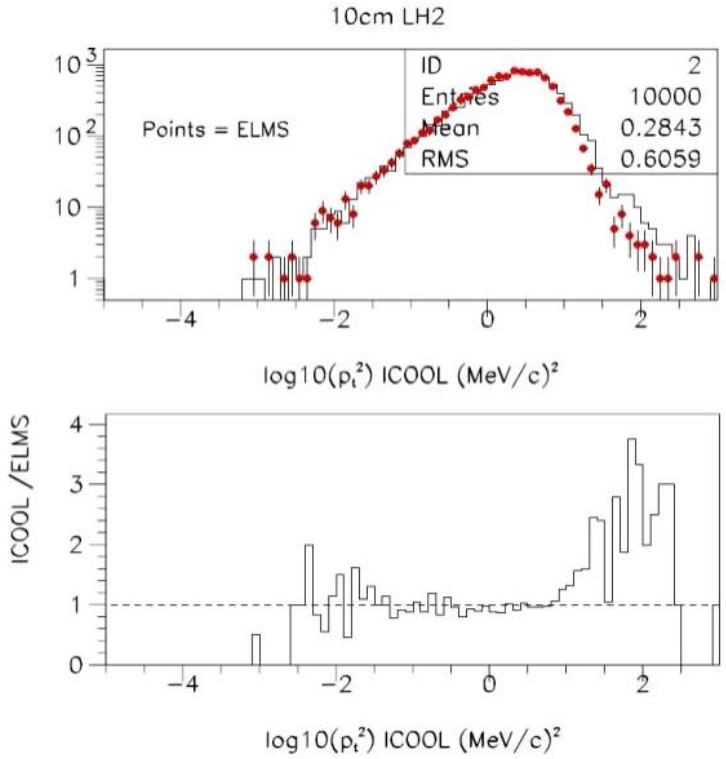

Figure 4.4: Absolute and ratio of $\log(Pt^2)$ in a 10cm slab of liquid hydrogen for native ICOOL and ELMS in ICOOL. In the top picture the points refer to ELMS in ICOOL while the lines and data refer to native ICOOL.

However, as noted by Tollestrup [68], there is a problem in the implementation of Moliere theory in standard calculations. The standard way of including the electron in the Moliere scattering formula is to replace Z^2 with $Z(Z+1)$, but there is a kinematic limit to the scattering of the electron defined by m_e/m_μ. This corresponds to 4.8 mrad. If $Z(Z+1)$ is

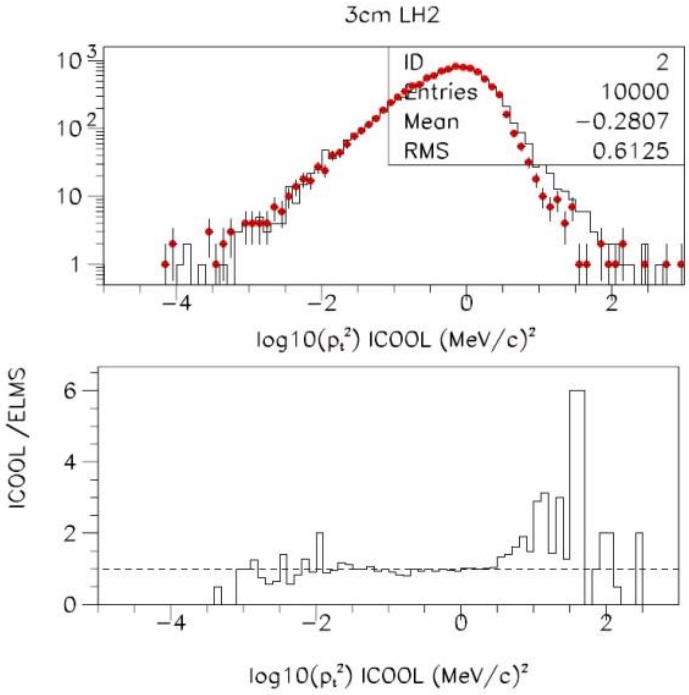

Figure 4.5: Absolute and ratio of $\log(Pt^2)$ in a 3cm slab of liquid hydrogen for native ICOOL and ELMS in ICOOL. In the top picture the points refer to ELMS in ICOOL while the lines and data refer to native ICOOL.

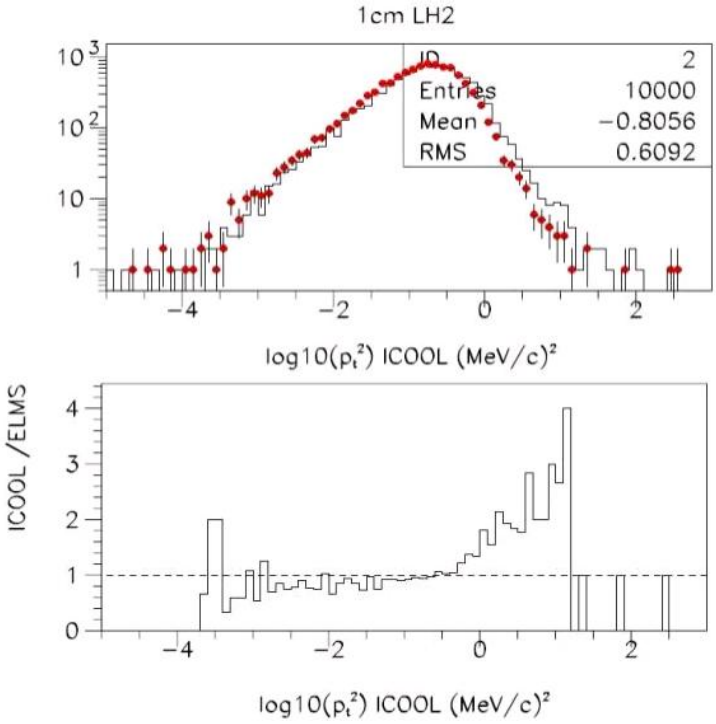

Figure 4.6: Absolute and ratio of $\log(Pt^2)$ in a 1cm slab of liquid hydrogen for native ICOOL and ELMS in ICOOL. In the top picture the points refer to ELMS in ICOOL while the lines and data refer to native ICOOL.

used instead of Z^2 above 4.8 mrad, there is a factor of 2 increase in the scattering probability in liquid hydrogen.

For $\theta_{\max} = 4.8$ mrad, $\mathrm{Pt}_{\max} = (4.8 \times 10^{-3} \times 200)$ MeV/c ≈ 1 MeV/c. Therefore it would be expected that ICOOL/ELMS is greater than 1 for $Pt^2 > 1$ (MeV/c)^2 if not dominated by multiple scatters. This matches the observed behaviour in the thinnest slab, see figure 4.6. It is important to note that the Moliere theory is an approximation and ELMS in ICOOL is calculating scattering from a proper cross section, but exposing the inherent flaw in using Moliere theory naively in scattering simulations is beneficial.

To flesh this out, at large scattering angles both the ELMS cross section and the ICOOL implementation must reduce to Rutherford scattering,

$$P(\theta)d\omega = 4N\frac{Z^2}{A}(\frac{e^2}{\beta Pc})\frac{d\omega}{\theta^4}.$$

Taking any of the distributions, it is possible to integrate the entries and calculate the probability of scattering at an angle of greater than θ^2 to compare with a Rutherford expression, i.e.

$$P(\theta^2 > \theta_0^2) = \int_{\theta_0^2}^{\infty} \frac{dN}{d\theta^2} d\theta^2.$$

Doing this is not strictly correct for more than one point since all of the distribution entries are dependent on those before. Still, a graph of the probability of scattering at an angle greater than θ^2 against θ^2 is interesting since it shows that the probability for ELMS comes back down to the Rutherford line for high angles and that ICOOL does not. This drop begins very close to $\theta^2_{\max}$ (2.3×10^{-5} rad^2), see figure 4.7. E.g. the probability for scattering at an angle greater than 10^{-4} rad^2 in the Rutherford formula is 2.5×10^{-3} and hence a distribution of 10^4 muons should show around 25 scattered above 10^{-4} rad^2. ELMS in ICOOL predicts $20 \pm \sqrt{20}$, Standard ICOOL predicts $70 \pm \sqrt{70}$.

The ELMS model correctly predicts the number of large angle single scatters whereas ICOOL does not. Having found a flaw in the simulation of scattering in ICOOL (and others [71]), the next step was to look at a realistic cooling scenario, to see if this makes a noticeable difference in the expected emittance reduction of various muon cooling set ups. This calculation was done using the ECALC9 software [66]. First the linear MICE channel and then the RFOFO ring down to equilibrium emittance.

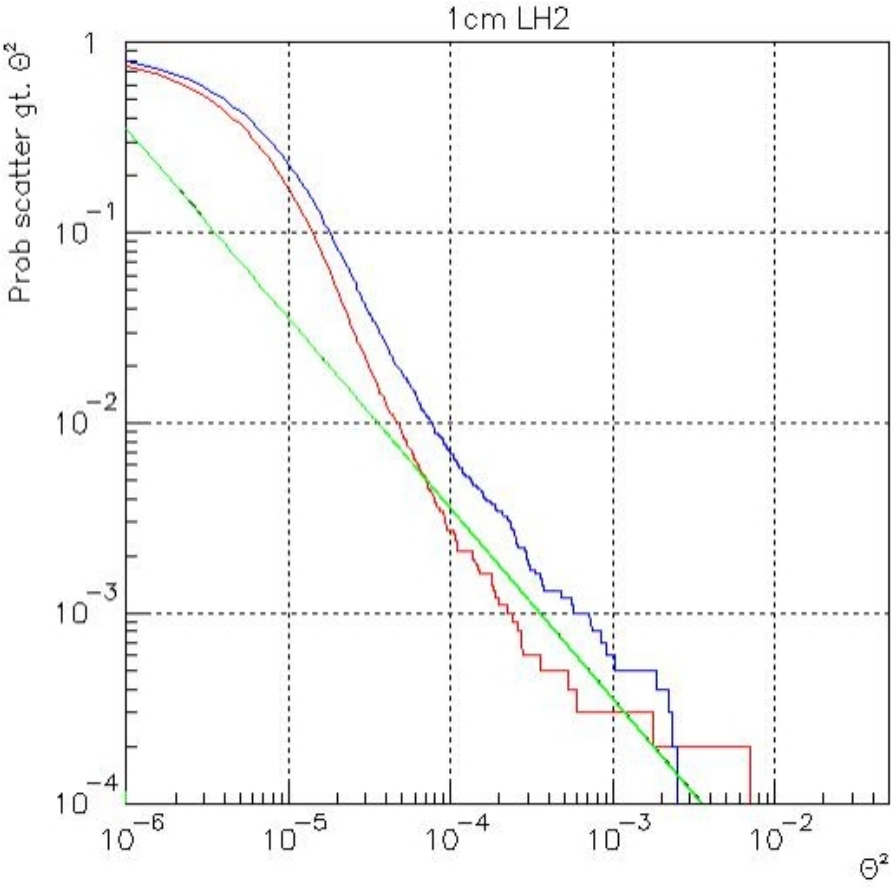

Figure 4.7: The probability of scattering above θ^2 for Rutherford (green), ICOOL (blue), and ELMS (red) for a 1cm slab of LH_2. The electron should be removed from scattering contribution above angles of 2.3 $\times 10^{-5}$ rad^2. At this point the ELMS distribution starts to approach the Rutherford $Z = 1$ line.

4.4 Simulating MICE

An ICOOL simulation of MICE, including the RF cavities and liquid hydrogen windows, was written by Bravar [72]. The channel has an average energy loss of 11 MeV per absorber and runs with an accelerating gradient of 8.3 MV/m over 1.7 m of RF at 201 MHz. The results of running ICOOL with this for 10^4 muons is shown in figure 4.8, which shows the transverse emittance (m rad) against distance for the channel. The total length is around 10 m between the two trackers. The input beam was defined to have an emittance of around 6 mm rad: an initial Pz of 207 MeV/c with $\sigma_{P_x} = \sigma_{P_y} = 20$ MeV/c, $\sigma_x = \sigma_y = 0.033$ m, and $\sigma_{P_z} = \sigma_z = 0$. Ninety nine percent of the initial muon beam survive. A simple measure of cooling performance is the percentage reduction in the beam emittance going in and coming out. For MICE with 10^5 muons, the values of the cooling performance were 12.3 % for standard ICOOL, 13.3 % for ELMS in ICOOL, and 13.4 % for ELMS in ICOOL uncorrelated with a statistical error of 0.1 %.

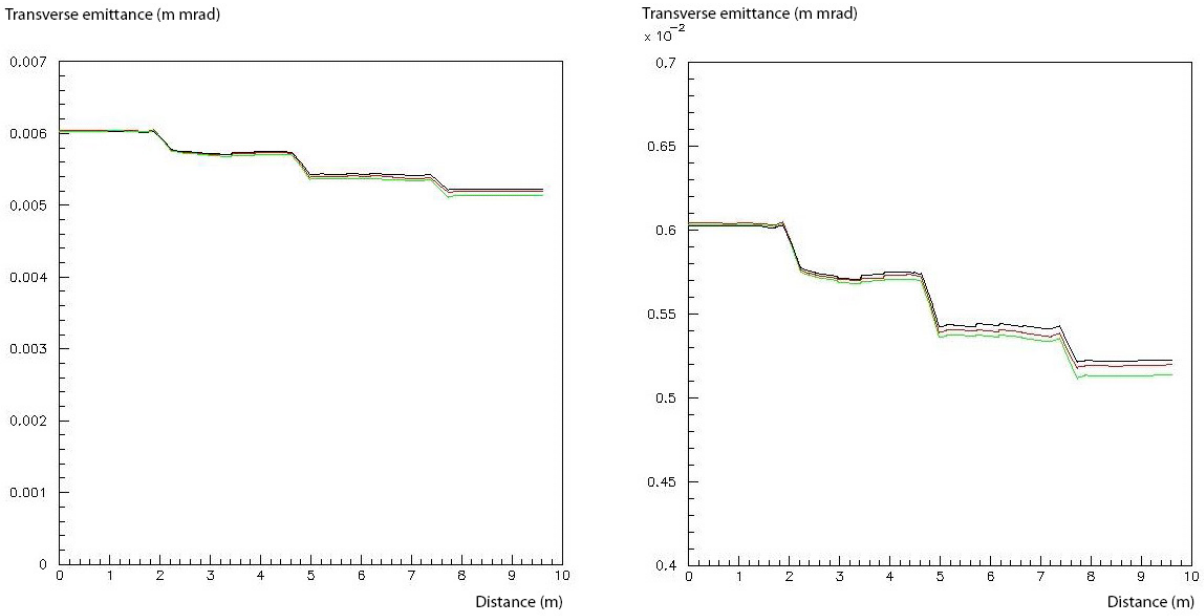

Figure 4.8: Transverse emittance (m rad) against distance (m) for the full MICE simulation. Standard ICOOL is in black, ELMS in ICOOL is in red, and ELMS in ICOOL uncorrelated is in green. The right hand plot is a zoom of the left hand one to show some of the structure in the emittance due to the windows and RF sections.

The emittance graphs are normalised by removing any particles that fail to reach the end. This affects the relative emittance at the start. The three cases are run with the same input beam, but random sampling of energy loss and scattering will cause different ones

to survive. The difference in number here is small. In the zoomed graph of figure 4.8 it is possible to see detail due to the structure of the MICE channel: the down slope is the absorber, with a slight rise in emittance just before and after the absorber being due to the windows; the momentum restoring RF forms the up slope in the emittance, with four steps up for each of the individual sections that make up the RF channel.

These results show that there is a 10% difference between the emittance predicted by ICOOL and the emittance predicted by ELMS in ICOOL in this channel, also that correlations make only a statistical difference in cooling performance for MICE. MICE claims to be able to measure emittance to 1% so this effect should be just visible [73]. This may be hampered by the presence of double absorber windows in the actual experiment, which act as a fail safe to the liquid hydrogen containment. Of course MICE is really more of an engineering problem to show that cooling is feasible in practise. An extension of the MICE channel over a longer distance should cool the beam further and accentuate the differences between ELMS and ICOOL with respect to the achievable emittance for a neutrino factory or muon collider.

4.4.1 Simulating a 100m MICE channel

The principle of setting up a repeating MICE cell to extend the length of a cooling channel simulated in ICOOL to 100m (and beyond) is not difficult in simulation. However there needs to be adjustments made to the beam and accelerating structure in order to make it work: the beam needs to be given an amplitude momentum correlation such that muons that are further out from the centre have more momentum to compensate for them spiralling in the magnetic field, the effect of taking a certain length of time to cross the RF must be taken into account, and the RF must be set up so that the beam is off the peak of the sinusoidal accelerating voltage to give lagging and leading particles respectively more and less of an accelerating boost. Not making these changes make the survival percentage drop from 99 % of muons for MICE down to less than 0.1 %. The following changes were put in by hand in the ICOOL set up.

To run off peak the RF phase was adjusted to 45 degrees. This is set up by ICOOL automatically with respect to a reference particle, which is forced to go through the simulation without experiencing energy loss and scattering. The voltage was also increased by a factor

of $\sqrt{2}$ to compensate for moving off peak. A check is to re-run the MICE channel and see no change in the momentum of the beam as it goes through. By running off peak the cooling performance of the MICE channel (in all cases) increases by 0.5% absolute and more muons survive the channel, as expected.

When particles travel in the magnetic field they will spiral in helical orbits. Because of this the particles at the edge of the beam will have to travel further than those in the middle and hence tend to lag behind. Accounting for the helical orbit of the particles is done by introducing an amplitude-momentum correlation in the beam. Amplitude is defined by $A^2 = \beta_T(\theta_x^2 + \theta_y^2) + (\frac{x^2+y^2}{\beta_T})$, where β_T is 33 cm in the tracker solenoids for MICE and 42 cm in the absorbers but varies along the channel. The correlation strength is then calculated by running 10^5 muons through a 100 m channel and taking the slope of the momentum against amplitude of the initial beam for the ones that survive.

Last, because the E field varies over the length of the accelerating cavities, a particle crossing the cavity will experience a varying field. Therefore the change in energy must take account of this ratio of energy gained in the time varying field to energy gained in a DC field. This is the transit time factor (T). Assuming the waveform is symmetrical around the centre of the gap where,

$$T = \frac{\int_{-L/2}^{L/2} E(0,z)\cos\frac{2\pi z}{\beta\lambda} dz}{\int_{-L/2}^{L/2} E(0,z) dz}.$$

The work done to the beam is defined as,

$$\Delta W = qE_0 TL\cos\phi.$$

The mean loss in one absorber and RF section is 12.3 MeV, which must be replaced by four separate RF cavities, enabling the correct value of E_0, the peak field, to be calculated. With all of this in place, the results of simulating the 100m MICE style channel is shown in figure 4.9.

Predicted cooling performances were 55% for ICOOL, 59% for ELMS in ICOOL, and 58% for ELMS in ICOOL uncorrelated. 90% of the initial beam with the various correlations survive in each case. There is still little effect due to correlations in ELMS. However a 100m linear channel is not cost effective, and the simulations show that 100m doesn't reach equilibrium emittance, though there is some effect due to the windows pushing the equillibrium higher.

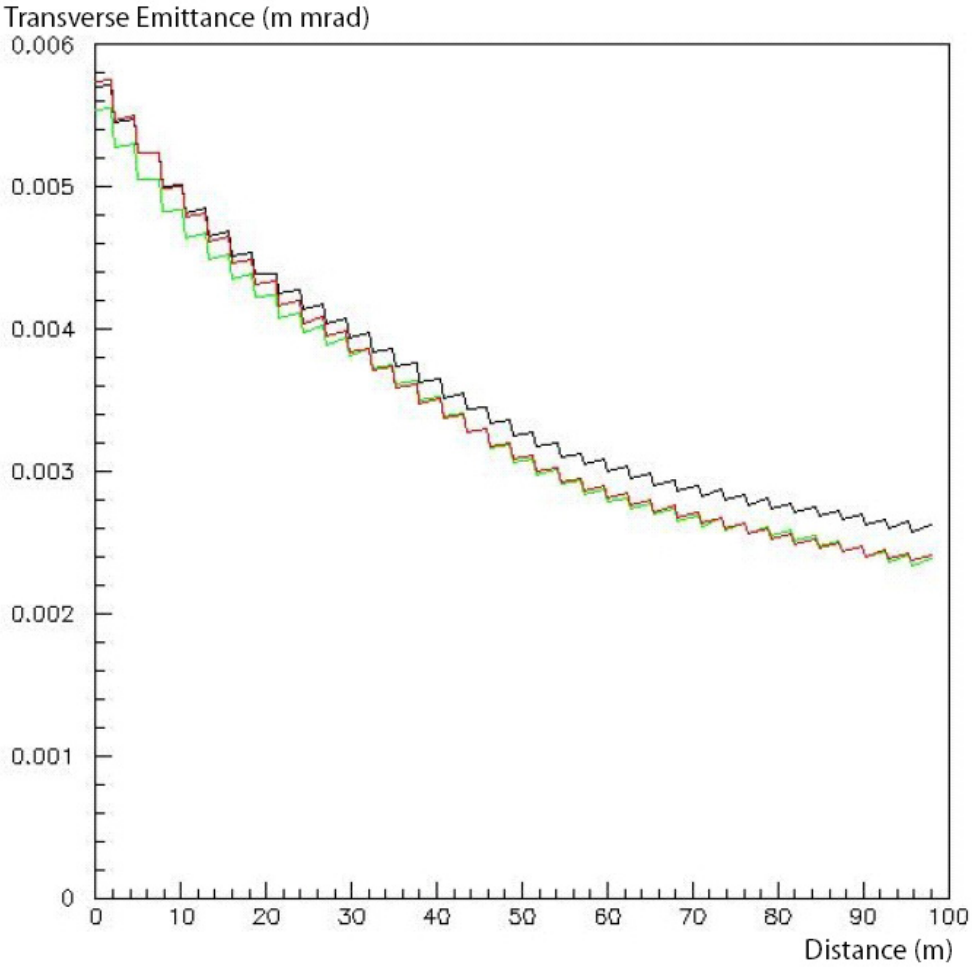

Figure 4.9: Transverse emittance (m rad) against distance (m) for an extended linear MICE channel that repeats the structure over 100m. Again, Standard ICOOL is in black, ELMS in ICOOL is in red, and ELMS in ICOOL uncorrelated is in green. There is now a difference between the predictions by ELMS and ICOOL.

4.5 Simulating the RFOFO ring

As discussed in chapter 2, the RFOFO ring offers a way to achieve simultaneous longitudinal and transverse cooling by using wedge shaped absorbers in a circular ring of absorbers and RF cavities. ICOOL has already been used to model the performance of such a ring using several factors defined to quantify cooling performance [49]: the longitudinal, transverse, and 6D emittance, the merit factor, transmission, and the number of muons in a given phase space acceptance (D-factor). The last term is relevant to a neutrino factory since it represents how many muons can be cooled with respect to the machine's acceptance. The merit factor, $M(z)$, is relevant to a muon collider, as it shows the relative increase in central phase space density. It is defined as,

$$M(z) = \frac{\epsilon_{6N}(initial)}{\epsilon_{6N}(z)} T,$$

where ϵ_{6N} is the normalised 6D emittance and T is the total muon transmission (the number of surviving muons at a given point). This represents both how tightly focused the beam is, and how many muons it contains. Luminosity is affected both by the focussing and the number of muons in the beam.

These performance measures can be applied to the output from ELMS in ICOOL and native ICOOL. First the merit factor and emittances are compared in figure 4.10, and then the muon density in two fixed acceptances is compared in figure 4.11. Here both acceptance volumes have a longitudinal acceptance of 35 mm. Acceptance volume 1 has a transverse acceptance of 15 mm, while acceptance volume 2 has a transverse acceptance of 9.75 mm, which could correspond to the acceptance of a linear accelerator that follows the cooling ring at a neutrino factory.

After a distance of 500 m (roughly 15 turns) the transmission is 51% for ELMS in ICOOL and 49% for standard ICOOL (with muon decays suppressed). The initial drop in transmission is due to a mismatch between the beam and the ring acceptance. The transverse emittance goes flat for both values, indicating it has reached an equilibrium. However there is a 33% reduction in the equilibrium emittance predicted by ELMS in ICOOL (1.74 mm) compared with that of standard ICOOL (2.32 mm). ELMS in ICOOL also shows a 26% reduction in longitudinal emittance (2.44 mm compared to 3.07 mm) and more than a factor of two reduction in the 6D emittance (7.2 mm^3 compared to 16 mm^3). This factor

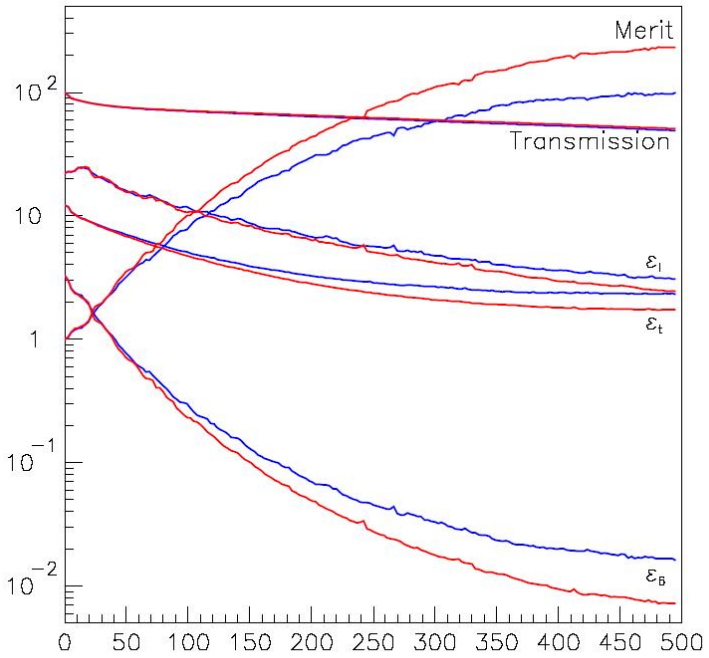

Figure 4.10: Summary plot of the performance of an RFOFO ring against distance in metres. The ELMS in ICOOL results are in red and the standard ICOOL results are in blue. Longitudinal and transverse emittance is measured in mm, 6D emittance is measured in cm^3.

2 improvement is mirrored in the merit factor, which is 230 for ELMS in ICOOL and 100 for standard ICOOL (compare to the feasibility study 2 linear channel value of 15). A doubling of merit is large, but merit is a measure of the central phase space density and is quite sensitive. The number of muons into a phase space acceptance volume is a more realistic comparison for a neutrino factory. Figure 4.11 shows that for the standard ICOOL simulation, the RFOFO ring increases the muon density into the smaller acceptance volume by a factor of almost 10 after 250m (8 turns). The density in the larger acceptance volume rises by a factor of 6. ELMS in ICOOL improves both of these figures, though obviously the improvement decreases as the acceptance volume increases. ELMS in ICOOL predicts that the smaller acceptance volume should contain a 14 fold increase in muon density, while the larger acceptance volume gains 7 times. ELMS in ICOOL predicts a 40% increase in the number of muons in the smaller acceptance volume.

Figure 4.12 shows the effect of removing correlations from ELMS in ICOOL. There is no change between the two, and hence it is fair to conclude that correlations do not affect muon cooling performance, or the equilibrium emittance in liquid hydrogen. Materials of

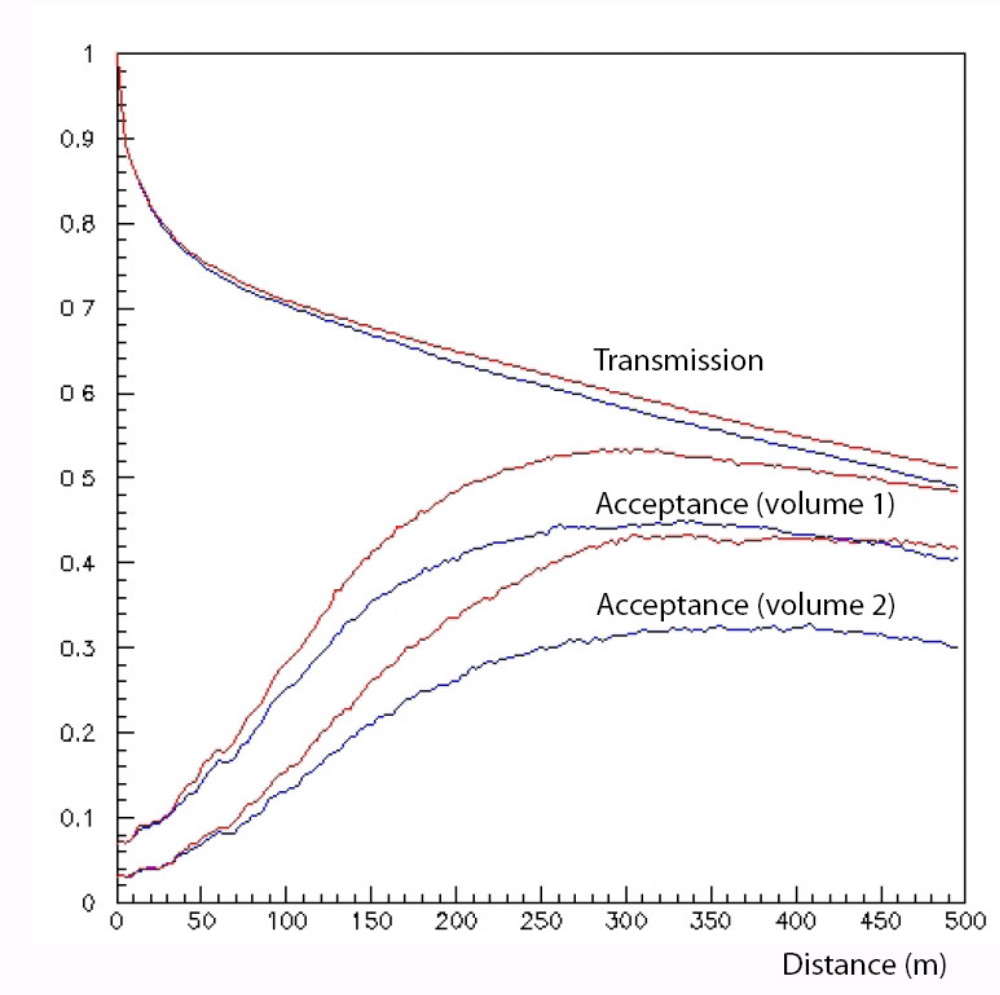

Figure 4.11: Acceptance for an RFOFO ring. The ELMS in ICOOL results are in red and the standard ICOOL results are in blue. Two different acceptance volumes are shown. Both volumes have a longitudinal acceptance of 35 mm. Volume 1 has a transverse acceptance of 15 mm, while volume 2 has a transverse acceptance of 9.75 mm.

higher Z would have even less correlation dependence because the electron scattering would constitute less of the bulk of scattering and energy loss. However observing their existence in empirical data would reinforce the theory behind ELMS, and this is attempted for the MUSCAT data in chapter 5.

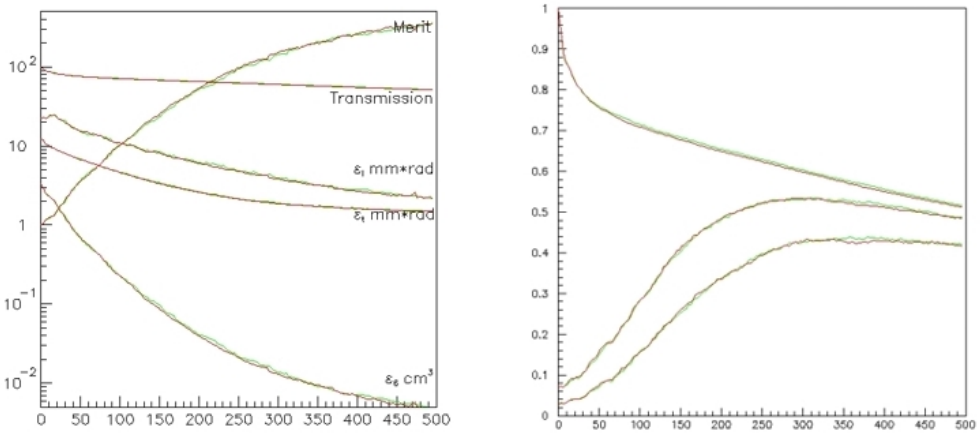

Figure 4.12: The impact of removing ELMS correlations on RFOFO performance. The ELMS in ICOOL results are in red and the uncorrelated ELMS in ICOOL results are in green. Longitudinal and transverse emittance is measured in mm, 6D emittance is measured in cm^3.

Despite correlations having no effect on muon cooling performance, the ELMS approach in itself has shown that predictions based on the traditional treatment of energy loss and multiple scattering underestimate the equilibrium emittance achievable and hence the cooling performance of long cooling channels. The main reason for these changes is that ELMS predicts less scattering than ICOOL, especially out in the tails of the distribution where ICOOL is shown to overestimate single scatters.

4.6 An independent test of the equilibrium emittance

Since the relative increase in merit predicted by ELMS in ICOOL with respect to standard ICOOL is so large it is necessary to investigate further. Instead of running an RFOFO round and round, it is possible to study the equilibrium emittance independently with a simple set up; a slab of liquid hydrogen with a β_T similar to the conditions in the RFOFO enables the determination of the emittance at which crossing the slab does not increase or decrease the emittance, i.e. the minimum, or equilibrium value. This was carried out with 10^5 muons

through 20 cm of liquid hydrogen with β_T of 40 cm.

A formula for the change in emittance is derived from equation 2.10,

$$\frac{d\epsilon_n}{\epsilon_n} = (\epsilon_n - \epsilon_\infty)\frac{dz}{\lambda\epsilon_n}.$$

Where the sign has been changed to plot $\epsilon_{\text{in}} - \epsilon_{\text{out}}$. Using the definition of λ and relativistic relations between E and P ($dp/p = dE/\beta^2 E$), the percentage change in emittance is given by,

$$\frac{\epsilon_{in} - \epsilon_{out}}{\epsilon_{in}} = \frac{dp}{p} \times (1 - \frac{\epsilon_\infty}{\epsilon_{in}}) \times 100\%,$$

where dp/p comes from the mean energy loss in liquid hydrogen at 200 MeV/c, which ELMS calculated (table 3.1) as 4.302 MeV cm^2 g^{-1}. This gives dp/p = 3.45%. See figures 4.13 and 4.14.

The values from fitting are $\epsilon_\infty = 0.160$ cm for native ICOOL and $\epsilon_\infty = 0.118$ cm for native ELMS. The plots contain errors on the value of emittance, but for 10^5 events these are around 0.01 % and are barely visible [74]. The scatter about the best fit line is due to the finite number of digits produced in the analysis software [70]; the 4sf precision of the ratio of $\epsilon_{in} - \epsilon_{out}/\epsilon_{in}$ is worse than the statistical error.

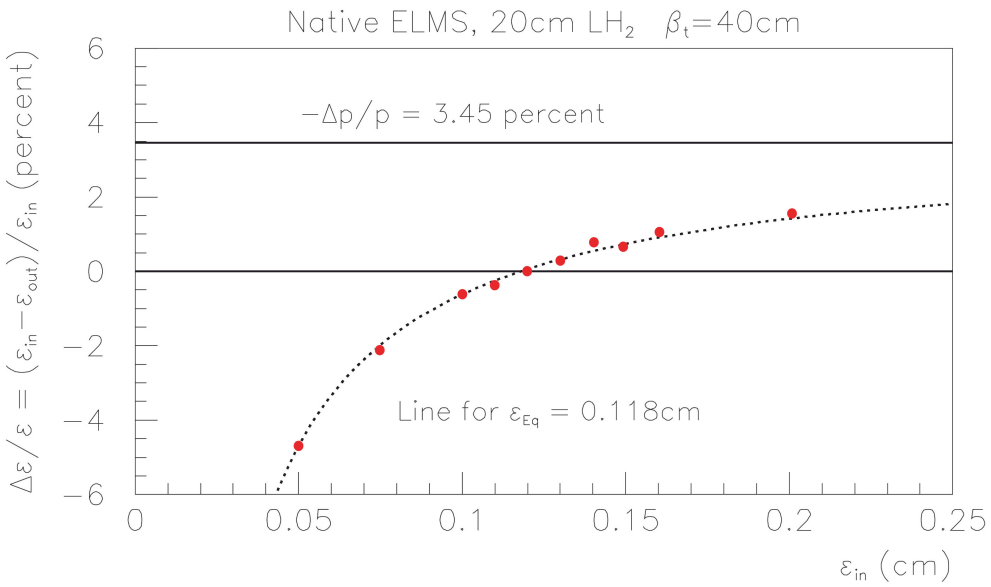

Figure 4.13: Equilibrium emittance for native ELMS, the red points showing the data are considerably larger than the error bars. The line represents a best fit to the data by varying the value of equillibrium emittance.

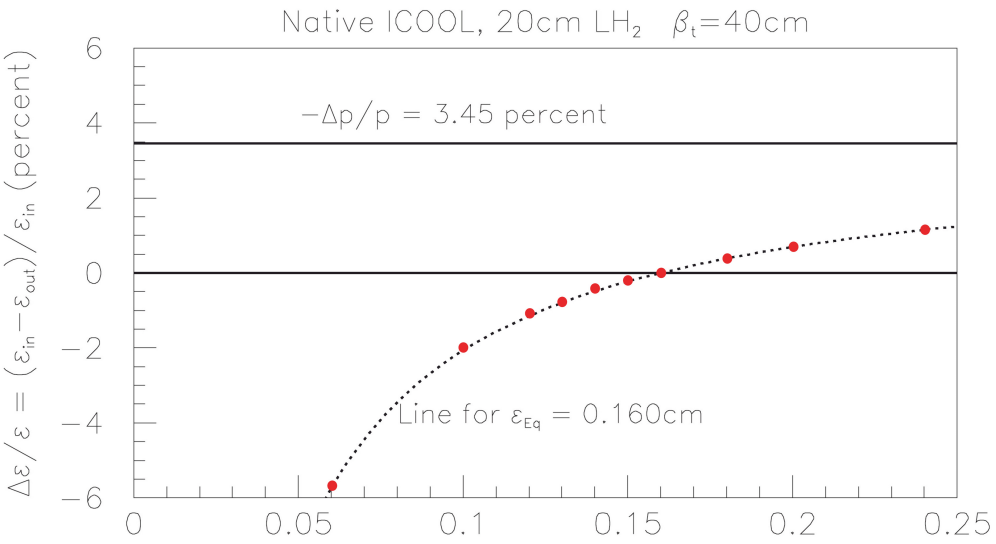

Figure 4.14: Equilibrium emittance for native ICOOL, the red points showing the data are considerably larger than the error bars. The line represents a best fit to the data by varying the value of equillibrium emittance.

Hence $\epsilon_{\infty_{ICOOL}} = 0.160$ cm , $\epsilon_{\infty_{ELMS}} = 0.118$ cm and the ratio is 1.36. The ratio of the asymptotic values from the RFOFO run was 1.33. This confirms the decreased equilibrium emittance predicted by ELMS in ICOOL for the RFOFO and the value is significant to muon cooling studies. However emittance is defined as a Gaussian property, whilst the ELMS cross section is concerned with non-Gaussian effects. Lower emittance says nothing about, for instance, how many particles have been lost from the RF bucket.

The formula can also be used for MICE, the ratio of the emittance change between ELMS and standard ICOOL is independant of dp/p, and using a typical $\epsilon_{in} = 0.6$ cm predicts the ratio of emittance change across the channel as 10% in favour of ELMS (ignoring windows). This backs up what was observed in figure 4.8 and is observable since MICE aims to measure emittance change to 1% [48]. The effect will be more pronounced as the initial beam emittance is lower so MICE should tune the beam to have an emittance near to the equillibrium value.

4.7 Summary

The ELMS folded probability distribution generated from a first principle cross section for the energy loss and scattering of muons in liquid hydrogen was successfully incorporated

into the ICOOL simulation program. This framework allows for running with an option of dual sampling to study the effects of removing the correlations between energy loss and multiple scattering that are present at cross section level. It can also be extended to other materials in the future by changing the conditions under which ICOOL uses the probability distribution from ELMS as opposed to its own routines. Incorporating the ELMS engine for liquid hydrogen does not affect the rest of the program, or the results of energy loss and scattering in other materials. Hence it is possible to compare like for like results for muon cooling in a variety of cooling scenarios including the linear MICE channel, and the circular RFOFO set up.

A simulation of the MICE set-up shows a ten percent decrease in final transverse emittance predicted by ELMS in ICOOL compared to native ICOOL. This should be an observable effect since MICE has an aim of measuring a one percent change in emittance. When the channel is extended to 100m (by using a repeated cell structure) a simillar difference emerges once the set-up is adjusted to run off peak and take account of the transit time factor: standard ICOOL shows a transverse cooling performance of 55%, ELMS in ICOOL predicts 59%.

The RFOFO confirms that correlations do not affect cooling performance, neither in the transverse nor longitudinal plane, nor in other measures like merit factor and the density of muons that can be cooled into a given acceptance. However the RFOFO can cool down to the equilibrium emittance value and this shows a 30% decrease in equilibrium emittance predicted by ELMS in ICOOL compared to standard ICOOL. This increases the merit factor by a factor of 2, and increases the number of muons into a smaller acceptance volume by 40%. This improvement will be reduced in practise since the RFOFO tested here did not contain absorber or RF windows.

The decrease in equilibrium emittance predicted by ELMS in ICOOL was checked by using a simple arrangement of a slab of liquid hydrogen and a beam defined to have a β_T similar to that encountered in MICE or the RFOFO and an emittance near to equilibrium. When this beam was passed through the hydrogen the percentage change in emittance it saw was modelled to fit for the equilibrium emittance. The results showed that the ratio in the equilibrium predicted by ELMS and ICOOL was the same size as for the RFOFO, just over 30%.

The reason for the improvement in cooling and equillibrium emittance is that the scattering predicted by ELMS has a smaller tail than that predicted by native ICOOL. The central areas agree, but above a certain Pt^2 the ICOOL tail is two or three times larger than that of ELMS. The explanation for this is the way that electrons are included in the Moliere scattering formula - the factors $Z(Z+1)$ that replaces the standard Z^2 in the Rutherford cross section does not hold for angles greater than 4.8 mrad, since this is the kinematic limit to electron contribution. ELMS correctly takes care of the electron in the constituent and resonant scattering areas of the cross section.

As with any new prediction, what is required to confirm the accuracy of the ELMS cross section is an experimental verification. Fortuitously, at the same time as this work was carried out, the MUSCAT experiment was taking data and analysing results. This offered the chance to test the scattering predictions and also look for evidence of correlations in multiple scattering and energy loss.

Chapter 5

Empirical muon scattering data

Simulations of muon cooling show that the rigorous ELMS cross section predicts an observable improvement in the cooling offered by long channels of liquid hydrogen absorbers and re-acceleration. The reason for this difference is that traditional simulations model multiple scattering in low Z materials by unnecessary simplification. Motivated by the need to understand the discrepancy in observed scattering for low Z materials and traditional predictions, the MUSCAT experiment [75] has measured the scattering of 172 MeV/c muons in a variety of materials. The unfolded data for liquid hydrogen is presented here and compared to the predictions of Moliere theory, GEANT, and ELMS. For liquid hydrogen there is some discrepancy between the results. The ELMS prediction matches the observed data within errors. However the MUSCAT apparatus is not sensitive enough to confirm the existence of the predicted correlations between energy loss and multiple scattering.

5.1 Experimental set-up

MUSCAT measures the scattering of a beam of muons in various targets using a muon source with a collimator system and three scintillating fibre trackers. There is also a sodium iodide calorimeter (TINA) to help with particle identification, and scintillators that act as triggers. The set-up used for MUSCAT is shown in figure 5.1. The muons are created from the M20 muon beam line at TRIUMF with an average momentum of 172 MeV/c $\pm$2.0 MeV/c.

The collimator consists of two lead blocks with slits in them that the muons must pass through to be accepted. The slit system gives a beam that is narrow in one direction but broader in the other to preserve a high rate of particles. To ensure that the muons can not scatter off the jaw of the first collimator and miss the second entirely there are eight auxiliary collimators between the two slits. Two active collimator bars sit just above and below the front slit, to record particles which otherwise would have hit the lead and passed into the slit with a large $\mathrm{d}E/\mathrm{d}x$ and scattering.

The hydrogen target was filled with liquid or gaseous hydrogen, allowing the contribution

from the containment windows to be evaluated. During the experiment the temperature was in the range of 15.5 and 16 K [76], giving an estimate of the density as 0.755 g cm^{-3}. The target can be oriented to present a long (15.9 cm) or short (10.9 cm) liquid hydrogen length.

The scintillating fibres select hits that are consistent with having come from the target. However due to the arrangement of the fibres - 512 fibres in x and y made from two bundles of 256 - there is an efficiency problem at the center because of the location of the edge fibres. There is also a problem of cross talk due to refraction in the 1.5mm of glass before the photomultiplier tubes leading from the fibres. To some extent these problems are reduced by tuning the simulation to the results with a thick iron target, for which the Gaussian center dominates the scattering distribution.

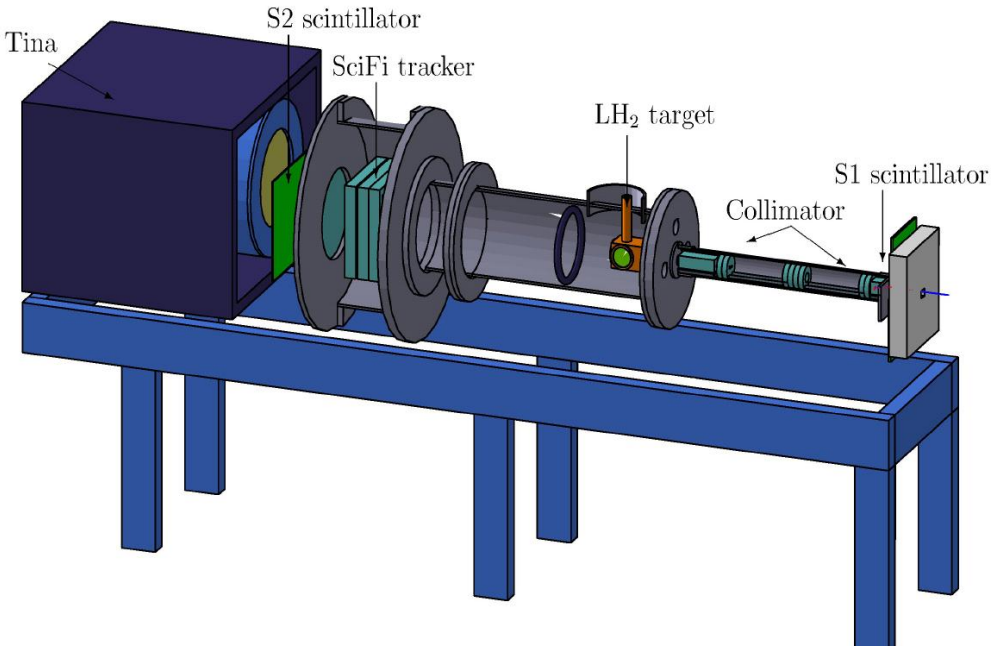

Figure 5.1: The MUSCAT experimental set-up from the GEANT simulation model. The beam coming in from the right of the picture passes through a collimator before illuminating the target. The SciFi trackers then measure the position after the drift section. The TINA calorimeter measures energy deposition [75].

5.2 Analysis and deconvolution technique

Recorded events are exposed to a number of filters to determine if they are the signals from muons that have been scattered in the target. These include requiring that the event is taken during a period of proper operation of the data acquisition and time of flight system,

and that the hits on the various scintillators point to a particle that has passed through the target [75].

Having selected the muon events, it is possible to study the position of the muons at the first detector and compare this to ELMS or GEANT, however this does not remove all systematic effects from the results. Instead, a deconvolution is required to give any real meaning to the experiment. This removes the effects of the beam width, efficiency of the detector, background, pion contamination, etc, leaving just the scattering caused in the target itself. It is carried out using the formula,

$$D = B + D_\pi + R \cdot \epsilon \cdot \Theta.$$

Where D is the observed position data, B the background of muons not passing through the target, and D_π the pion contamination. R is a matrix representing the response of the detector as a function of the particle deflection angle (θ_y), ϵ is a matrix that represents the efficiency of the detector as a function of the deflection angle, and Θ is the projected scattering distribution in the target.

The response and efficiency matrices are found from simulation. The efficiency is found by making two runs of GEANT 4. The first is a simulation consisting of mono-energetic beam plus target only. This gives the underlying scattering distribution. The second is the full simulation including tracking and acceptance cuts. The ratio of the two gives the efficiency. The response is found by recording each accepted event (in the simulation) as a function of angle and y position at the first measurement plane. This therefore gives a probability of measurement for each true deflection angle.

The equation is then solved for Θ imposing symmetry around $\theta = 0$, and reducing the number of bins from 57 to 22 to reduce instabilities. The last bin is not shown in plots since it runs from 115 mrad to π and contains very few actual events. It is instead highly dependent on the simulated predictions. Note that the formalism does not include the effect of scattering or energy loss in the x direction. The probability that a particle misses the detector in the x direction as a function of its y angle can only be taken from simulation, which is a large systematic error.

5.3 Results

Shown here are the results of comparing an ELMS simulation of the bare MUSCAT set-up (with the correct momentum, density, etc, but no containers) with the deconvoluted data, and also to Moliere theory and GEANT 4.7. The results are expressed in terms of the probability of scattering through a given angle in radians. Figure 5.2 shows the results for the short liquid hydrogen target and figure 5.3 shows the results for the long one.

Observation of these shows that the two Moliere models considered are clearly separate from one another in liquid hydrogen, and both are inadequate to describe the observed scattering performance, with the actual data being closer to Moliere $Z(Z+1)$ at small angles and closer to Moliere Z^2 at large angles, which is as expected. The ELMS result describes the data well at all points except the outermost bin, which contains the largest systematic errors. Referring to the results for 10.9cm of liquid hydrogen and figure 4.4, the scattering of 200 MeV/c muons in a 10cm slab of liquid hydrogen that shows an increase in ICOOL/ELMS at around 10 $(\mathrm{MeV/c})^2$, in the MUSCAT results the transistion from $Z(Z+1)$ to Z^2 occurs more or less where expected, $\theta \approx \frac{\sqrt{10}\mathrm{MeV/c}}{172\mathrm{MeV/c}} \approx 20\mathrm{mrad}$.

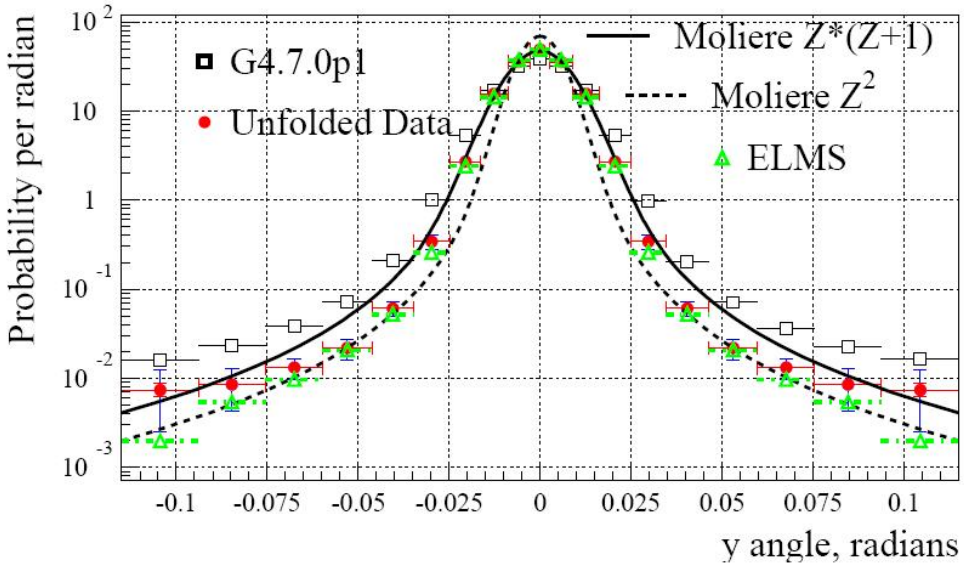

Figure 5.2: The deconvoluted results from MUSCAT showing the short (10.9 cm) liquid hydrogen target [75]. The ELMS predictions match the data well. Moliere $Z(Z+1)$ describes the data well at low angles, while Moliere Z^2 is better at high angles as is expected. Neither model is adequate for intermediate angles. GEANT agrees with Moliere $Z(Z+1)$ at low angles, but overestimates the scattering by a factor of 4 at large angles.

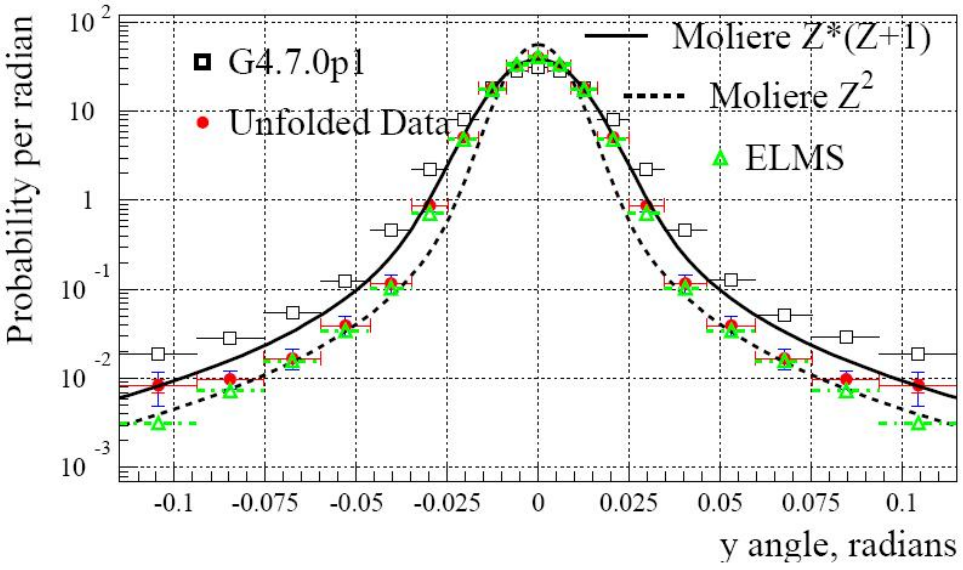

Figure 5.3: The deconvoluted results from MUSCAT showing the long (15.9 cm) liquid hydrogen target [75]. Again ELMS describes the deconvoluted results well. The discrepancy between the other predictions is simillar to those in the short target.

GEANT has a tail that is a factor 4 too large in liquid hydrogen. Indeed, GEANT (4.7.0p01) does not implement Moliere theory well; it tends to overestimate the scattering at large angles compared to either model. Comparing result for liquid hydrogen to other materials tested with MUSCAT [75] reiterates that there is a problem with Moliere theory for low Z only. Note that the lithium discrepancy mentioned in chapter 2 from old data for electron scattering are not confirmed by MUSCAT, if anything the scattering from GEANT needs reducing, not increasing, which is beneficial for muon cooling work. Table 5.1 shows numerically the difference between the data and the GEANT prediction. A chi-squared test on these values,

$$\chi^2 = \sum_{\mathrm{i=bin}} \frac{(\mathrm{data_i} - \mathrm{theory_i})^2}{\mathrm{error_i^2}},$$

where the error is the combined error from experiement and theory, gives $\chi^2_{\mathrm{ELMS}} = 25.0$ and $\chi^2_{\mathrm{Geant}} = 470$. With 10 degrees of freedom the critical value at the 0.005 probability level is 25.2. This confirms that, within errors, ELMS correctly predicts the scattering of muons in liquid hydrogen.

Upper edge of bin (radians)	Data	ELMS	GEANT 4
0.00269	49.5 ± 2.7	49.6 ± 0.07	38.7 ± 0.04
0.00895	35.8 ± 1.5	37.7 ± 0.05	32.2 ± 0.03
0.0162	15.7 ± 0.41	17.4 ± 0.02	14.5 ± 0.03
0.0248	2.70 ± 0.39	2.43 ± 0.01	5.33 ± 0.01
0.0347	0.34 ± 0.061	0.26 ± 0.004	1.00 ± 0.005
0.0463	0.061 ± 0.012	0.052 ± 0.001	0.205 ± 0.002
0.0597	0.022 ± 0.006	0.021 ± 0.0009	0.071 ± 0.001
0.0754	0.013 ± 0.003	0.010 ± 0.0008	0.036 ± 0.0008
0.0938	0.008 ± 0.004	0.005 ± 0.0004	0.023 ± 0.0006
0.1151	0.007 ± 0.005	0.002 ± 0.0002	0.017 ± 0.0004
3.141	0.0025 ± 0.0025	3.6 E-05± 0.2 E-05	0.0025 ± 1.5 E-05

Table 5.1: MUSCAT data and simulated predictions for scattering in 10.9 cm of liquid hydrogen in terms of the probability per radian of scattering through a given angle [75].

5.3.1 Systematic errors

The error bars on the plots presented in the last section are large. This is due to an over-exageration of the error effects since some of the systematics considered overlap. The collimator system caused a problem in simulation [75]. Accounting for the difference in collimator distribution gives the biggest errors. It is checked in three ways to err on the side of caution, but combining these checks - a background level check, an additional collimator difference, and the collimator deconvolution with no target - adds a factor of $\sqrt{3}$ to the total error [77].

In general the width of beam is not well simulated - the apparent width and observed tails are wider in data than simulation (assuming perfect geometry). Also, the distributions are normalised to the centre, so the effects of the efficiency problem caused by the edge fibres being present at the centre of the sci-fi trackers show up in the tails of the distribution.

The matrix used to relate true scattering angle to measured position is taken from simulation. It depends on the physics in that simulation, for instance the scattering in the x direction. This dependence is reduced by reweighting all the simulated events as a function of the space angle scatter, which moves GEANT towards Moliere Z^2 above 40 mrad. Hence a further systematic error is computed by comparing the reweighted simulation with the ELMS prediction. This is one of the largest systematic error at the very edge of the deconvoluted distribution [75].

5.4 Correlations in scattering and energy loss

ELMS predicts that muons passing through 10.9cm of liquid hydrogen should emerge correlated in energy and transverse momentum because collisions with constituent electrons account for half of the energy loss and half of the scattering. Hence the MUSCAT calorimeter (TINA) might be able to observe a dependency in energy on the position of the muons, which would confirm the ELMS prediction (although this correlation does not seem to affect muon cooling performance). The confirmation is complicated by the effect of the containment vessel, the resolution of the detector, the nature of the input beam, and the finite size of the calorimeter.

The TINA calorimeter is a sodium iodide crystal (460 mm diameter and 510 mm long). It is mounted off centre to give a complete angular coverage in the y direction. A 14 mm steel rim takes up some of the space towards the edge. The calorimeter is an absorption calorimeter and has a linear response. A comparison of the full and empty liquid hydrogen runs does show an appreciable decrease in the TINA readout. Overall the resolution is a couple of percent, but the 10^6 events should enable effects at the 0.001 level to be observed. Figure 5.4 shows a contour plot of the average reading in volts from the calorimeter against the x and y position for all of incident muons.

The beam in the x direction is too diffuse to give meaningful results. To get a sensible plot of the calorimeter voltage against the y position a correction is applied to make the thick steel target have a flat distribution. This same correction is then applied to the liquid hydrogen data and Monte Carlo to give a distribution as shown in figure 5.5. This is not flat, as might be expected if the correlations exist, but it is unknown if the angle dependencies are due to the correlation in energy loss and scattering or something else, for instance the varying gains on the seven photomultiplier tubes used to amplify the signal from the calorimeter. An ELMS prediction adds some clarity, as shown in figure 5.6.

Unfortunately the ELMS predictions are pessimistic. The difference in energy of muons in the region of the calorimeter between the two runs (one with correlations and one without) is around 0.02%, which will not be observable with the resolution and statistics of the MUSCAT run. Extending the scattering angle outwards and using the same statistics as MUSCAT, see figure 5.7, shows that there is a 0.5% difference in muon energy at a position above 10cm.

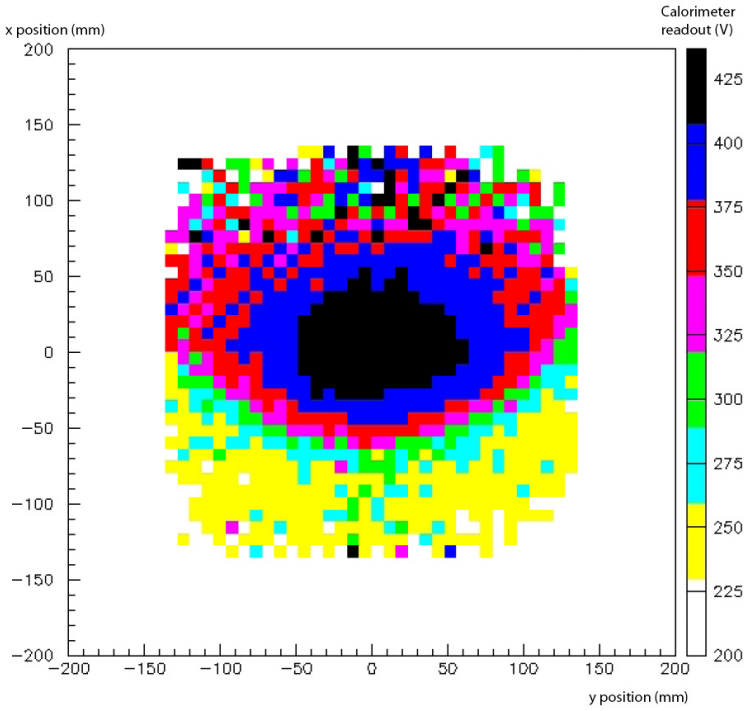

Figure 5.4: A contour plot of the MUCAT calorimeter readout for the liquid hydrogen target, voltage against the x and y position. The edges of the calorimeter show signs of muon leakage.

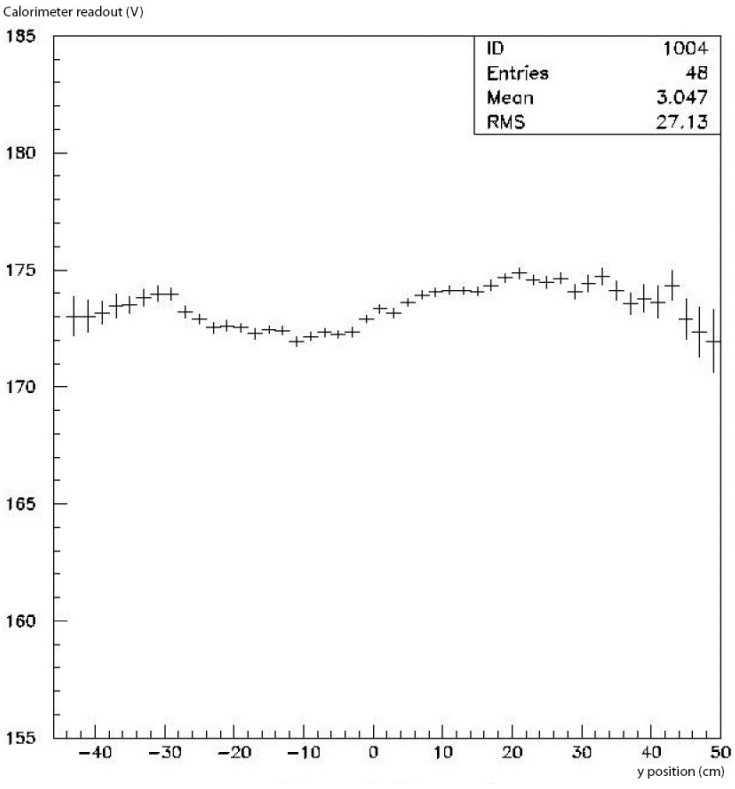

Figure 5.5: The MUSCAT calorimeter signal corrected by Monte Carlo.

With hindsight a larger calorimeter with better resolution would have been beneficial, but the predicted correlation from ELMS was not known at the time the experiment was designed.

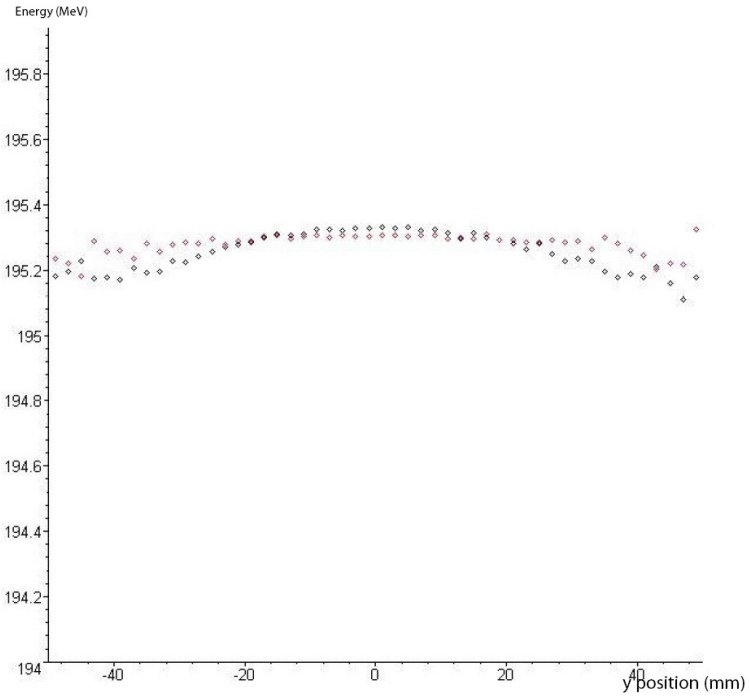

Figure 5.6: ELMS prediction of position versus energy in the MUSCAT calorimeter. The red dots show the effect of neglecting correlations. The position refers to the TINA position, not the actual space position since this is offset. The y axis shows muon energy for 10^6 events.

5.5 Summary

The ELMS predictions of the scattering of muons in liquid hydrogen are confirmed by the deconvoluted results taken by the MUSCAT experiment. As expected, the data looks like Moliere $Z(Z+1)$ at low angles and Moliere Z^2 at large angles. However the intermediate region is badly described by both Moliere models, and GEANT is a factor 4 too high at large angles. ELMS simulates scattering properly, not relying on Moliere at all, and it gets results that describe the data to within errors for all but the largest angles. At large angles there is a large systematic error because of an efficiency problem at the centre of the detector, the correction on the GEANT physics used in deconvolution, and not being able to simulate the beam collimation system well enough.

An examination of the MUSCAT calorimeter signal was not able to observe the ELMS predicted correlation between scattering and energy loss. This was becasue the experiment

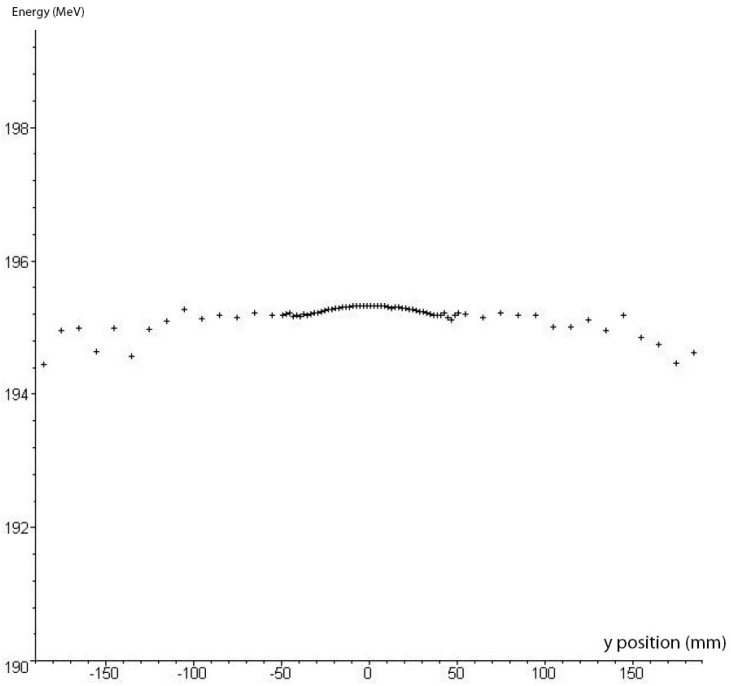

Figure 5.7: ELMS prediction of position versus energy beyond the MUSCAT calorimeter for 10^6 muons. This leads to an observable effect outside 10cm. Note that edge muons may not go all the way through the calorimeter in any case.

was not designed to look for correlations - the resolution and size of the calorimeter were not large enough to see any effect. However the correlation has been shown not to affect the cooling performances simulated in chapter 4, so its confirmation remains as more of a tidying up exercise for some future experiment.

Chapter 6

Conclusion

Although both theoretically and experimentally challenging, the multiple scattering and energy loss of muons in liquid hydrogen has been resolved by the work presented in this thesis. This work was motivated by the need to understand the behavior of muons in materials of low atomic number because the technique of ionisation cooling is used to get a focused muon beam, and relies on passing muons through such a material and re-accelerating in the longitudinal direction many times. A focused muon beam could be put into a storage ring where the muons would decay into muon and electron type neutrinos that could be studied, it would also be the first step towards building a muon collider that could reach higher energy than traditional colliders. These machines could probe the areas of physics that have given hints that the standard model of particle physics is incomplete.

An experimental validation of the ionisation cooling technique is under construction at the Rutherford Appleton laboratory. The Muon Ionisation Cooling Experiment (MICE) is a short section of a full cooling channel. MICE is more of an engineering challenge than physics experiment since ionisation cooling is a sound principle. But one of the motivations behind MICE was that the scattering of muons in low Z materials is short on data, and what does exist suggests that the traditional Moliere model is not suitable for $Z < 4$. In the days of modern computing power the simplifications used in traditional approaches are not necessary, and given the iterative nature of muon cooling it is important to make simulation as accurate as possible.

Beginning from well understood physics ideas, a first principles derivation of the electromagnetic interactions of charged particles in matter (ELMS) gave a double differential cross

section for the energy loss and scattering of muons in liquid hydrogen. The cross section showed a correlation between scattering and energy loss due to electron constituent scatters that has not been considered in previous treatments, and was important for muons in liquid hydrogen since these electron scatters provide about half of the energy loss and half of the scattering.

Using a folding technique the ELMS cross section was turned into a three dimensional probability distribution for the scattering and energy loss for muons in sub-mm lengths of liquid hydrogen. This probability distribution was incorporated into an existing muon cooling simulation program, ICOOL, bypassing the existing energy loss and scattering routines (which are dealt with in separate steps) to give the hybrid ELMS in ICOOL. The mean energy loss and range of muons in liquid hydrogen predicted by ELMS (in ICOOL) compared with that predicted by the Bethe Bloche formula, and the full energy loss distributions were similar to those produced from running alternate simulation software such as GEANT and native ICOOL. Energy loss was shown to be reasonably well modelled by existing simplifications.

However results from MUSCAT, which was built to measure the scattering of muons in various materials, have confirmed the ELMS scattering predictions for liquid hydrogen, and shown that predictions from GEANT and simple Moliere theory are not adequate to describe the scattering of muons in liquid hydrogen. Traditional calculations over-estimate the scattering in liquid hydrogen because they do not take account of the kinematic limits on electron scattering and so allow electrons to contribute to scattering through larger angles than they should. This anomaly was first noted by Tollestrup. Correcting for this problem ad hoc in existing simulations is non trivial; on the other hand, it was not an issue when the energy loss and scattering are handled properly by ELMS.

With a decrease in the tail of the multiple scattering distribution, ELMS in ICOOL predicted an improvement in muon cooling on multiple revolutions of a circular RFOFO channel. Here the equilibrium cooling predicted by ELMS in ICOOL was 33% lower than that predicted by native ICOOL. This was confirmed by an independent test that studied the emittance change in a slab of liquid hydrogen using a beam prepared to have a transverse beta function simillar to that found in MICE and the RFOFO. ELMS in ICOOL also predicted a ten percent decrease in emittance over native ICOOL in the MICE channel and this should

be observable.

The ELMS predicted correlation in energy loss and multiple scattering could not be seen in MUSCAT, which was disappointing but unsurprising as the experiment was never designed to look for such correlations. The search was made difficult by the relatively small size of the calorimeter crystal, but the energy resolution, presence of the hydrogen containment vessel, and the broad spread in momentum of the initial beam also hindered the task. However simulations using ELMS in ICOOL running uncorrelated by double sampling from the probability distribution showed that the presence of correlations does not effect muon cooling performance.

The most important question raised by this work is whether the sizable improvements predicted by ELMS will actually survive into a real muon cooling channel. The RFOFO examined in comparative studies was an idealised situation that did not contain hydrogen windows or Beryllium windows in the RF cavity (though note that the MICE like channels did and still showed a reasonable increase in emittance reduction over 100m). Table 6.1 is taken from a study by Palmer [49] and compares the D-factor of various combinations of absorber and windows for a similar RFOFO to that studied here. The comparison looks at the effect of adding in aluminium windows around the absorbers, beryllium windows in the RF cavities, and empty cells for extraction/injection of the muon beam. The performance measure is the D-factor, which represents the density of muons inside a realistic neutrino factory acceptance.

US Study II windows (360μ m of aluminium) degrade performance by about 30%, but for less thickness the amount reduces elastically. There is some scope for a reduced thickness in practise through careful shaping of the absorber windows to reduce stress. An alternative would be to use a material that requires no window, for instance lithium or lithium hydride. This has been proposed in the new Study IIb document as a direct consequence of the cost of the cooling channel. Although the reduction in D-factor with LiH absorbers and no RF windows or empty cells is 45% when compared to the ideal liquid hydrogen ring [49]. Alternative low Z cooling materials could and should be modelled with ELMS and compared.

The Be windows of the RF cavities have a significant effect on performance, in Study II the end windows were 200 μm thick out to a 12 cm radius, then 400 μm thick to 18 cm. The interior windows were 700 μm out to a radius of 14cm then 1400 μm to 21cm. Together these

Absorber Window	RF Window	Empty Cells	D-factor
none	none	0	8.93
250 μm Al	none	0	7.50
360 μm Al	none	0	6.60
500 μm Al	none	0	6.08
none	FS2	0	5.88
none	FS2/20	0	7.80
none	none	2	6.73
360 μm Al	FS2/20	2	4.25

Table 6.1: The effect of simulating various iterations of a realistic RFOFO channel compared to the idealised channel [49]. Three thicknesses of absorber window are used, the neutrino factory feasibility study II (FS2) considered 360 μm of aluminium. The RF windows are tested at study II thickness, or a twentieth of this under lower operating temperature and reduced RF gradient. The empty cells are needed on a real cooling ring for injection/extraction.

windows gave a 35% reduction. However an alternate scenario operating at liquid nitrogen temperatures and hence a lower accelerating gradient (12 MV/m, against 16 MV/m) allows windows of a twentieth of the thickness giving a performance loss of only 13%. It would also be possible to use an open cavity with no windows, but this would require four times as much power to create the same field on axis. Empty cells are necessary to get the beam into and out of the ring. Removing absorbers from these two cells gave a 25% reduction.

So with care, the additional parts of a realistic channel do not have an overwhelming effect on the cooling performance. For comparison, the ELMS in ICOOL D-factor for the idealised absorber tested in Chapter 4 is 13.4, compared to the native ICOOL value of 10.3 which represents an increase of 30%. Hence the ELMS predicted cooling improvement roughly negates the detrimental effect of the absorber windows, though the effects are not simply multiplicative. This is positive news for the muon cooling collaborations.

Following on from this it would be useful to extend ELMS to other materials – lithium, lithium hydride, etc for absorbers. And also perhaps window material as scattering from these does have role. However, theory and the experimental work from MUSCAT expects that a proper treatment of scattering will be simillar to the traditional predictions for higher Z materials. The problem in using the ELMS method for other materials is that the refractive index of a solid is undefined and so the effect of material density is hard to account for. However using the gaseous atomic photo absorption spectrum had little effect on scattering,

it was only the energy loss that was affected, which means that an ELMS comparison with MUSCAT for lithium is possible.

ELMS in ICOOL is not significantly slower than native ICOOL (though could be further optimized) when running. But statistics are an issue, though this is an inherent ICOOL concern since ICOOL is set up to run 100,000 events as it is a complex simulation with many variables to be tracked and file sizes can get out of control. Using native ELMS to run over a million events in simplistic set-ups is a way around this (for instance with the MUSCAT comparison), but an overhaul of the ICOOL architecture to increase statistics might be beneficial.

From a starting position where there was still confusion about the proper implementation of scattering in low Z materials, this work has, for hydrogen at least, solved all of the associated theoretical problems. The results from MUSCAT confirming the earlier predictions were important given that they were made blind to the actual scattering distributions. More importantly ELMS predicts that the cooling performance of hydrogen is increased by a significant amount; the achievable neutrino flux from a neutrino factory should be greater than current estimates. It is hoped that these findings will act as a spur for the whole muon cooling collaboration.

Bibliography

[1] K. Hagiwara et al. *Phys. Rev. D*, **66**. `http://pdg.lbl.gov`

[2] W. Pauli. *(English Translation) Physics Today*, **31**, 27.

[3] S.F. Adams. *Phys. Educ.*, **27** (1992) 102–108.

[4] J. Chadwick. *Verh.d.Deutschen.Phys.Ges.*, **16** (1914) 383.

[5] C.D. Ellis & W.A.Wooster. *Proc.Roy.Soc. A*, , 117 (1927) 109.

[6] L. Meitner & W. Orthman. *Z.Physik.*, **60** (1933) 143.

[7] D.H. Perkins. "Introduction to High Energy Physics". Cambridge University Press, 4th edition (2000). ISBN 0521621968.

[8] F.B. Harrison H.W. Kruse F. Reines, C.L. Cowan & A.D. McGuire. *Science*, **124**, 3212 (1956) 103–104.

[9] S. Basu J.N. Bahcall & M.H. Pinsonneault. *Phys.Lett.*, **B**, 433 (1998) 1–8.

[10] C. Nishi S. de Leo & P. Rotelli. *Int. J. Mod. Phys. A*, **19** (2004) 677–694.

[11] D.E. Groom et al. [PDG collaboration]. *Eur. Phys. J. C*, **15** (2000) 1.

[12] K. Winter. "Neutrino Physics". Cambridge Monographs on Particle Physics (2000).

[13] J.Hosek S.M. Bilenky & S.T. Petcov. *Phys. Lett. B*, **94** (1980) 495.

[14] W.M. Alberico. *Phys.Part.Nucl.*, **35** (2004) 297–323.

[15] G. Albright et. al. *Fermilab Notes*, **692 (2004)**.

[16] "Super Kamiokande and K2K at Boston U." `http:hep.bu.edu/ superk/atmnu.html`

[17] S. Gregory M. Zeilik & E. Smith. "Introductory Astronomy and Astrophysics". Saunders, 3rd edition (1992). ISBN 0030316979.

[18] A. McDonald. "Results from SNO". Nobel Symposium (2004).

[19] K.Eguchi et al. *Physical Review Letters*, **90**, 2 (2003).

[20] M. Apollonio et al. *Phys. Lett.*, **B420** (1998) 397–404. `hep-ex/9711002`

[21] D.A. Petyt. *DPhil Thesis University of Oxford*, **1998** 56–75.

[22] The MICE collaboration. *Proposal to the Rutherford Appleton laboratory*, **2003**.

[23] J. C. Street & E. C. Stevenson. *Phys. Rev.*, **52** (1937) 1003–1004.

[24] M. Zisman S. Ozaki, R. Palmer & J. Gallardo. *BNL-52623*, **2001**.

[25] S. Geer. *FERMILAB-Pub-00/108-E*, **2000**.

[26] R. Raja V. Barger, S. Geer & K. Whisnant. *hep-ph/9911524*.

[27] J.Hosek S.M. Bilenky & S.T. Petcov. *Phys Lett*, **B94**, 2 (1980) 495.

[28] B. Aubert et al. *Phys. Rev. Lett.*, **33 (1974)**.

[29] F. Mandl & G.Shaw. "Quantum Field Theory" (1996).

[30] M. Carena & H.E. Haber. *Fermilab-Pub-02*. arXiv:hep-ph/0208209

[31] G. P. Salam (2004). http://www.lpthe.jussieu.fr/salam/talks/

[32] LEP EWWG. www.cern.ch/LEPEWWG/

[33] R.P. Walker. *CERN Accelerator School*, pages 437–459. http://preprints.cern.ch/yellowrep/1994/94-01/p437.pdf

[34] M. Peel. http://www.mikepeel.net/mphys.php

[35] J. Rosenzweig. "Fundamentals of Beam Physics". Oxford University Press (Oxford) (2003). ISBN 0198525540.

[36] A.N. Skrinsky & V.V. Parkhomchuk. *Sov. J. Part. Nucl.*, **12**, 223 (1981).

[37] Ken Long. www.hep.ph.ic.ac.uk/ longkr/Presentations/MICE/2004-11-17-SC.ppt

[38] R.B. Palmer et al. arxiv:acc-phys/950302

[39] E. Wilson. "An Introduction to Particle Accelerators". Oxford University Press (Oxford) (2001). ISBN 0198508298.

[40] R. P. Johnson. http:/hadron.kek.jp/Nufact/Johnson-wg3.ppt

[41] J. Cobb. "Discussion of Farley's paper". MICE Meeting, Osaka (2004).

[42] D. Kaplan. "Introduction to Muon Cooling". Snowmass Summer Study on the Future of Particle Physics (2001). http://arxiv.prg/abs/physics/0109061

[43] K. Wille. "The Physics of Particle Accelerators: an Introduction". Oxford University Press (Oxford) (2001). ISBN 0198505493.

[44] K. Floetman. *Phys. Rev. Special Topics, Accel + Beams*, **6**, 034202 (2003).

[45] R.C. Fernow & J.C. Gallardo. *Physical Review E*, **52**, 1 (1995) 1039–1042.

[46] J. Cobb. "Private Communication".

[47] J. Cobb. Private Communication.

[48] `www.isis.rl.ac.uk`

[49] R.B.Palmer et al. *Phys.Rev.*, **ST Accel.Beams**, 8 (2005).

[50] J. Cobb. Private Communication.

[51] A. I. Andrievsky et al. *J. Phys. (USSR)*, **6** (1942) 279.

[52] W.W.M. Allison. "Graduate Course Lectures, Oxford University".

[53] J. D. Jackson. "Classical Electrodynamics" (1998).

[54] W.W.M. Allison. Private Communication.

[55] W.W.M. Allison & J.H. Cobb. *Ann. Rev. Nucl. Part. Sci.*, **30** (1980) 253–298.

[56] R.G. Newton. "Scattering Theory of Waves and Particles". Dover, 2nd edition.

[57] W.S.C. Williams. "Nuclear and Particle Physics". Oxford University Press (Oxford). ISBN 0198520468.

[58] M. Apostol. "On a Thomas-Fermi model of hollow atom" (1996). `http://www.citebase.org/cgi-bin/citations?id=oai:arXiv.org:chem-ph/9607002`

[59] J. Berkowitz. "Atomic and Molecular Photoabsorption". Academic Press (2002).

[60] W.W.M. Allison. Private Communication.

[61] E. Fermi. *Z.Physik.*, **88** (1934) 161.

[62] C. Baxter. *J. Phys. B: At. Mol. Opt. Phys.*, **25 (1992)**.

[63] Cross section moments produced with the assistance of S. Brooks.

[64] H.A. Bethe. *Phys. Rev.*, **89**, 6 (1953) 1256–1266.

[65] G. Moliere. *Z. Naturforsch*, **3a**, 78 (1948).

[66] H. W. Lewis. *Phys. Rev.*, **78**, 526 (1950).

[67] H. A. Bethe. *Phys. Rev.*, **89**, 6 (1953).

[68] A. Tollestrup. MUCOOL notes 176.

[69] "GEANT". `http://geant4.web.cern.ch/geant4/`

[70] R.C. Fernow et al. `http://pubweb.bnl.gov/users/fernow/www/icool/`

[71] P. Spentzouris J. Monroe, P. Lebrun. "DPGEANT and ICOOL code comparison". Mucool Notes 72.

[72] U. Bravar. **Bene Talk (2004)**.

[73] "MICE Technical Reference Document". `http://ndapelham/accelerator/MICE/TR/`

[74] J. Cobb. Private Communication.

[75] D. Attwood et al. "The Scattering of Muons in Low Z Materials" (2005). `www.arxiv.org/ps cache/hep-ex/pdf/0512/0512005.pdf`

[76] W. Murray. "Density of Muscat Hydrogen Target" (2005). `wmurray.home.cern.ch/wmurray/mumu/muscatII/density.pdf`

[77] W. Murray. Private Communication.